Ionic liquids and ionic liquid-like systems – from molecular structure to macroscopical properties

Dissertation

zur Erlangung des Doktorgrades der Naturwissenschaften (Dr. rer. nat.)

der Naturwissenschaftlichen Fakultät II

Chemie, Physik und Mathematik

der Martin-Luther-Universität Halle-Wittenberg

vorgelegt von

Frau Ulrike Cerajewski

geboren am 10. 05. 1990 in Potsdam

Erstgutachter: Prof. Dr. Dariush Hinderberger

Zweitgutachter: Prof. Dr. Matvey Fedin

Datum der Verteidigung: 02.12.2020

Abstract

Ionic liquids (ILs) and ionic liquid-like systems seem to be a promising alternative to commonly used solvents, electrolytes or reaction media. Especially due to their lower toxicity and negligible volatility, ionic liquids can be a driving factor in the transformation to environmentally friendly industrial processes in pharmaceutical and chemical economy. In order to gain a better understanding in ionic liquid systems and how they could be modified to achieve the best results in their desired application, three different systems were investigated. Part 1 describes a system of [EMIm][Cl] and urea, which forms a dystectic mixture, *i.e.* features a local melting point maximum and two minima. By means of different measurement techniques and spectroscopy, the origin of the mixture's physicochemical properties is evaluated on a nanoscopical scale. Results from this experiment have already been published (Cerajewski et al., PCCP 12/2018[1] – reproduced by permission of the PCCP Owner Societies). In Part 2, a deep-eutectic solvent mixture is investigated, consisting of choline chloride and imidazole. The melting point depression at a mixing ratio of 3 : 7 shifts this mixture into a melting point regime similar to ionic liquids and is also considered to feature the characteristic IL properties. Since this mixture is highly hygroscopic, the influence of small water contents on the physicochemical properties was investigated and the incorporation of water into the sample explained with spectroscopical data. For Part 3, the intrinsically disordered protein MBP (basic myelin protein) is mixed with different alkylated imidazolium tetrafluoroborate ILs in varying concentrations and by means of dynamic light scattering, the effect of the IL's transient structures as solvent on the protein structure is examined. MBP is known for only forming tertiary protein structures in the presence of biomembranes, but it could be shown that [BMIm][BF_4] in buffer solution indeed forms defined structures and is able to dissolve the MBP aggregates which possibly can incorporate into the IL structures acting as an "artificial" membrane.

Abbreviations

H(F)C hydro(fluoro)carbons

NMVOC non-methane volatile organic compounds

IL Ionic liquid

TSIL Task-specific ionic liquid

(CW) EPR (Continuous-wave) Electron paramagnetic resonance

TEMPO (2,2,6,6-Tetramethylpiperidin-1-yl)oxyl

EMIm 1-Ethyl-3-methylimidazolium cation

BMIm 1-Butyl-3-methylimidazolium cation

HMIm 1-Hexyl-3-methylimidazolium cation

ChCl Choline chloride

DES Deep-eutectic solvent

MD Molecular dynamics

MSD Mean square displacement

DSC Differential scanning calorimetry

DLS Dynamic light scattering

IDP Intrinsically disordered protein

MBP Basic myelin protein

ss MAS NMR Solid state magic angle spinning nuclear magnetic resonance

PFG NMR Pulse-field gradient nuclear magnetic resonance

Contents

1 Introduction and motivation **1**

2 Fundamentals **4**

2.1 Ionic Liquids 4

2.2 Deep-eutectic solvents 6

2.3 Intrinsically disordered proteins 7

2.3.1 The myelin basic protein 7

2.4 CW EPR spectroscopy 9

2.4.1 The electron spin 9

2.4.2 EPR on nitroxide radicals 10

2.5 Dynamic light scattering 13

2.5.1 Basic principle 13

2.5.2 Autocorrelation and data processing 14

3 Nanoscopic structures and molecular interactions leading to a dystectic and two eutectic points in (EMIm)(Cl)/urea mixtures **16**

3.1 Introduction 16

3.2 Experimental 19

3.2.1 Sample preparation 19

3.2.2 Differential scanning calorimetry 19

3.2.3 X-band CW EPR spectroscopy 19

3.2.4 MD simulation 20

3.2.5 Diffusion NMR & Raman spectroscopy 21

3.3 Results and discussion 21
3.3.1 Differential scanning calorimetry (DSC) 21
3.3.2 Diffusion studies 23
3.3.3 Electron paramagnetic resonance (EPR) spectroscopy 24
The 50 % urea sample 26
The 25 % urea sample 28
The 72.5 % urea sample 30
Comparison of the eutectic and dystectic mixture samples 30
The 12.5 and 37.5 % urea samples 32
The 62.5 and 87.5 % urea samples 33
3.4 Conclusions 35

4 The deep-eutectic choline chloride/imidazole–water mixture – a "porous" liquid 37

4.1 Introduction 37
4.2 Experimental 38
4.2.1 Sample preparation 38
4.2.2 Rheology and density measurements 39
4.2.3 Water uptake 39
4.2.4 NMR studies 40
4.2.5 Electron paramagnetic resonance 40
4.3 Results and discussion 40
4.3.1 Physicochemical properties 40
4.3.2 Spectroscopic analyses 46
EPR spectroscopy 46
Solid state NMR spectroscopy 49
Explanation of the physicochemical properties with spectroscopic findings 51
4.4 Conclusions 55

5 Investigation of structure formation of MBP induced by ionic liquids **58**

5.1 Introduction 58

5.2 Experimental 59

5.2.1 Sample preparation 59

5.2.2 Dynamic light scattering 61

5.2.3 Rheology and refractive index 61

5.3 Results and discussion 61

5.3.1 Dynamic light scattering 61

Characterization of the reference systems 61

MBP in [EMIm][BF_4] 67

MBP in [BMIm][BF_4] 71

MBP in [HMIm][BF_4] 74

Summary 76

5.3.2 Small angle X-ray scattering 78

5.4 Conclusions 78

6 Summary and outlook **80**

7 References **86**

Appendix **A1**

Scientific contributions **vii**

Acknowledgements **viii**

Curriculum vitae **ix**

Declaration of original authorship **x**

1 Introduction and motivation

Over the last decades, efficient and environmental aspects in economy and industry have gained the attention of politics and activists. Decreasing the global greenhouse gas emission and changing over to biodegradable substances in the field of industry and synthetic chemistry have become more and more important.

The era of the Industrial Revolution in Europe and North America has marked the start of the man-made emission of atmospheric greenhouse gases – especially carbon dioxide [2] – with a drastic increase since the 1950s (see Fig. 1.1). Correlating with the increased greenhouse gas concentration is the rise of the mean temperature of the earth [3] (see Fig. 1.1, blue line). Reason for this phenomenon is the greenhouse effect which is a natural occuring effect depending on the fraction of radiation reflected by the earth's surface – the albedo. The reflection of the sun's electromagnetic radiation from the earth's surface can be idealized with the theory of black body radiation. Thereby, an object absorbs irradiated electromagnetic energy and eradiates energy that corresponds solely to the objects temperature. In case of the earth, the emitted electromagnetic radiation is in the infrared spectrum. Small molecules in the atmosphere, such as water vapor, carbon dioxide, methane, nitroxides as well as small hydrocarbons and hydrofluorocarbons absorb and reflect this thermal infrared energy back to the surface instead of letting it pass into space, hence causing a "blanketing effect". Although CO_2 and CH_4 are the most prominent greenhouse gases in the atmosphere (413.4 ppm and 1876.2 ppb, respectively [4,5]), it is mainly the HC and HFC that possess an extraordinary global warming potential (GWP) [6]. The main source for those volatile organic compounds (excl. methane; "NMVOC") are industrial processes, especially the usage of volatile solvents;

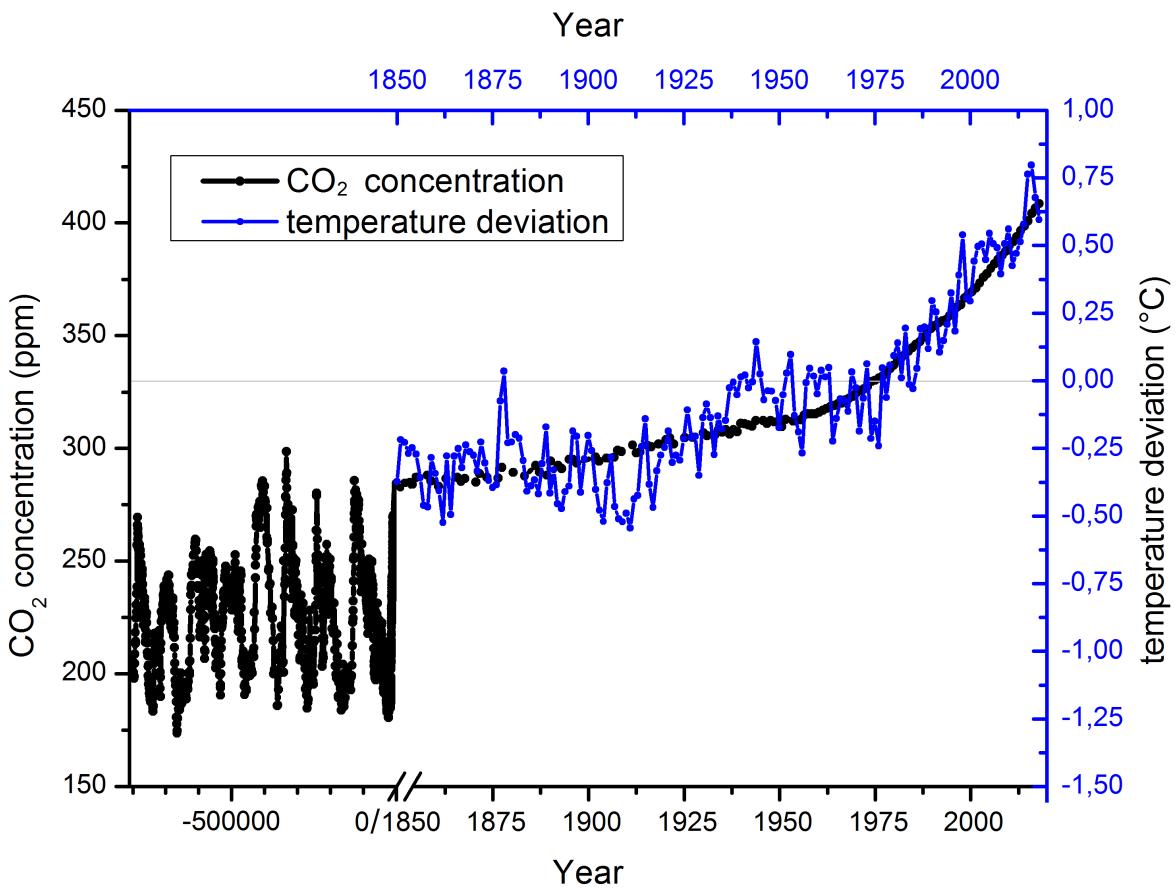

Figure 1.1: Atmospheric CO_2 concentration from $\sim$ 800000 B.C. to 2018 is shown in black. For the deviation of the mean global temperature shown in blue, the average between 1961 and 1990 is used as baseline (light grey).

Fig. 1.2 visualizes the European NMVOC emission to the atmosphere of 2013 and shows that indeed, the pollution from the chemical-industrial solvent use is still an issue[7].

In order for companies to assign their priority in favor for sustainability, science has to provide well-known systems and thoroughly studied concepts. Especially in the field of highly volatile solvents and harmful electrolytes, ionic liquids and ionic liquid-like substances seem to be a promising alternative because of their non-toxicity and low volatility. Furthermore, ILs might find application in medical research due to numerous possible interactions with biopolymers.

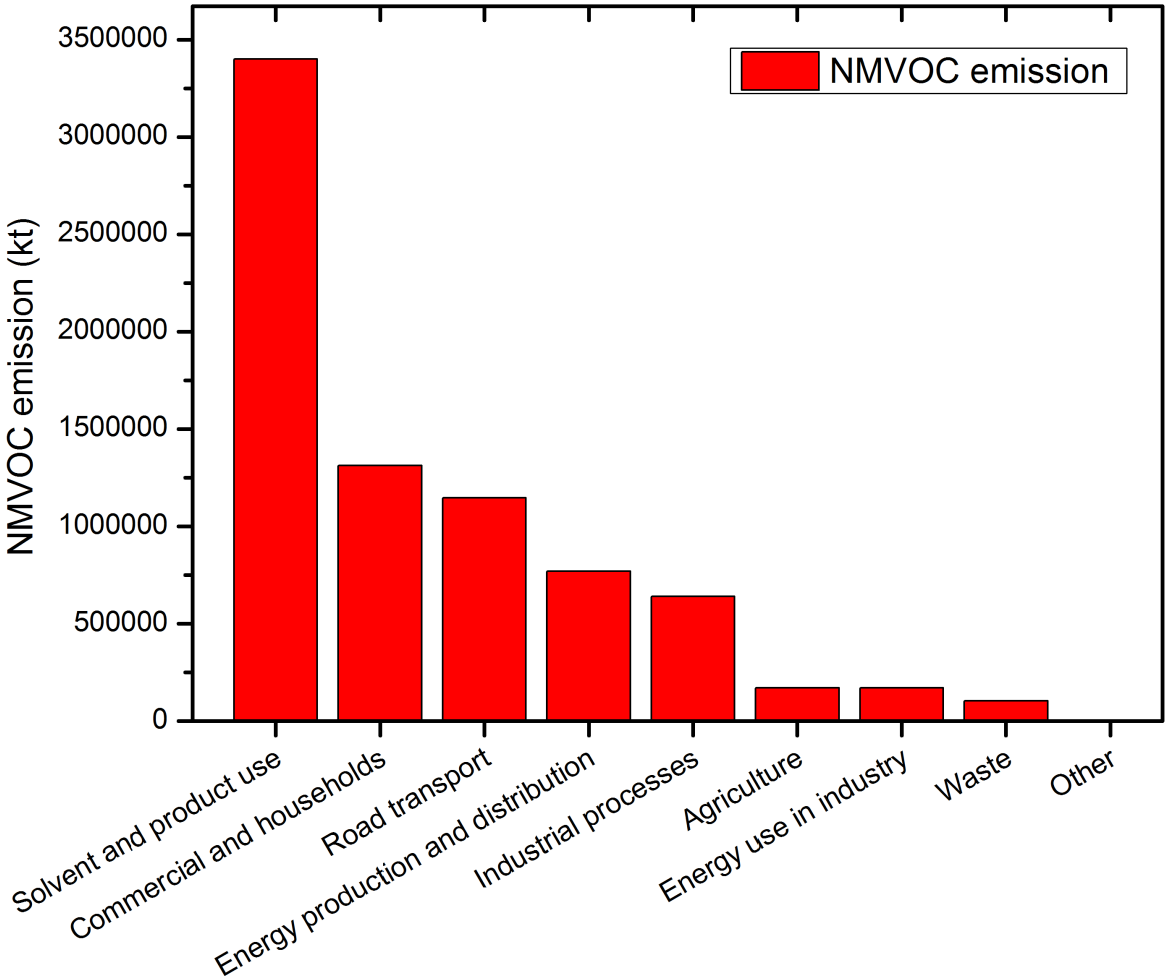

Figure 1.2: European NMVOC emission to the atmosphere in 2011, sorted by sector.

The present study presents three different ionic liquid-based systems investigated under a different approach each: **(1)** a system of 1-ethyl-3-methyl-imidazolium chloride mixed with urea was investigated, especially their nanoscopic structures leading to two eutectic points; **(2)** a eutectic mixture of imidazole and choline chloride was examined regarding its water uptake mechanism; **(3)** a complex system of three 1-alkyl-3-methyl-imidazolium tetrafluoroborate ionic liquids, two buffer solutions and the intrinsically disordered myelin basic protein was analyzed in regard to possible structure formation of the MBP.

2 Fundamentals

This chapter gives an overview into the basic concepts of the investigated solvent systems as well as the two mainly used measurement methods: electron paramagnetic resonance as well as dynamic light scattering.

2.1 Ionic Liquids

Ionic liquids are organic salts with a melting point of below 100 °C, some even below room temperature. This places them in the liquid state under ambient conditions. Thereby, the properties of molten salts are easily accessible under lab conditions: the complete dissociation into ions without the need of a solvent. This highly charged state comes with further unique properties, such as very low vapor pressure, a wide liquid range and broad electrochemical window. The reason for their low melting point is the use of an asymmetric, large organic cation, preventing a close anion–cation interaction and thus crystal formation. Figure 2.1 shows a few examples for cations and anions that can be combined to form ionic liquids.
Viable cations thereby are based on imidazolium, pyrrolidinium, phosphonium, ammonium or other organic core structures. Anions can vary from anorganic and small (halogenides) to bigger anorganic or organic ions such as tetrafluoroborate or triflate and even to more complex anions, *e.g.* lactate or taurinate. This combination of large organic cations with various common anions makes ILs less toxic and some even biogenic. Because of the high amount of possible combinations, as well as the numerous possibilities to modify the ions with functional groups – especially the cations – ionic liquids can be specifically altered in order to draw their maximum potential for the requested task ("task-specific ionic liquids").

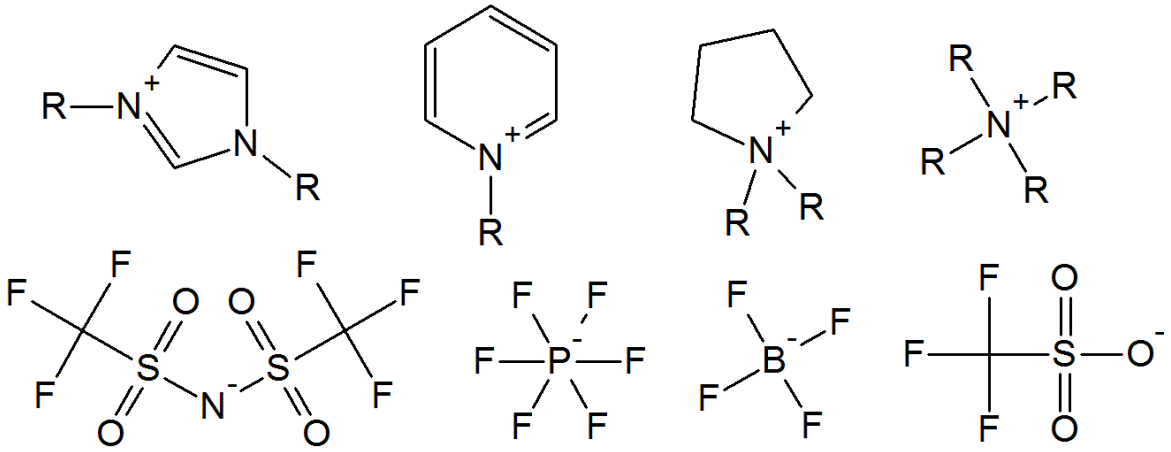

Figure 2.1: Examples of commonly used cations (top row) and anions (bottom row) for ionic liquids.

Due to their negligible volatility and their low toxicity, ionic liquids can prove a viable alternative for conventional solvents and could be used in completely new ways. By the time the first air and water stable ionic liquids were synthesized (imidazolium based, 1992[8]), they had only few application, but quickly became a rapidly growing field of research thereafter. The first applications for ionic liquids were mainly as catalyst and for increasing reaction product yield[9] as well as for efficient removing of impurities and unwanted by-products[10]. Soon, their enormous potential for sustainable and environmentally friendly processes had been discovered, for example their ability to adsorb large amounts of carbon dioxide[11,12] or sulfur dioxide[13]. Especially as alternative for commonly used – and mostly volatile – solvents, ionic liquids have been studied, *e.g.* as solvent in biodiesel synthesis[14].

Because there are so many possibilities to combine anions with cations and to modify them with functional groups, a wide knowledge about the general behavior of ionic liquid properties with various changed parameters and upon mixing with other substances is crucial.

2.2 Deep-eutectic solvents

The concept of melting point depression in eutectic systems can be used to transfer organic salts with higher melting points to the liquid range of ionic liquids solely by mixing them with a hydrogen bond donor. Typical additions are *e.g.* urea or imidazole, which can – when mixed at an ideal ratio – form hydrogen bonds with the organic salt and therefore lower the salts intramolecular COULOMB interaction, hence lowering the overall melting point. The eutectic mixtures formed in that way have been found not only to possess the same melting point range as ionic liquids, but also their unique properties.[15] Figure 2.2 shows an exemplary melting diagram of the eutectic mixture of choline chloride and urea. At the ideal mixing ratio, the melting point of the higher melting choline chloride ($T_{\mathrm{m}} = 302\,°\mathrm{C}$) can be brought down to $18\,°\mathrm{C}$. If such a strong melting point depression can be achieved, these deep-eutectic solvents can be a viable and easy-to-obtain alternative to ionic liquids. In addition, the properties of higher melting salts can be accessed in their liquid state and hence give yet more possibilites to tailor the solvent specifically on their desired function.

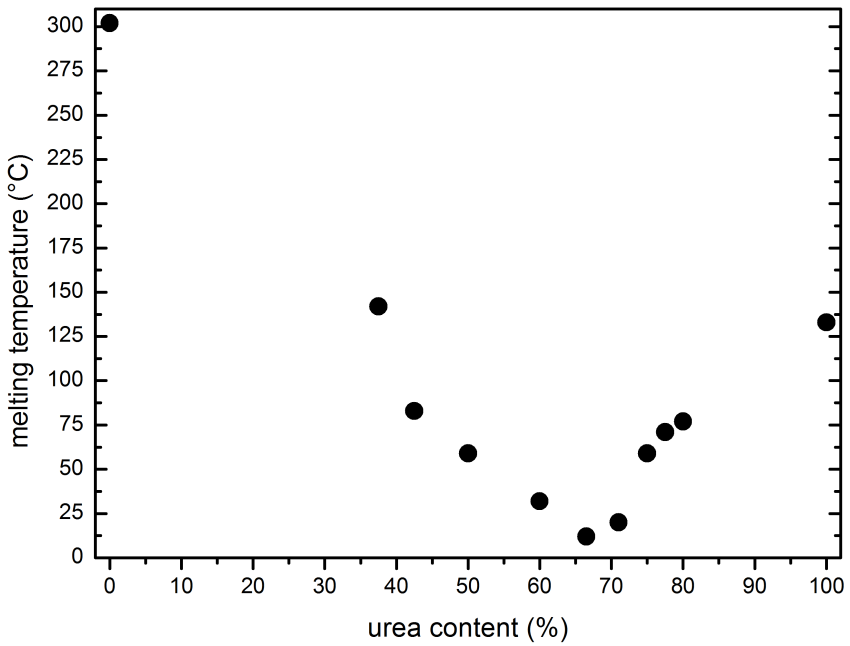

Figure 2.2: Melting points of selected mixing ratios of a choline chloride–urea mixture (data taken from Abbott *et al.*[15]).

2.3 Intrinsically disordered proteins

In Chap. 5, the effect of three different alkylated ILs on the structure of the intrinsic disordered myelin basic protein is investigated. Thereby, a possible application of ionic liquids in medical research is examined and interaction processes with proteins are identified.
Protein structures can be categorized into four different types:

1. Primary protein structure: the way the single amino acid monomers are combined to form the protein;
2. Secondary protein structure: depending on the interplay of the single amino acids, α-helices and β-sheets can form;
3. Tertiary protein structure: the α-helices and β-sheets can interact with each other, in that way, every protein has its very unique conformation;
4. Quarternary protein structure: several folded polypeptide chains can undergo structure formation.

However, there are proteins that show no tertiary structures at all in solution and where no crystal structure has been found yet. They are called intrinsically disordered proteins (IDPs), one of them being the myelin basic protein.

2.3.1 The myelin basic protein

The myelin basic protein (MBP) is a protein with a molecular weight of $\sim$ 18.5 kDa. It is made up of $\sim$ 20 % of the basic amino acids histidine, lysine and arginine. It plays a very important role in the transfer of neural impulses. MBP is an integral part of the myelin sheath that surrounds the axons in the brain[16]. The function of the myelin sheath is the shielding of the inner axon from the electrochemical potential of the surrounding cell to ensure a fast transmission of the neural impulses. Figure 2.3 shows the composition of a neuron cell and a scheme of the amino acid sequence with the secondary structures.

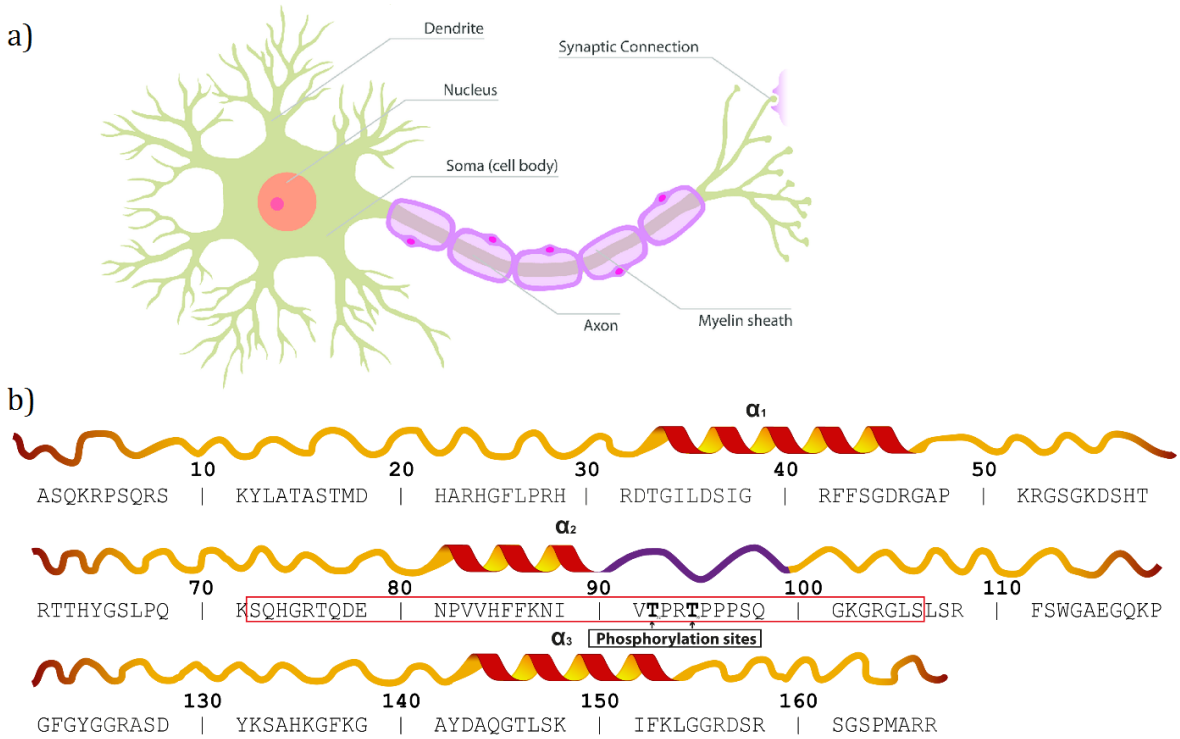

Figure 2.3: **(a)** Structure of a neuron cell taken from Fountas[17]. **(b)** Amino acid sequence of MBP and its secondary protein structure taken from Vassall *et al.*[18].

Although the MBP shows no tertiary structures in solution, its α-helices (*cf.* Figure 2.3b) allow for interaction with lipid double layers[19]. It even acts as a "molecular glue"[20], hence making it an important factor of the integrity of the myelin sheath. It has been found that MBP plays a central role in some neural diseases. The myelin sheath of *e.g.* multiple sclerosis patients show a leakage of MBP[21]. The total net charge of the leaked MBP also differs from "healthy" MBP ($z = +13$ vs. $+19$, respectively) which highly affects their binding affinity to the negatively charged lipids in the cytoplasmic membrane. Detailed knowledge of the structure of MBP and the conditions it needs to be forced into secondary and tertiary structures could be beneficial for multiple sclerosis research.

2.4 CW EPR spectroscopy

Electron paramagnetic resonance spectroscopy measures the resonance frequency of an unpaired electron upon applying an external magnetic field. In contrast to nuclear magnetic resonance, the EPR spectroscopy is very sensitive, which is caused by the very small mass of the electron compared to the nucleus. This means that the EPR signal is very sensitive to the unpaired electron's surrounding. Thus, EPR spectroscopy can give very detailed structure information restricted to a very local area.

2.4.1 The electron spin

In 1922, the physicists O. Stern and W. Gerlach discovered the existence of the electron spin and its quantization by means of their famous experiment of a beam of neutral silver atoms, that split up in two distinctive beams when passing through an external magnetic field. Since the only unpaired electron in the neutral silver atoms is located in an s orbital, the origin of the splitting cannot be the angular momentum which is 0 in this case. Hence, there must be another, quantized state – the electron spin.

In the presence of an external magnetic field, the difference between both states becomes visible, since an electron spin that is in antiparallel direction to the magnetic field is energetically unfavorable. This effect is called electron-ZEEMAN-effect and is visualized in Fig. 2.4I.
The energy difference between the two energetic states corresponds to the resonance frequency. When considering the potential energy of a magnetic dipole, the following resonance condition can be expressed:

$$\Delta E = E\left(m_\mathrm{s} = \frac{1}{2}\right) - E\left(m_\mathrm{s} = -\frac{1}{2}\right) \tag{2.1}$$

$$\Delta E = g \cdot \mu_B \cdot B_0 \tag{2.2}$$

$$h \cdot \nu = g \cdot \mu_B \cdot B_0 \quad \text{with} \tag{2.3}$$

$$\omega_0 = \frac{g \cdot \mu_B \cdot B_0}{\hbar} \tag{2.4}$$

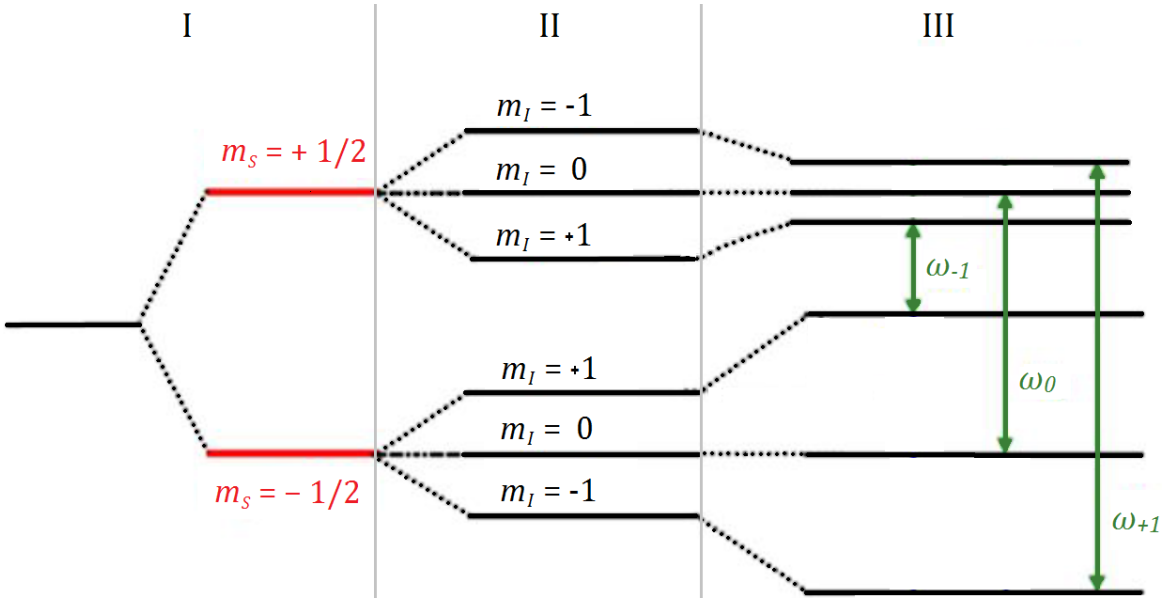

Figure 2.4: ZEEMAN-effect visualized as energy diagram; **(I)** electron spin energy splitting, **(II)** electron spin–orbit coupling, **(III)** allowed transitions.

with μ_B being the BOHR magneton and B_0 being the external magnetic field. While in nuclear magnetic resonance spectroscopy γ is the gyromagnetic ratio, its electronic analog is the g value. For a free electron, the g value is $g_e = 2.0023193043737$. According to Eq. 2.4, for magnetic fields that usually are used in spectrometer technique (0.1–12 T) this gives frequencies in the range of microwave radiation which can be used to induce spin state transition.

2.4.2 EPR on nitroxide radicals

Since the natural occurrence of substances with unpaired electrons is very limited (radical molecules, *d*-transition metals), unpaired electrons have to be introduced to the sample of interest. This can be achieved via spin labelling (covalently bound to the sample) and spin probing (non-covalently added to the sample). A very common method is the use of TEMPO-based radicals as spin probes (see Fig. 2.5a). The respective unpaired electron is located along the O–N axis. Its proximity to the nitrogen nucleus leads to electron–core-interaction.

^{14}N is an $I = 1$ atom and therefore shows a triplet splitting in an external magnetic field (see Fig. 2.4II). The spin–orbit coupling of both of the electron spin states with the three nuclear spin states yields three possible allowed transitions (*cf.* Fig. 2.4III) and hence gives three signals in an EPR spectroscopy experiment. A typical isotropic nitroxide EPR spectrum is shown in Fig. 2.5b.

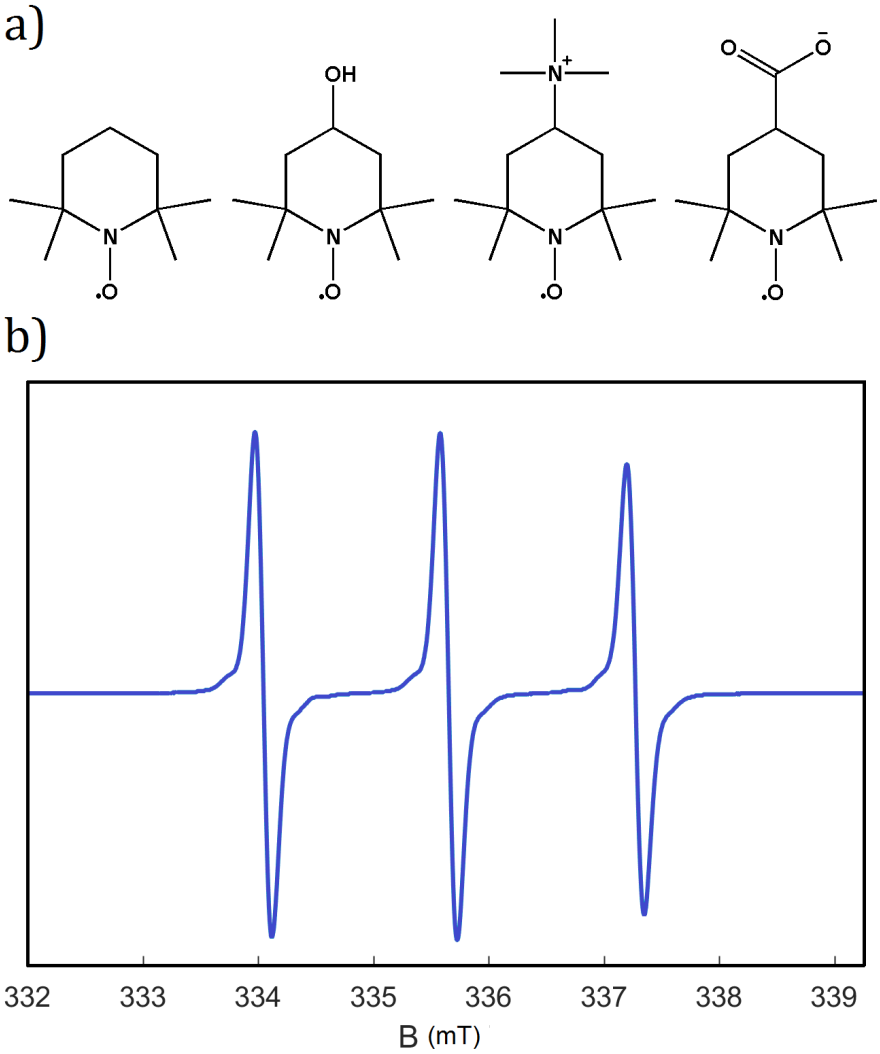

Figure 2.5: **(a)** Selected examples of TEMPO-based nitroxide radicals: TEMPO, hydroxy-TEMPO, amino-TEMPO, carboxy-TEMPO and **(b)** typical isotropic nitroxide triplet EPR signal.

The hyperfine coupling A can be calculated from the peak distances. It is a linear combination of the hyperfine coupling in x, y, and z direction. However, for isotropic rotation the z-component dominates the A value because the respective p_z-orbital is parallel to the magnetic field vector, therefore the term A_{zz} is used. The value of A_{zz} depends on the position of the unpaired electron along the O–N-axis; the closer it is to the ^{14}N nucleus, the stronger is the hyperfine splitting. Thus, A_{zz} is very sensitive to the polarity of the surrounding and can reflect even the smallest changes. In case of decreased rotational isotropy – covalent bonds, non-covalent interactions, increased viscosity of the surrounding, decreased temperature – the x and y components become more present and the spectrum gets distorted. Figure 2.6 shows the typical spectral distortion pattern with decreased rotational isotropy.

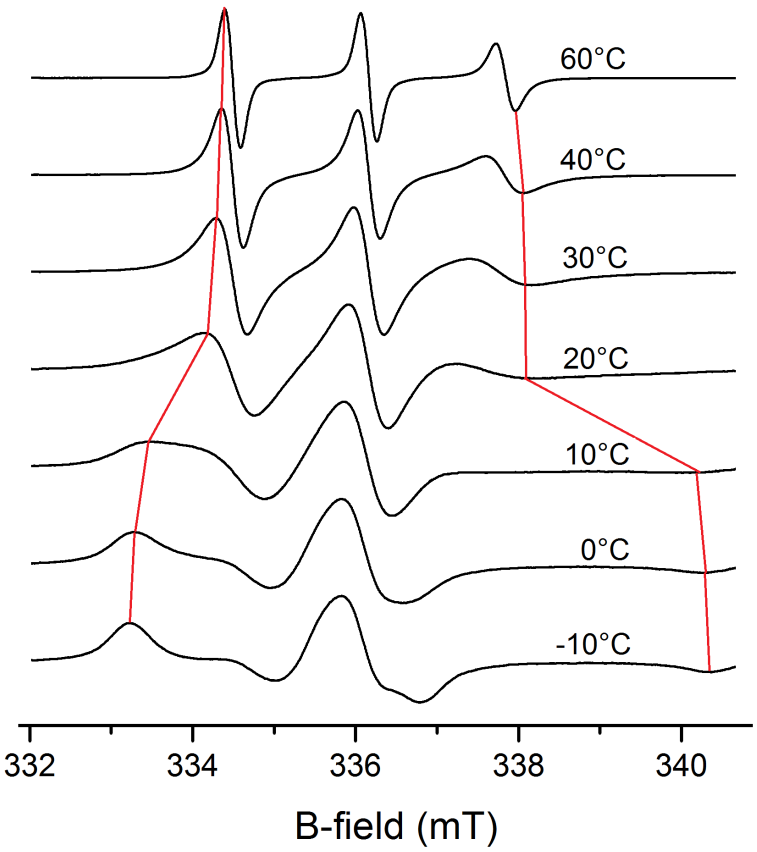

Figure 2.6: Selected TEMPOL spectra for increasing spin probe immobilization, here achieved by decreasing measurement temperature. Progression of the outer extrema separation (A'_{zz}) upon spectral distortion is schematized in red.

When monitoring the expansion of the peaks, conclusion about possible interactions of the spin probe with the sample or the freezing behavior can be drawn. Since TEMPO can be functionalized in many ways (*cf.* Fig. 2.5a), this method especially is suitable for heterogeneous samples. Depending on the possible interactions of the TEMPO-derivates with the sample, different spin probes can be chosen so that they become enriched in different domains of the sample, hence giving structural information about their different surroundings sensed by the unpaired electrons.

2.5 Dynamic light scattering

Dynamic light scattering proves a viable method to evaluate the size of different nanoparticles, which can be proteins, polymers, colloids or other nanostructured materials and is therefore suited well for investigating the structural changes of the MBP in Chap. 5.

2.5.1 Basic principle

Electromagnetic radiation gets scattered from particles which are smaller than the wavelength of the respective radiation. For visible light, this allows for a detection range of colloidal samples and nanoparticles, *i.e.* particles with radii from $\sim$ 1 to 1000 nm. Below 1 nm, sample particles are in the same size range as solvent molecules which is why this is considered as lower limit of the dynamic light scattering method.

When particles move, the DOPPLER principle is valid: the observer detects a frequency shift of the reflected electromagnetic wave that originates from the particle's movement in direction or away from the detector. Thereby, their speed of movement depends on the particle size – the hydrodynamic radius to be more precise, and the viscosity of the dispersion medium. If the viscosity is known, the hydrodynamic radius of the particles could directly be calculated if the frequency shift is measured. However, all particles follow BROWNian motion in their dispersion medium and move with different velocities. This causes fluctuations in the measured scattering light intensities ($I(t)$). The intensities vary around an average value $\langle I \rangle$. With a sufficient long

measuring time, a reliable value for $\langle I \rangle$ can be determined. Information about the particle sizes can be obtained through establishing and analyzing the autocorrelation.

2.5.2 Autocorrelation and data processing

The autocorrelation in DLS is a measure for a relating connection of positions, velocities and directions of motion of particles between a time t and a later time step $t + \tau$. In contrast to static light scattering methods where $\langle I \rangle$ is calculated between the two time steps t_0 and t_{end}, dynamical light scattering uses several very small time steps τ for which $\langle I \rangle$ is calculated each. For n very small time steps τ, following equation can be used to express the autocorrelation:

$$\langle I(t) + I(t+\tau) \rangle = \lim_{t_n \to \infty} \frac{1}{t_n} \int_{t_0}^{t_n} I(t) + I(t+\tau) \mathrm{d}t \tag{2.5}$$

Divided by $\langle I \rangle^2$ yields the intensity–time-correlation function and also dictates its co-domain to be ≥ 1. Figure 2.7 visualizes a typical autocorrelation function which shows an exponential decay. The modality of its decay gives information about the diffusion behavior of the particles.

The transformation from the autocorrelation to the particle size distribution is done with the program package Kalliope by Anton Paar where the *cumulant* analysis method is applied – a monomodal ditribution method. The exponential autocorrelation decay $g(\tau)$ is fitted with Eq. 2.6 and the exponential coefficient k, together with known viscosity η and refractive index n of the sample as well as the spectrometer wavelenght λ and scattering angle θ, is used to calculate an intensity-weighted particle size (*i.e.* the hydrodynamic radius R_{H}) distribution by means of the Stokes–Einstein-equation (Eq. 2.8):

$$g(\tau) = e^{-k\tau} \tag{2.6}$$

$$k = D \cdot \frac{4\pi n}{\lambda} \cdot \sin \frac{\theta}{2} \tag{2.7}$$

$$D = \frac{k_{\text{B}T}}{6\pi\eta R_{\text{H}}} \tag{2.8}$$

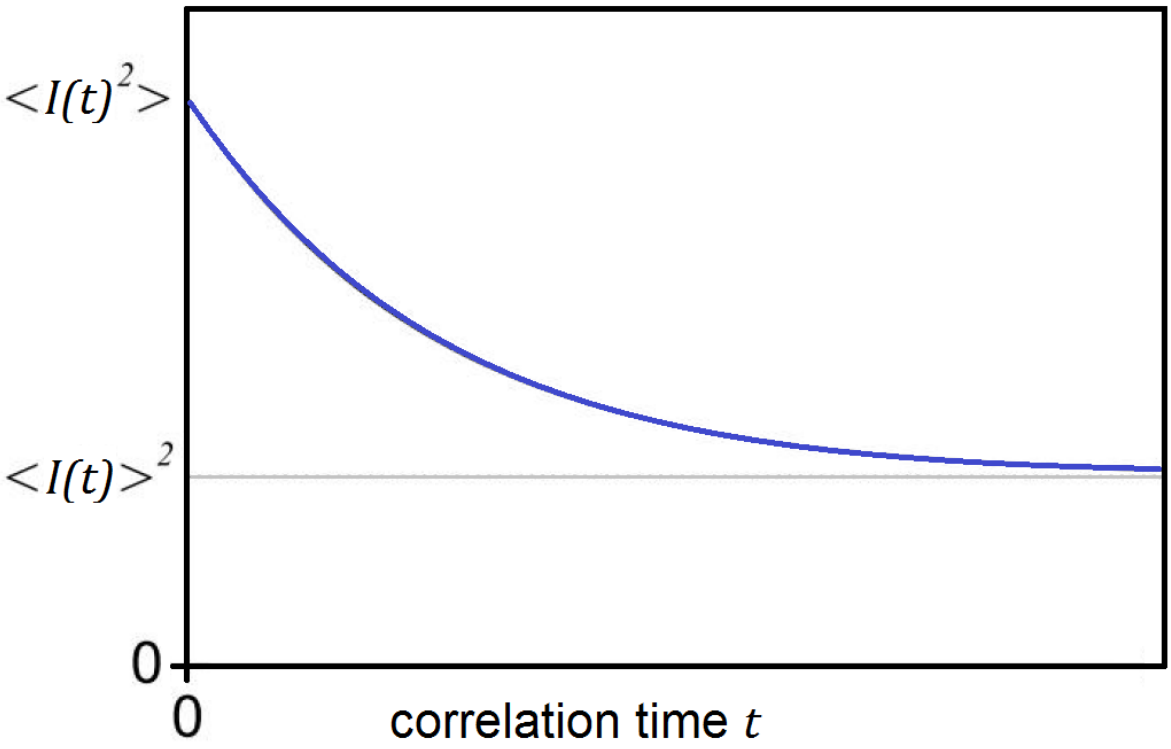

Figure 2.7: Typical shape of the autocorrelation $\langle I(t) + I(t+\tau)\rangle$.

3 Nanoscopic structures and molecular interactions leading to a dystectic and two eutectic points in (EMIm)(Cl)/urea mixtures

3.1 Introduction

The aim of this study is to investigate a mixture of urea (Fig. 3.1(**1**)) and the IL 1-ethyl-3-methyl-imidazolium chloride ([EMIm][Cl], Fig. 3.1(**4**)) and to understand its nanostructure and molecular dynamics. In particular, we compare these to the nanostructure of common molecular solvents on the one hand and ionic liquids on the other hand. A previous study by Tsuda et al. has shown that this mixture forms a dystectic system with two eutectic points at 25 and 72.5 % urea content respectively[22] (see Fig. 3.2a).

The eutectic melting points of both mixing ratios seem to be very similar, at 58 and 62 °C, respectively. In this previous study, the basic physicochemical properties of both samples were measured and compared to find out if they behave as a common molecular solvent or rather as an ionic liquid. Former studies showed that all DES of the type salt/HBA have structural and/or dynamic heterogeneities to some extent, while neutral DES of the type HBD/HBA (e.g. acetamide/urea) do not.[23] Here, we use PFG NMR spectroscopy to quantitate mobility of all chemical components individually. Analysis of the dynamic properties are supported with molecular dynamics simulation. For detailed nanoscopic insights, we use electron

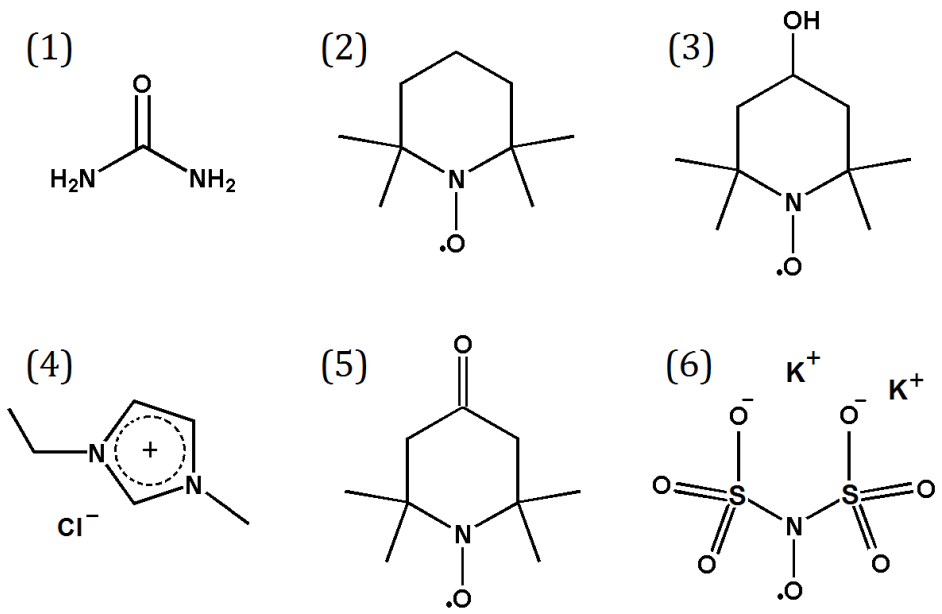

Figure 3.1: Used substances and spin probe molecules: urea **(1)**, TEMPO **(2)**, TEMPOL **(3)**, [EMIm][Cl] **(4)**, TEMPONE **(5)**, Frémy's salt **(6)**.

paramagnetic resonance (EPR) spectroscopy on nitroxide spin probes of different chemical substitutions that are used as paramagnetic tracers in the DES mixtures. With EPR spectroscopy, we particularly study the effect of the DES nanostructure on the environment and rotational dynamics of these spin probes.

Since the mixture itself does not contain EPR-active molecules with unpaired electrons, it is doped with persistent radicals, called spin probes. An EPR spectrum is very sensitive to the chemical character of the unpaired electron's direct surrounding (esp. polarity, H bonding). The spin probes used in this study are shown in Fig. 3.1: TEMPO (**(2)**), TEMPOL (**(3)**), TEMPONE (**(5)**) and Frémy's salt (**(6)**). Each spin probe contains different functional groups, so that they have different interaction patterns with the solvent molecules as already observed, e.g. by Akdogan et al.[24] The method employs spin probes preferentially partitioning into one domain of a nano-segregated sample. Nano-segregation has been known in ionic liquid-like solvents as shown via X-ray/neutron diffraction.[25] A similar probing method has already been performed with fluorescence spectroscopy by Hossain et al.[26] These authors

used ionic probe molecules in DES for the first time to obtain information on dynamic micro-heterogeneities, which they indeed found and characterized them as being non-static.

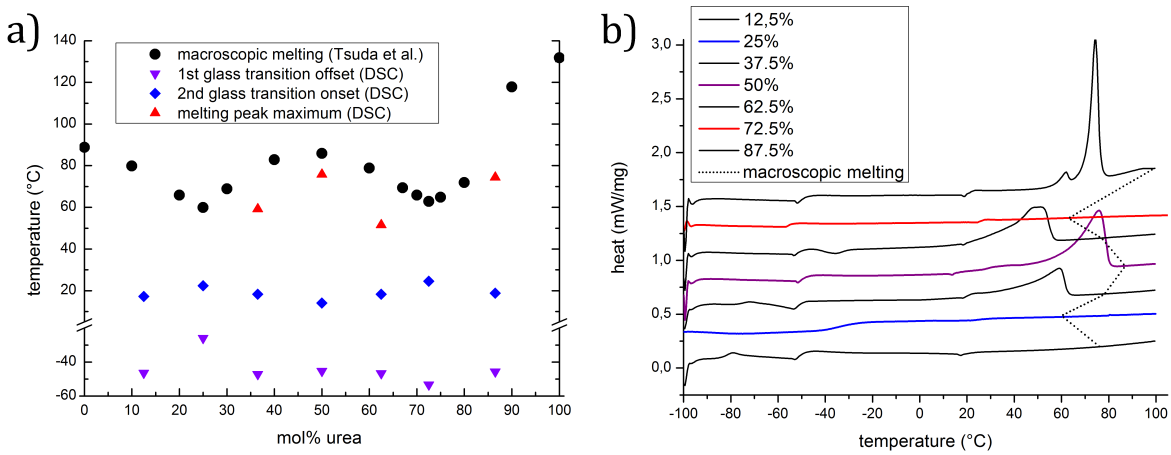

Figure 3.2: **a)** Melting diagram of [EMIm][Cl]–urea with macroscopic melting points (black dots, data adapted from Tsuda et al.) as well as DSC $T_{\mathrm{g1,offset}}$ (purple downward triangles), $T_{\mathrm{g2,onset}}$ (blue diamonds), and $T_{\mathrm{m,max}}$ (red triangles). **b)** DSC heating curves at $5\,\mathrm{K\,min^{-1}}$ of the 25 % (blue), 50 % (purple), 72.5 % (red) urea mixtures as well as the heating curves of selected mixing ratios in between (black).

In general, EPR spectroscopy has been proven to be a powerful method to investigate microviscosity and micropolarity, as well as microscopic/nanoscopic bulk structure. Several research groups have already used EPR for assessing the viscosity[27] and phase transitions[20] of ILs, as well as their polarity.[28] One of the most important characteristics for this study is the A'_{zz} value, the spectral separation of the two outermost extrema (at the low-field and high-field ends, respectively) of the measured nitroxide radical spectra and denotes the ^{14}N hyperfine coupling value along the long axis of the unpaired electron-bearing p orbital. For freely and fast moving nitroxide radical molecules, the individual spin state transition of all 3 spatial directions is averaged out – an isotropic triplet spectrum is observed.[29] With reduced mobility, the triplet spectrum gets distorted and the outer extrema separation increases rapidly when

approaching a rotational correlation time of $\tau_c = 2$–$5\,\mathrm{ns}$. This jump in the A'_{zz} values of a temperature series can be used to observe the radical molecule's immobilization temperature which is highly dependent on the freezing immobilization of the radical's surrounding. Furthermore a quantitative analysis of A'_{zz} delivers insights in the polarity and thus the preferred radical enrichment domains. Figure 2.6 shown above depicts how spin probe immobilization affects the spectra and hence the A'_{zz} values.

3.2 Experimental

3.2.1 Sample preparation

Both pure substances [EMIm][Cl] (1-ethyl-2-methylimidazolium chloride, 98 % Sigma Aldrich) and urea were freeze-dried under vacuum for not shorter than 24 h before use. All sample mixtures are denoted by their urea content (e.g. 25 %). TEMPO (2,2,6,6-tetramethylpiperidine-1-oxyl, 98 %, Sigma Aldrich), TEMPOL (4-hydroxy-TEMPO, 98 %, Sigma Aldrich), TEMPONE (4-oxo-TEMPO, 98 %, Alfa Aesar) and Frémy's salt (potassium nitrosodisulfonate, 98 %, Sigma Aldrich) were used as received.

3.2.2 Differential scanning calorimetry

DSC measurements were performed at a Netzsch 204F1 Phoenix device. An initial weight of $\sim$ 10 mg each sample was inserted into a metal cup. A heating rate of $5\,\mathrm{K\,min^{-1}}$ was applied and the samples were measured in a one cycle cooling and heating from +100 to −100 °C.

3.2.3 X-band CW EPR spectroscopy

A Miniscope MS400 benchtop EPR spectrometer (magnettech GmbH, Berlin) was used for EPR spectroscopy. The samples were doped with four different spin probes, each with a concentration of $\sim$ $1\,\mathrm{mg\,ml^{-1}}$. Around 50 µl of the sample was inserted into a quartz capillary (Blaubrand) and sealed. The magnetic center field was set to 336 mT with a scan sweep of 15 mT. Modulation and microwave attenuation were set to 0.02 mT and 20 dB, respectively for all TEMPO-based spin probes. For Frémy's salt, slightly different parameters were used, a

scan sweep of 10 mT, modulation of 0.01 mT and a micowave attenuation of 15 dB. In analogy to the DSC measurements, cooling and subsequently heating from +100 to −100 back to +100 °C was performed and an EPR spectrum was recorded every 10 K. They were then analyzed with the EasySpin[30] package for MatLab (Mathworks, Inc.). All simulations are based on the stochastic LIOUVILLE–VON NEUMANN-equation which allows the extraction of the rotational diffusion coefficients including its anisotropies. The required input parameters are spin system, g and hyperfine (A) tensor elements for the three spatial directions as well as measurement settings: center B field, B field sweep, microwave frequency, reference microwave phase and modulation amplitude. After adjusting the ratio of GAUSSIAN to LORENTZIAN peak shape to exactly match the shape of the measured spectra peaks, the individual rotational diffusion tensor elements have to be manually entered and adjusted several times until the simulation matches the spectra (see Appendix Fig. A5). The diffusion tensor elements then can be used to calculate the rotational correlation time τ_c as a simplified figure.

3.2.4 MD simulation

For each experiment, a system of 512 ion pairs was investigated and the MD simulation was performed with the LAMMPS program package.[31] The density was obtained via NPT equilibrium simulation of 2 ns run time and the force field parameters for $[EMIM]^+$ as well as $[Cl]^-$ were taken from Canongia Lopes and Pádua,[32] while those for urea were obtained from the OPLS–AA force field.[33] In general, MD systems are calculated with temperatures set at $\sim$ 400 K to massivly reduce calculation time while collecting dynamic data. In our study, the system temperature was set to 358 K in order to allow a comparison to experimental data, especially to the viscosities.. The NOSÉ–HOOVER chain thermostat[34] and barostat were attached for all calculations, short-range LENNARD-JONES and COULOMB interactions were computed up to 1000 pm and the long range electrostatic interaction established via PPPM method. The full simulation run time was 20 ns with a time step of 0.5 fs, thereby, the positions and energies of all atoms were excerpted every 10 ps to gain the final trajectory set. All results were gained through the use of the trajectory analyzer program TRAVIS.[35]

3.2.5 Diffusion NMR & Raman spectroscopy

Self-diffusion coefficients were determined via NMR experiments at 70 °C on a Bruker spectrometer with the resonance frequency at 400 MHz for protons using the Diff60 probehead. The standard stimulated-echo pulse sequence was employed.[36] Raman spectra were recorded with an inVia Raman microscope by Renishaw with Cobolt cw DPSS laser excitation at 532 nm wavelength. The samples were placed on a gold plate and measured quickly.

3.3 Results and discussion

3.3.1 Differential scanning calorimetry (DSC)

Differential scanning calorimetry is a fast and simple method to obtain an overview of structure-related thermodynamic differences of a sample set. The samples were heated at 5 K min^{-1} and deviations from the known heating curve were plotted against the actual temperature which ranged from −100 to +100 °C. Such, energy consumption or release due to phase transitions at certain temperatures can be made visible. As it can be seen in Fig. 3.2b, all samples feature two glass transitions, appearing as a step in the heat baseline. Additionally, all samples except the 12.5, 25 and 72.5 % mixtures show an endothermic melting peak as well. The following Table 3.1 summarizes selected onset/offset/maximum temperatures of the DSC transitions for every sample.

All samples show two glass transitions, the first at $\sim$ −50 °C and the second at $\sim$20 °C. Since there are no glass transitions visible for pure [EMIm][Cl],[37] they originate from the interactions and structures after the mixing of both substances. For the 37.5, 50, 62.5 and 87.5 % mixtures, an endothermic melting peak can be observed which shows the same trend as the macroscopic melting points. Interestingly, the mixture with the highest [EMIm][Cl] content and both eutectic mixing ratio samples do not feature a melting peak.

When comparing the first glass transition temperatures, both eutectic mixing ratio samples show a deviation, too. The 25 % urea sample shows a shift of $\sim$ 20 K to higher temperatures

Table 3.1: Glass transition onset/offset temperatures and melting peak maximum temperatures for all samples.

Sample	1st T_g onset	1st T_g offset	2nd T_g onset	T_m max
12.5 %	−52.4 °C	−46.4 °C	17.2 °C	–
25.0 %	−40.1 °C	−26.0 °C	22.4 °C	–
37.5 %	−53.1 °C	−47.2 °C	18.3 °C	59.2 °C
50.0 %	−51.7 °C	−45.3 °C	14.1 °C	75.8 °C
62.5 %	−53.1 °C	−46.7 °C	18.3 °C	51.6 °C
72.5 %	−56.4 °C	−53.4 °C	24.5 °C	–
87.5 %	−51.7 °C	−45.7 °C	18.8 °C	74.4 °C

(*i.e.* enforcement of the underlying interactions), whereas the 72.5 % urea sample shows a shift of $\sim$ 8 K to lower temperatures (*i.e.* weakening of the underlying interactions). Glass transition temperatures of DES already have been proven to have the same trend as their viscosities.[38] These authors investigated proline-based DES with different water contents and their DSC measurements showed only glass and no phase transitions, hence the T_g trends and viscosity trends are correlated. The temperature difference between the 25 % and 72.5 % urea mixture is indeed in agreement with viscosity data and mean square displacement analysis, where the 25 % urea sample shows a generally higher viscosity and lower molecular mobility (see Appendix Fig. A1). Furthermore, molecular dynamics simulation and subsequential radial distribution function analysis allow the conclusion that the urea-$NH_2 \cdots Cl^-$ interaction is the strongest (see Appendix Fig. A2). This would explain the glass transition temperature shifts and viscosity/mobility observations, since the 25 % urea mixture sample provides an excess of Cl^- so that both NH_2 groups of urea can form hydrogen bonds and thus strengthen the interaction network. An excess of the ionic liquid [EMIm][Cl] furthermore leads to a very weak, broad and indistinct transition, which can be seen when comparing the 25 % urea sample's DSC curve with the other samples.

The second glass transition however has a similar value for both eutectic mixing ratio samples with a difference of only 2 K, which is also seen in their similar macroscopic melting points.

Interestingly, the 72.5 % urea sample does not feature a melting peak although pure urea is a highly crystalline substance. Therefore, Raman spectroscopy was performed and the results in Fig. 3.4 show that the bands originating from free urea are of very low intensity or even completely missing. This is in agreement with former Raman studies of *e.g.* Hou et al.[39] They proposed that the main reason for the melting point depression lies in anion–N interaction (with the added neutral molecule $N =$ urea, imidazole or carboxylic acid). In this study, only urea is used as neutral molecule, which contains two different polar groups (C=O and NH_2) which can interact with the surrounding IL and hence weaken its COULOMB interactions.

3.3.2 Diffusion studies

To shed light on the cause of the difference in first glass transitions and the reason for the similarities in the second glass transition temperatures, each component was investigated regarding its mobility of the unique components in the 25 % and 72.5 % urea mixtures. To this end, diffusion (PFG) NMR measurements and the mean square displacement data of our molecular dynamics simulations were combined.

As Fig. 3.3 shows, the particles in the 72.5 % urea mixture generally have a larger MSD, indicating a higher mobility. This is also in agreement with the viscosity data and the low first glass transition temperature in DSC. When inspecting the individual components, urea shows smaller displacements in the 25 % urea mixture compared to $[EMIm]^+$ and higher displacements in the 72.5 % mixture compared to $[EMIm]^+$. Apparently, the respective excess components are more mobile at the eutectic points. Experimentally, diffusion NMR spectroscopy gives direct access to the self-diffusion coefficients. These are in remarkably good agreement with the MD simulation results: sample 72.5 %: urea $5.75\,m^2\,s^{-1}$, $[EMIm]^+$ $5.4\,m^2\,s^{-1}$, sample 25 %: urea $4.02\,m^2\,s^{-1}$, $[EMIm]^+$ $4.14\,m^2\,s^{-1}$. Although counterintuitive at first sight, the diffusion coefficients are in fact quite independent on their molecular size

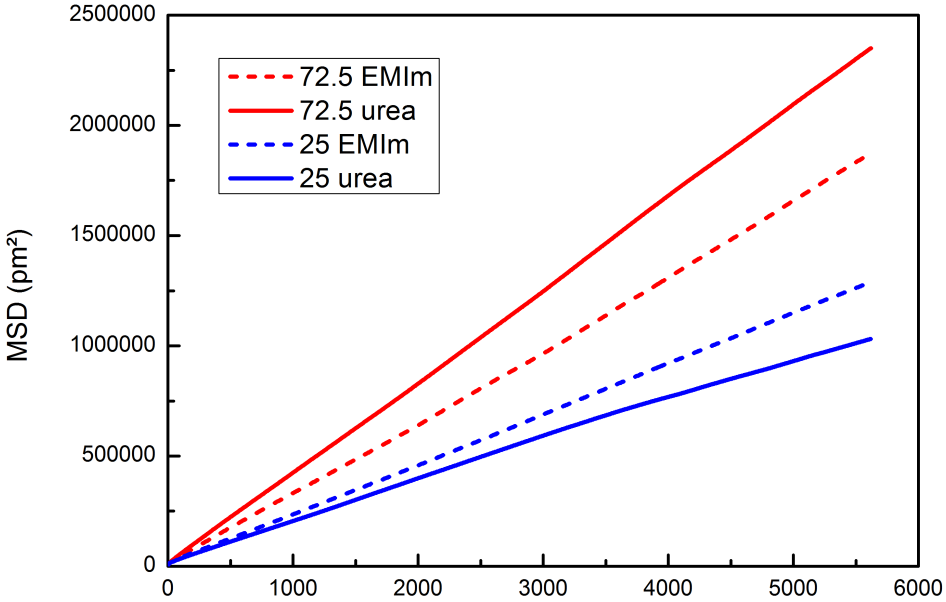

Figure 3.3: Mean square displacements of the urea and $[EMIm]^+$ molecules for both mixing ratios extracted from the trajectory of the molecular dynamics simulation.

and mostly reflect the component's ability to form hydrogen bonds, which has been studied before.[40,41] Hayamizu et al. performed diffusion NMR studies on the binary mixture $[EMIm][BF_4]/LiBF_4$ and showed a higher ion mobility for the $[EMIm]^+$ cation than for the much smaller lithium cation.

The 72.5 % urea sample shows a high urea mobility although pure urea is well known for its high crystallinity. Interpretation of this finding is aided by Raman spectra of the different mixtures and pure substances (Fig. 3.4). In the 72.5 % sample, remarkably little of the pure urea bands (seered vs. black trace) are visible, presumably due to a strong hydrogen bond network. These interactions have already been identified as the underlying reason for dynamic properties by means of fluorescence spectroscopy.[42]

3.3.3 Electron paramagnetic resonance (EPR) spectroscopy

For the EPR spectroscopic measurements, spin probe molecules with different functional groups have been chosen that can interact with different components in the [EMIm][Cl]–urea

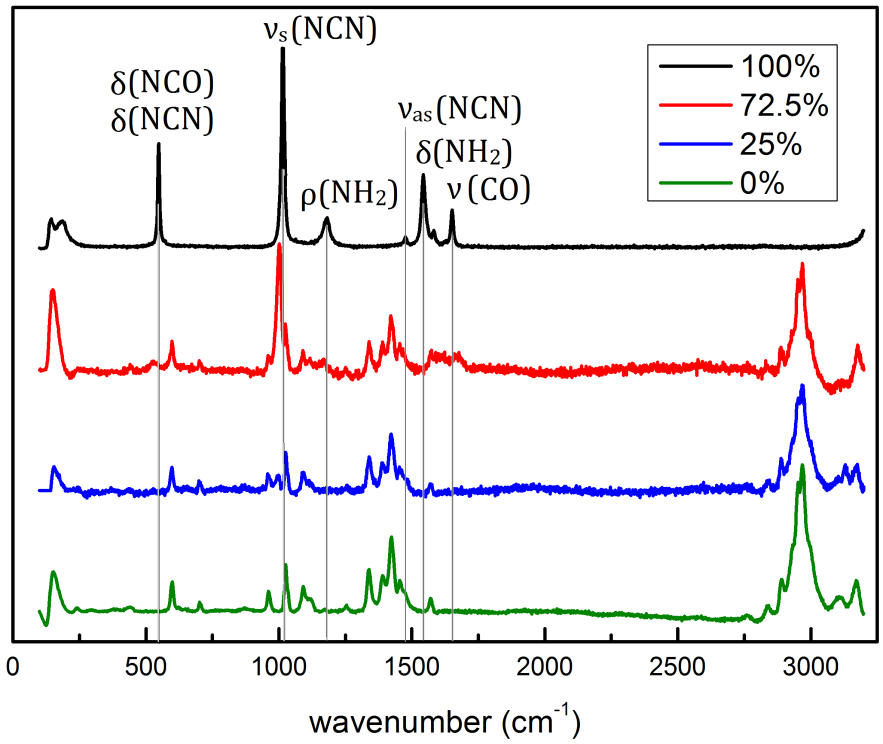

Figure 3.4: Raman spectra of the pure components as well as the 25 % and 72.5 % urea mixture, respectively. Grey vertical lines indicate the position of different bands of the pure urea with the respective vibrational modes.

matrix. In case of microheterogeneity of the matrix, these interactions lead to a different enrichment of each spin probe in the nano-segregated domains. These nanoscopic domains then become manifest through different immobilization temperatures and polarities of the environment as seen in the hyperfine coupling. The underlying effect of the formation of domains on the spin probes has already been studied and described by means of high-field and standard EPR spectroscopy before.[24,20] Representative EPR spectra in the 25 %, 50 % and 72.5 % mixtures are shown in Fig. 3.5, the extracted A'_{zz} vs. temperature plots of the various spin probes in the different mixtures are summarized in Figs. 3.6 and 3.7 and the Appendix. We now discuss and interpret the EPR spectroscopic data (Fig. 3.5), in the framework of information obtained from the other methods so far. We have chosen to graphically illustrate the findings on the nanostructure and dynamics of the sample using representative snapshots

from the MD simulation, which are depicted in Fig. 3.8. For reference, all spin probes were also measured in pure [EMIm][Cl]. Due to a high melting point, reference measurements in pure urea were not possible, since the TEMPO-based spin probes are thermally instable above $\sim$ 100°C and solid mixing led to high concentration heterogeneity and precluded EPR spectroscopic analysis. Figure 3.5 gives an overview of all the relevant mixing ratio sample spectra. Pure [EMIm][Cl] shows formation of nano-domains itself,[43,20] spectroscopic deviations to the other samples hence give hints on the structural changes caused by the mixing of urea. The A'_{zz} vs. T progression typically shows a jump to higher values with decreasing temperature, indicating the spin probe's immobilization accompanied by the visible spectral anisotropy. The immobilization temperature is dependent on the interactions of the spin probe molecule with the matrix molecules as well as on freezing of the spin probe's surrounding – which can give information about the presence of different domains. A comparison of the three TEMPO-based spin probes in the reference sample of pure [EMIm][Cl] (see Fig. 3.6b, black curves) shows that TEMPO has the lowest immobilization temperature, presumably due to its lack of functional groups which can interact with the [EMIm][Cl] molecules, followed by TEMPONE with its keto-group and then TEMPOL with its hydroxyl-group. We now discuss the EPR-derived data for the unique sample sets individually.

The 50 % urea sample

The 50 % urea sample features a local melting point maximum – the dystectic point in the temperature–composition phase diagram. It is caused by structural ordering which becomes present only at a 1 : 1 mixing ratio. The temperature-dependent A'_{zz} values of TEMPO, TEMPOL and TEMPONE, respectively in the 50 % mixture are shown in Fig. 3.6b (purple curves). Note that we have plotted the 0 % urea sample in Fig. 3.6b, for better comparison with the 25 % and 72.5 % samples, vertical lines show the position of −40, −20 and +20 °C. The curve progression – jump temperature as well as absolute A'_{zz} values – is very similar for all three TEMPO-based spin probes. Thus, a homogeneous distribution of all spin probes and hence in return of [EMIm][Cl] and urea can be assumed. Interestingly, all TEMPO-based spin probes stay mobile for much longer during probe cooling compared to the reference sample. It

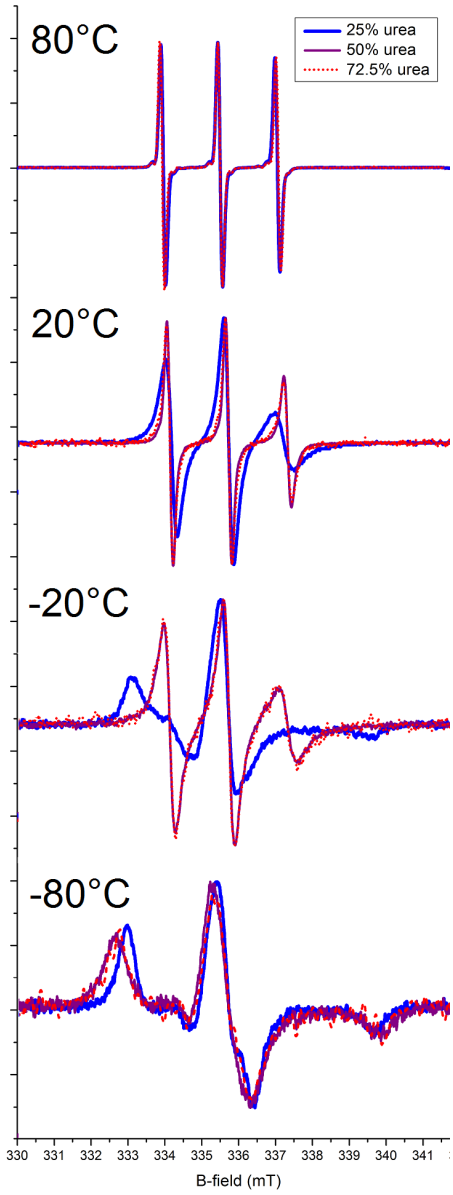

Figure 3.5: CW EPR spectra of TEMPO in the 25 % (blue), 50 % (purple) and 72.5 % (red) mixtures for different temperatures.

seems that specific interactions between the functional groups of spin probes and the solvent are prevented. This may be due to the complete saturation of available [EMIm][Cl] interaction sites by the added urea, causing a very stable structure and hence a melting point maximum. The transition from isotropic rotation (low A'_{zz} values – a_{iso}) to slow tumbling (high A'_{zz}

values) happens at temperatures of $\sim -45\,^{\circ}\mathrm{C}$ which correlates well with the onset of the first glass transition in DSC (*cf.* Tab. 3.1). Apparently, the 1 : 1 [EMIm][Cl] : urea mixture forms a specific structural network which is the cause for the first glass transition and the high macroscopic melting point, and for solute molecules it acts as a molecular solvent.

A quantitative analysis of A'_{zz} values can give hints on the polarity of the matrix, since the position of the unpaired radical electron along the N–O bond and hence the nitrogen hyperfine coupling/triplet peak splitting is altered in presence of electronegative/-positive atoms and polar groups within range[24,44]. Thereby, nitroxide radicals show low A'_{zz} values in non-polar domains and high A'_{zz} values in polar domains. The alkyl chains of the $[\mathrm{EMIm}]^+$ cation are the only groups that can be considered to be of low polarity.

The absolute A'_{zz} values for Frémy's salt are much lower and the transition temperature is approx. 40 K higher compared to the TEMPO-based spin probes. Due to the fact that Frémy's salt dianion is introduced into the charged ionic liquid matrix, Coulomb interaction leads to an enrichment around the $[\mathrm{EMIm}]^+$ cation as well as a very early immobilization during sample cooling. The very proximity of the nitroxide group to the cation's alkyl chains can explain the low A'_{zz} values as compared to its appropriate reference systems.

The 25 % urea sample

Both eutectic mixing ratios 25 and 72.5 % show an macroscopic melting point depression to $\sim 60\,^{\circ}\mathrm{C}$. Nevertheless, despite the very similar melting points, their A'_{zz} vs. T plots differ from each other as well as from that of the 50 % urea sample.

Figure 3.6a compares the 50 % urea sample with the eutectic 25 % urea mixture (TEMPO-based spin probes only). The immobilization temperatures in the eutectic mixture are shifted approx. 50–60 K to higher values (*cf.* first glass transition temperature shift also to higher values, Tab. 3.1). The transition temperatures for the respective spin probes in the 25 % mixture themselves span $\sim$ 20 K (midpoint between 0 and 20 °C) and the A'_{zz} values in the frozen state are identical (3.5 mT).

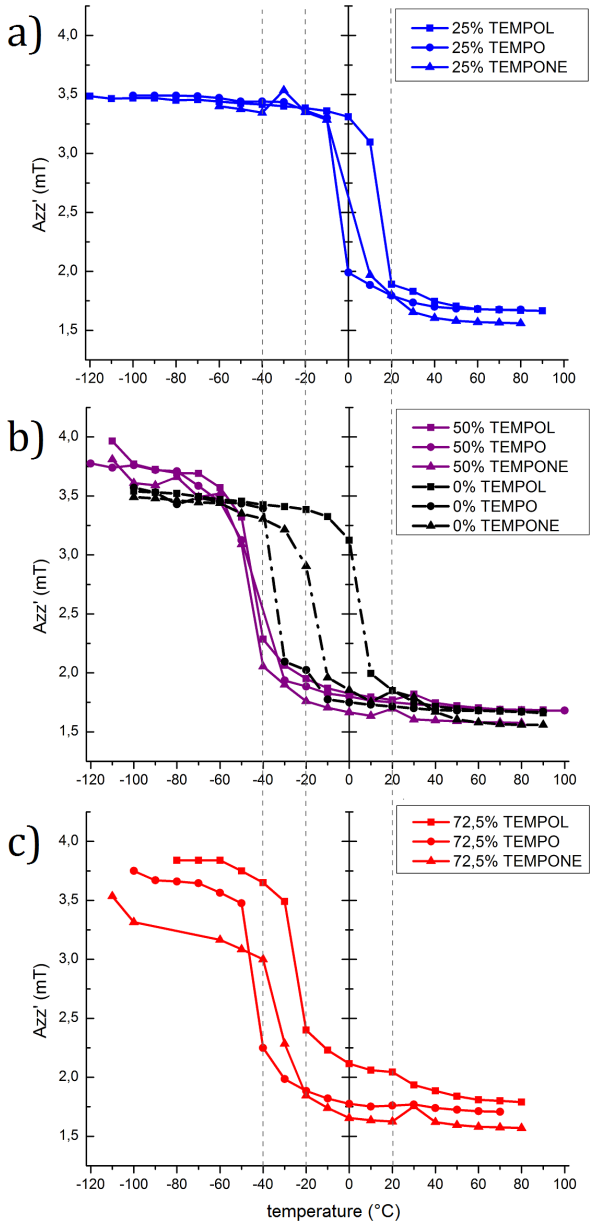

Figure 3.6: A'_{zz} curves for the 25 (blue, panel **a**), 0 and 50 (black and violet, panel **b**), and 72.5 (red, dotted, panel **c**) % urea samples each doped with the nitroxide spin probe TEMPOL (squares), TEMPO (circles), and TEMPONE (triangles). Note that a grey dashed line denotes the temperatures −40, −20, and 20 °C allowing for better comparison.

Since the three T–A'_{zz} plots for the 25 % urea sample form a group similar to the 50 % urea sample, from the probe's point of view a homogeneous DES phase that integrates the excess component (when compared to the 50 % mixture) [EMIm][Cl] seems to be formed and no nano-segregation into domains can be deduced, as otherwise the different spin probes should experience different surroundings. The excess chloride anions further enforce the urea-$NH_2 \cdots Cl^-$ network which is the reason for the stronger immobilization and higher first glass transition temperatures. The excess imidazolium cation however cannot form separate domains due to COULOMB repulsion and are mixed into the sample homogeneously. Further, the excess imidazolium cations might form the pseudo-fluid phase caused by the weakening of the $[EMIm]^+ \cdots Cl$ COULOMB attractions due to extensive hydrogen bonding of the chloride anion with urea. The diffusion constants and mean square displacements support this interpretation, meaning that the low optical melting point is governed by this fluid phase.

The 72.5 % urea sample

The situation in the 72.5 % urea sample is clearly different. The A'_{zz}-vs.-T plots for all three TEMPO-based spin probes (and also Frémy's salt), differ strongly, either in mid-point temperature or the final low-temperature A'_{zz} (see Fig. 3.6c). For TEMPO the plot (red dotted line with circles) corresponds very well with that of the 50 % urea sample. For TEMPONE (red dotted line with triangles), the immobilization temperature is also very similar to that of the dystectic mixture, but the A'_{zz} values in the frozen state are significantly lower. TEMPOL (red dotted line with squares) in contrast shows high A'_{zz} values as well as higher immobilization temperatures. While the Frémy's salt spectra of the 25 % and 50 % match extremely well, the 72.5 % urea sample matrix causes lower transition temperatures ($\sim$ 45 K) and higher absolute A'_{zz} values (see Appendix Fig. A3).

Comparison of the eutectic and dystectic mixture samples

All four investigated spin probes obviously sense different chemical environments depending on their chemical substitution. This is a clear indication of domain formation on the nanoscale.

Figure 3.8 shows snapshots taken from the MD simulations of the two eutectic and the dystectic mixture (top row). In the bottom row, we have used these snapshots and marked the different regions ([EMIm][Cl]-rich, urea-rich) and especially the interface regions between these two nanoscale regions where Cl^- ions mostly reside. We can use this coarsened view of the [EMIm][Cl] as well as the urea$\cdots$Cl domains to discuss the combined data presented so far. The bridging role of the chloride anion becomes apparent in these snapshots. This explains the formation of nano-segregated domains in the 72.5 % urea sample where there is a chloride deficit whereas the 25 % urea sample shows a homogeneous distribution of urea within the [EMIm][Cl] excess. As has been described before, the role of the Cl^- anions is decisive for the nanostructure in these different mixing ratios.[15] For 25 % urea, the excess of chloride anions leads to a dispersion of individual urea molecules in the majority phase of [EMIm][Cl], hence leading to a homogeneous single phase, as also seen in the EPR data. The 50 % mixture remarkably has the highest melting and the lowest spin probe immobilization temperatures. This indicates that nanoscopic rotational motion of the nitroxide spin probes starts at very low temperatures ($\leq$40 °C), while a melting cannot be observed until almost 90 °C are reached. The snapshot in Fig. 3.8 center (top and bottom) shows a structure of two major phases, one EMIm-based and one urea-based phase, which only partly "share" chloride anions. This situation can be described as a set of two interpenetrating networks that are dominated by their interfaces. Given the high polarity experienced by the spin probes ($A'_{zz} > 3.7$ mT), they probably reside at exactly the interfaces of the two domains where chloride and EMIm ions are abundant. A slipping motion at these interfaces may well start at very low glass transition temperatures (seen in EPR), while a macroscopic melting only occurs when the individual networks break up. Finally, when urea is the majority component, one observes EPR spectra that reflect underlying nanoscopic heterogeneity. As depicted in Fig. 3.8, EMIm molecules form small clusters within a majority "fluid" phase of urea, again both being linked through chloride anions at the interface. This is reflected in the heterogeneity of A'_{zz} vs. T of all three spin probes probing different nanoregions: For TEMPOL, A'_{zz} in the rigid limit at low temperatures rises highest, indicating a polar environment. At the same time, the temperature mid-point (when TEMPOL starts fast rotational motion) at

$-20\,°C$ is significantly higher than for the other two spin probes. These findings can be reconciled when assuming that TEMPOL is hydrogen bonded in the EMIm-based clusters (high polarity, highest rigidity, see also the MSD in Fig. 3.3). TEMPONE and TEMPO, on the other hand, start their reorientational motion at much lower temperatures, hence indicating a weaker interaction pattern and/or a residence in a more mobile surrounding. Interestingly, TEMPONE shows a very low A'_{zz} in the rigid limit while starting reorientational motion at very low temperatures. This respective spin probe therefore must be located in the mobile urea-rich phase with the nitroxide group pointing towards the less polar parts of the EMIm-rich regions that are richer in ethyl groups. A residence in the urea-rich phase can be rationalized when considering the structural similarities between urea and TEMPONE.

The 12.5 and 37.5 % urea samples

Figure 3.7 shows the temperature dependence of A'_{zz} for TEMPO (which is also representative for TEMPOL and TEMPONE, as curves for all three TEMPO-based nitroxides are virtually identical in these two mixtures, see also the Appendix) in the above described samples as well as for four additional samples with other molar ratios. On the basis of the general curve shape and the absolute A'_{zz} values, the 12.5 % and 37.5 % urea samples should be discussed together, and the same holds true for the 62.5 % and the 87.5 % urea samples.

The two eutectic and the dystectic mixture samples 25 %, 72.5 %, and 50 % respectively, clearly show their unusual behavior in the A'_{zz} curves, both in transition temperature and/or absolute values. The curves for the additional samples do not differ strongly from each other with only a slight shift of the transition temperature of the 12.5 % and 87.5 % sample by 10 K. Regarding the plateau values of A'_{zz} at the low temperature end (below $-60\,°C$), a pairwise grouping of 12.5/37.5 % and 62.5/87.5 % is possible, the 12.5/37.5 % samples have $\sim$ 0.2 mT lower A'_{zz} values than the 62.5/87.5 % samples. This again reflects a lower polarity around all nitroxide spin probes for all samples with high [EMIm][Cl] content, as only this IL provides non-polar domains due to the alkyl chains, as discussed above for the dystectic mixture.

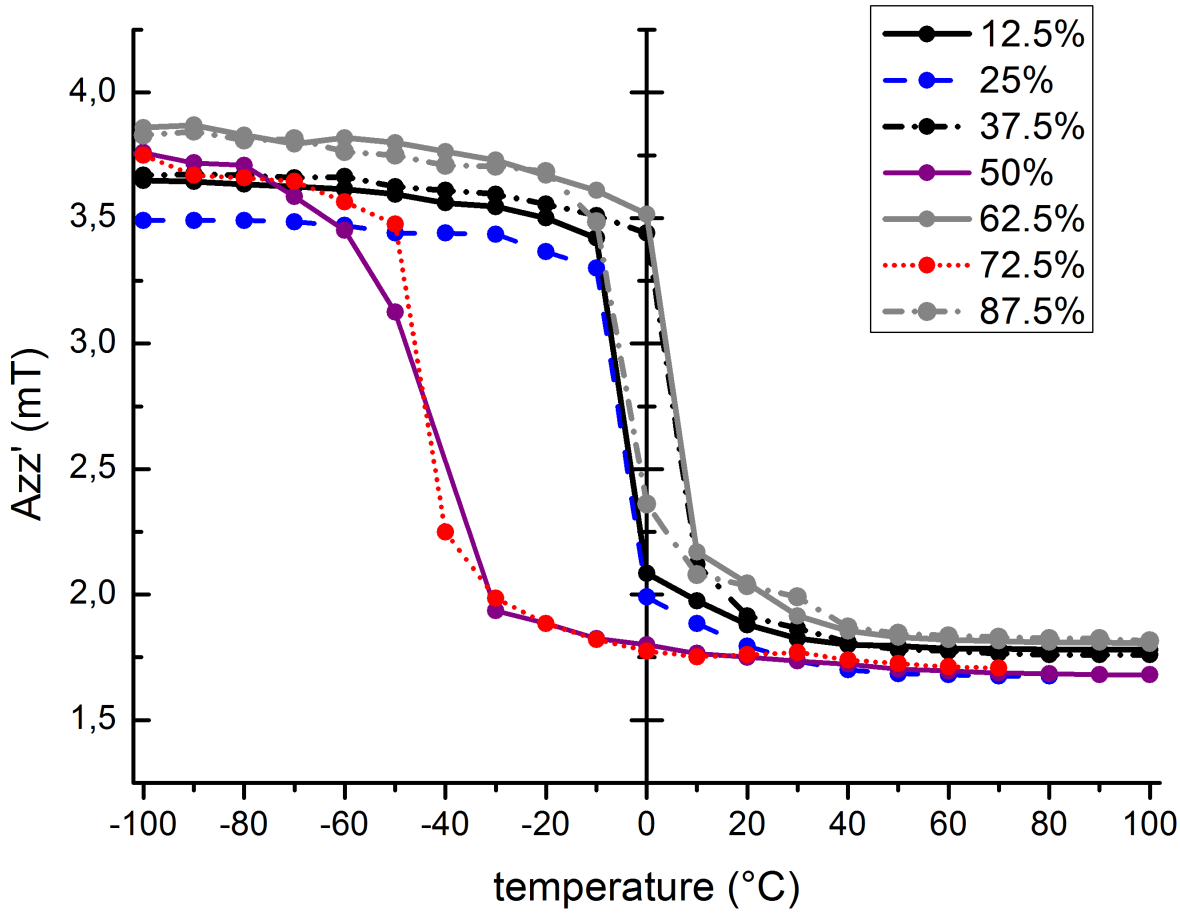

Figure 3.7: A'_{zz} values of TEMPO in all investigated samples in the temperature range between -100 and $+100\,°C$.

The 62.5 and 87.5 % urea samples

The 62.5/87.5 % sample group presents larger low temperature A'_{zz} plateau values because of high urea content, but otherwise does not vary strongly from the 12.5/37.5 % group. At this point it is instructive to look at the individual CW EPR spectra in more detail. The TEMPOL spectrum at 30 °C clearly shows two spectral species are present (see Appendix Fig. A4). This finding is in good agreement with the structural assumption given above for the dystectic mixture in the 50 % sample. The formation of interpenetrating domains sets in

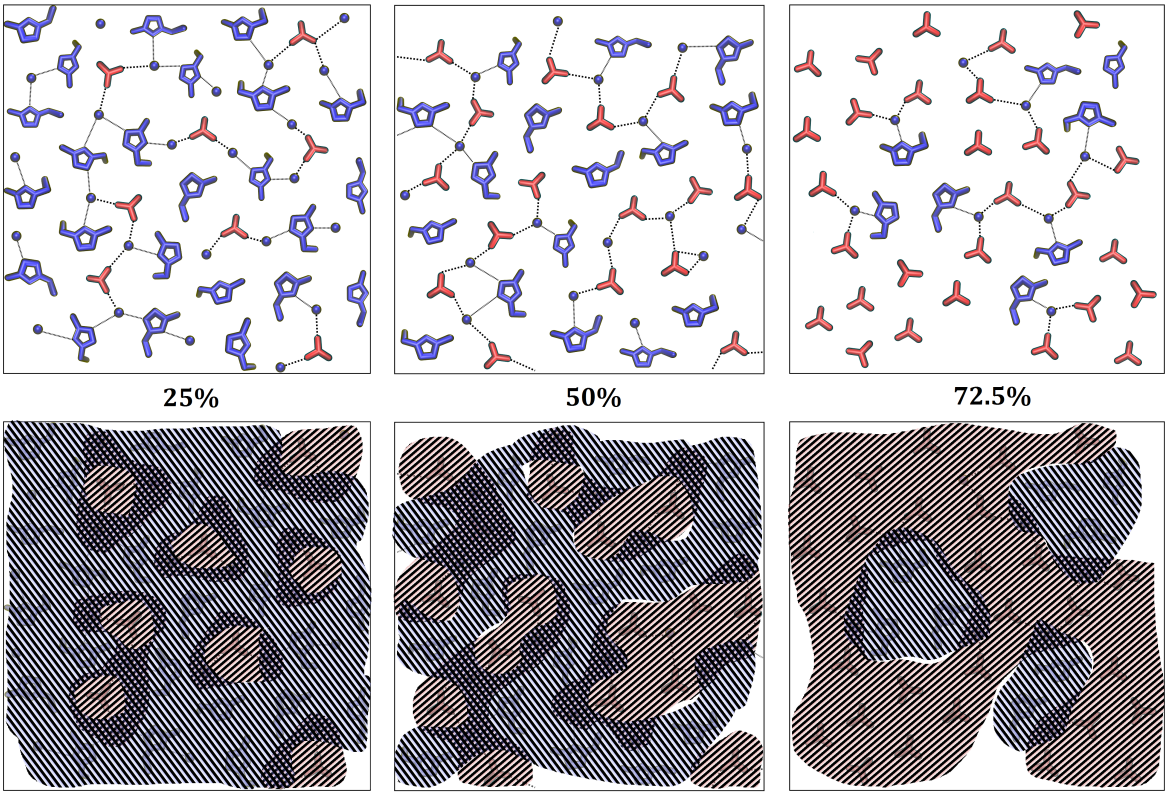

Figure 3.8: Schematic representation of the structural ordering as well as [EMIm][Cl]- and urea$\cdots$Cl-regions of the two eutectic samples and the dystectic sample. Top row: detailed assumption on the molecular orientation on the nanoscale of all three important mixtures: 25 %, 50 % and 72.5 % urea. Thereby, the IL [EMIm][Cl] is shown in blue and urea is shown in red. For the bottom row, the single components were shaded with stripes, top left to bottom right, blue, for the [EMIm][Cl]-domains and bottom left to top right, red, for the urea$\cdots$Cl regions.

and since TEMPOL can in principle reside in both, [EMIm]- and urea-rich nanoregions, this can explain more than one TEMPOL species in the spectrum.

Interestingly, all four samples 12.5 %, 37.5 %, 62.5 % and 87.5 % urea have transition temperatures which are significantly higher than the 50 % and 72.5 % urea samples, although the

macroscopic melting point is lower for the 72.5 % urea sample and higher for the 50 % urea sample. The high transition temperature is caused by an immobilization of the free rotation due to hydrogen bonding between the spin probes and the sample. It seems that all strong hydrogen bond acceptors – the chloride anions – are occupied in the 50 % and 72.5 % urea sample which leaves the spin probes more mobile. Only the 25 % urea sample has an excess of free chloride anions, which explains its high transition temperature that corresponds with those of the 12.5 %, 37.5 %, 62.5 %, and 87.5 % urea samples.

3.4 Conclusions

In this study we prepared mixtures of a non-room-temperature IL [EMIm][Cl] and urea and investigated the full range of molecular ratios with a particular focus on the three melting point extrema: two eutectic molar ratio samples with local melting point minima and a dystectic molar ratio sample with a local melting point maximum. We are specifically interested in understanding the difference in nanoscopic structures and dynamic interaction patterns and how they correlate with the macroscopic properties. The DSC and EPR results show, that the 1 : 1 mixing ratio, *i.e.* the dystectic mixing ratio, features an interpenetrating network of nano-segregated domains of the organic salt and urea, respectively. This sample of two co-continuous phases, as seen from EPR spin probe molecules' point of view, behaves like a conventional molecular solvent. Hence, it is not the mixing process *per se* that causes ionic liquid-like properties. However, it could be shown that the anion is the central component in the formation of the hydrogen bonding network. An excess/lack of the anion dominates the extent of intermolecular interaction and therefore the melting behavior. The A'_{zz} values that were obtained by EPR spectroscopy give access to the rotational immobilization of the spin probes which is most strongly influenced by hydrogen bonding and also by freezing of the surrounding matrix. For the non-extremal points in the mixtures that have relatively high transition temperatures, *i.e.* the 12.5 %, 37.5 %, 62.5 % and 87.5 % urea samples, apparently hydrogen bonding of the spin probes is easily possible. We can further conclude that all chloride anions are occupied in the 50 % and 72.5 % samples with hydrogen bonds

which might be the reason for their melting point extrema. Interestingly, these two mixtures have the largest difference macroscopically (melting point difference of almost 30 K), yet the spin probes experience similar rotational mobilities. The 1 : 1 molar mixing ratio in the 50 % sample presumably is ideal for an extensive and strong hydrogen bonding network with a saturation of all available interaction sites and the chloride anion playing the central role by bridging the urea with the $[EMIm]^+$ cation. It is the such formed interpenetrating, nanoscopically segregated network of IL-rich and urea-rich regions that leads to the melting of the sample when the higher melting component starts to melt. The 72.5 % urea mixture with its lack of anions shows a high degree of domain formation which is similar to what has been discovered in ionic liquids numerous times before.[45,46,47,48] The weakening of the IL's Coulomb attractions due to hydrogen bonding with the HBA urea leads to a pseudo-fluid $[EMIm]^+$ cation phase in the 25 % mixture and the EPR spectroscopic data can be substantiated by means of PFG NMR spectroscopy and MD simulation. This study gives an in-depth view on the nanostructure and the prevailing interaction patterns of probe molecules in deep eutectic solvents. We could show that for ionic liquid-like properties the key parameter to control is the very sensitive balance of weak intermolecular bonding. Melting point depression can finally be controlled by preparing mixtures in which the number of anions deviates from the molar ratio that lead to stable interpenetrating nanostructures.

4 The deep-eutectic choline chloride/imidazole–water mixture – a "porous" liquid

4.1 Introduction

The possibility for ionic liquids to serve as an alternative for common organic solvents has been evaluated for some time now – because of their similar properties, the same consideration can be drawn for deep-eutectic solvents as well. The aim of this study was to investigate the deep-eutectic mixture of choline chloride and imidazole at a molar ratio of 3 : 7 (see Fig. 4.1**(1)** and **(2)**) with a melting point minimum of 58 °C[39].

Since ChCl-based DES mixtures are highy hygroscopic,[49] and water cannot be fully excluded in possible fields of application of this DES, the initial question here was how water influences the physicochemical properties of the mixture. Different physicochemical measurements were performed, such as rheological, density, refractive index, pH, and conductivity measurements. Additionally, high temperature liquid NMR and solid state magic angle spinning (ss MAS) NMR as well as electron paramagnetic resonance spectroscopy were used to obtain further insight on the nanostructure of this mixture.

Similar to chap. 3 the EPR spectroscopy was employed to investigate the nanophase composition as well as microviscosity and -polarity by means of introducing persistent radicals into the mixture, here TEMPO and Frémy's salt (Fig. 4.1**(3)** and **(4)**).

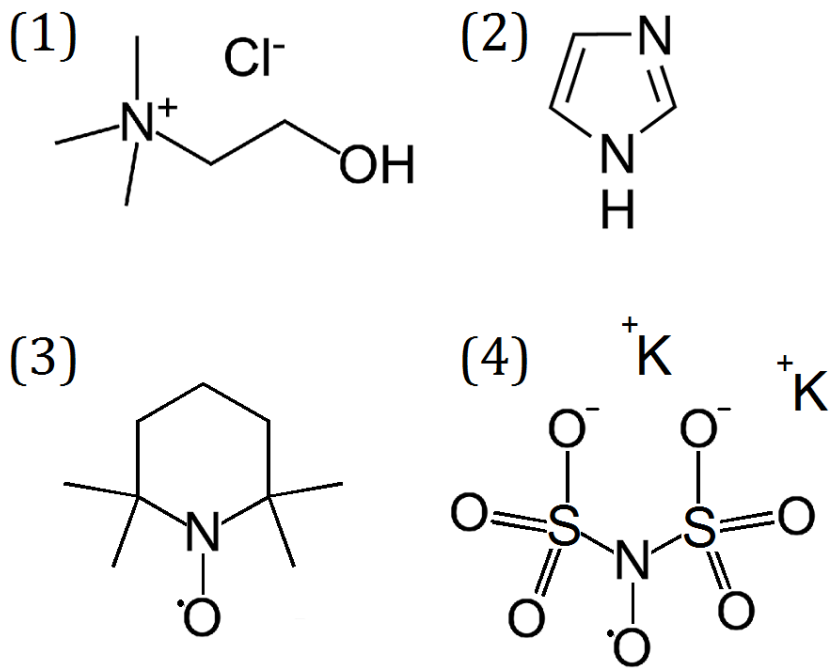

Figure 4.1: Structures of the used components: **(1)** choline chloride, **(2)** imidazole, **(3)** TEMPO, **(4)** Frémy's salt.

4.2 Experimental

4.2.1 Sample preparation

Choline chloride hast been purchased from Alfa Aesar with a purity of 98 %, imidazole has been purchased from Sigma Aldrich with 99.9 % purity, both were used as received after a treatment unter vaccuum at 80 °C for at least 10 h. The eutectic point for the mixture has been reported to be choline chloride : imidazole 3 : 7[39] which was subsequently prepared in that manner (see Fig. 4.2). The mixture has been heated to $\sim$ 100 °C to reduce the initial water content.

Different batches with the 3 : 7 molar mixing ratio were prepared and mixed with different amounts of water, mainly at low molar contents to mimic the water impurities that can occur: 0, 1, 2, 4.5, 9, 13, 20, 33.5, 43, and 100 $\%_n$, respectively.

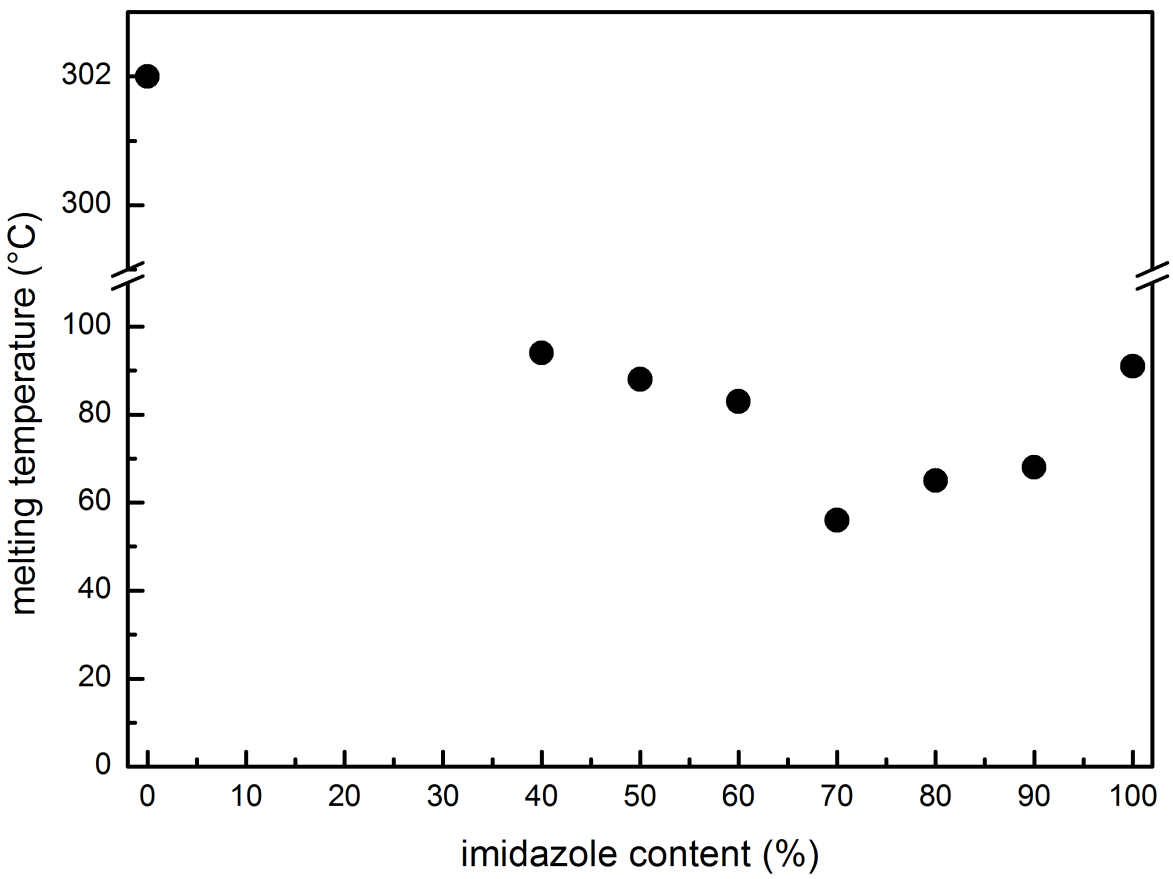

Figure 4.2: Melting diagram of different imidazole-based mixtures, taken from Hou et al.[39]

4.2.2 Rheology and density measurements

Viscosity data was aquired with a Physica MCR 301 rheometer from Anton Paar with a CP 25-2/TG spindel at 65 °C. The densities were obtained through gravimetrical measurement of 100 µl volumes on a precision balance.

4.2.3 Water uptake

Water uptake rates were measured on a precision balance of 0.01 mg in a box of constant local humidity of $\sim$ 60 %. A volume of 1 ml was placed on the scale and the weight increase was monitored every 15 s for 30 min.

4.2.4 NMR studies

For spectroscopic data, a Bruker NMR spectrometer has been used at 400 MHz and 60 °C with D_2O as solvent. Furthermore, MAS solid state NMR has been performed at a 400 MHz Bruker Avance system with two different repetition times: 3 s (3000 scans accumulated) and 240 s (268 scans accumulated). Previous to the preparation of the MAS ssNMR rotor (Bruker 2 mm MAS probe rotor), the sample was dried under vacuum for > 12 h and pestled into a very fine powder inside a glovebox and carefully and evenly tamped into the rotor.

4.2.5 Electron paramagnetic resonance

For electron paramagnetic resonance data, either TEMPO or Frémy's salt was added ($\sim 1\,\mathrm{mg\,ml^{-1}}$) to the mixture and examined in a MiniScope 400 by magnettech in the same way as already described in Sect. 3.2.3. A temperature range from -100 °C to $+60$ °C was measured.

4.3 Results and discussion

4.3.1 Physicochemical properties

The density is a property that depicts the molecular packaging and therefore can give coarse information on the interactions on molecular level upon adding water. All prepared samples were heated to 65 °C and then a volume of 100 µl was weighted on a scale and repeated 5 times. Figure 4.3 shows the averaged densities for all samples.

An ideal mixture should show values that follow Raoult's law, i.e. a linear behavior between the values of the pure 3 : 7 mixture and pure water. This is commonly not the case as positive/negative value excesses can be observed for many mixtures. Interestingly, the density measurements show values that even exceed the pure mixtures density. The added water does not contribute to an adequately increased sample volume. Reason therefore could be that the water molecules occupy empty molecular voids in the ChCl–Im structure.

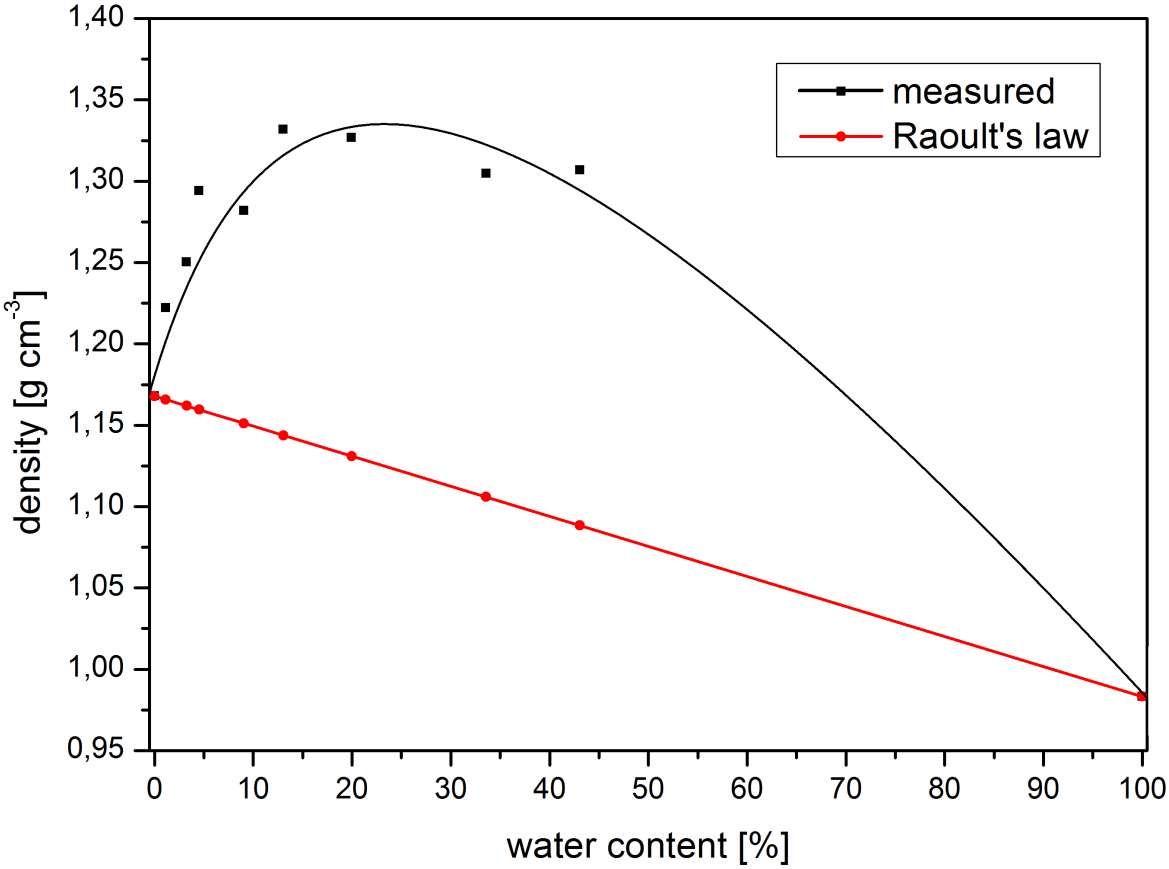

Figure 4.3: Density of the choline chloride–imidazole-mixture with different water contents. The black line denotes a linear dependence which would be the case in an ideal mixture. The red line shows the actual trend.

The other investigated physicochemical properties show a non-ideal behavior as well (see Fig. 4.4). Thereby small water contents have a strong effect on the mixture's viscosity, but not on the pH or refractive index. Water seems to have a heavy impact on the molecular structure and hence its viscous flow. However, there must be a second factor that leaves some properties less affected by water, such as the pH, the refractive index or the conductivity.

Since most ionic liquids and also choline chloride are highly hygroscopic, the water uptake of the ChCl–Im mixture was investigated by simply placing the sample on a balance and

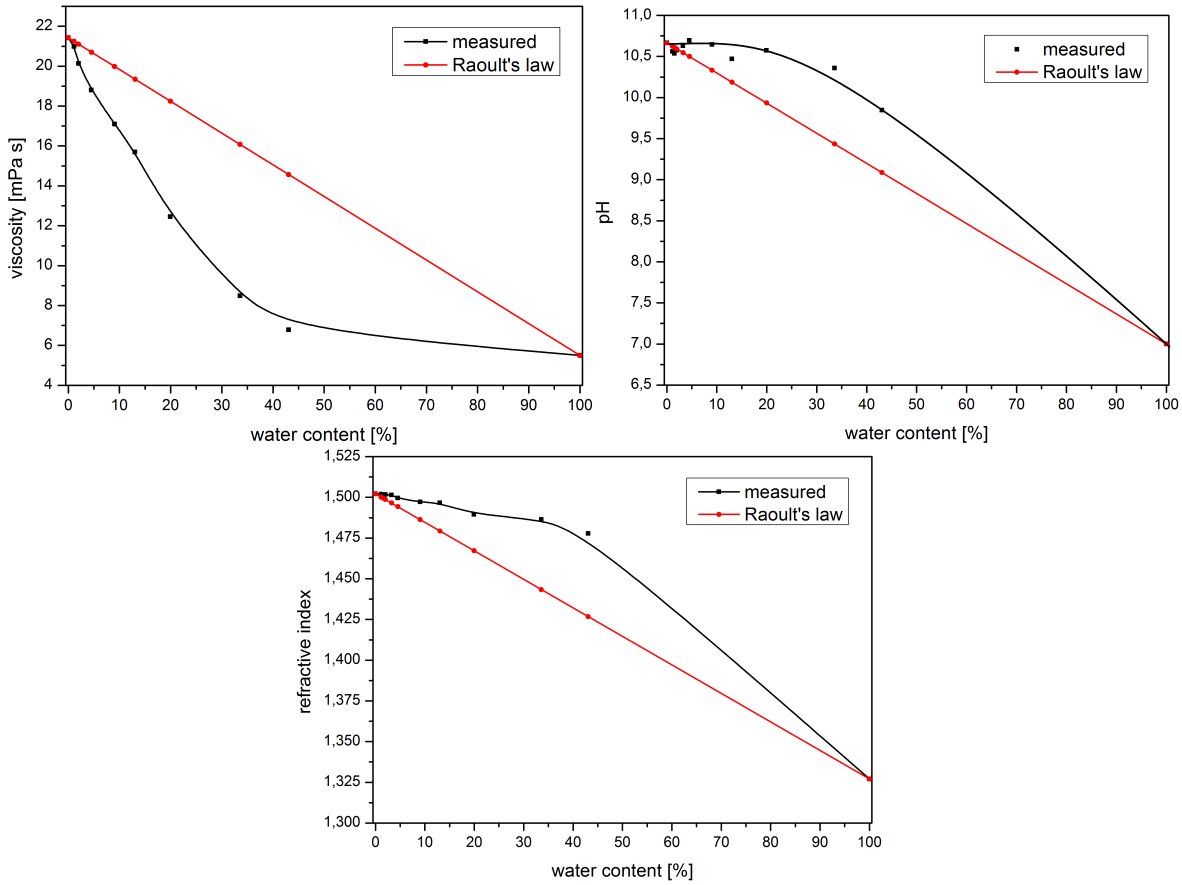

Figure 4.4: Selected physicochemical properties of the choline chloride–imidazole-mixture with different water contents. The black line denotes a linear dependence which would be the case in an ideal mixture. The red line shows the actual trend: **(a)** viscosity, **(b)** pH value, **(c)** refractive index.

monitoring the mass increase due to binding the water from the local air moisture. A defined volume of 1 ml in a glass vial was placed on the scale and the weight was observed every 15 s. As can be seen in Fig. 4.5 the water weight gain shows a very interesting pattern for all samples. Since the samples were all transferred onto the balance in their liquid state, they first had to cool down to room temperature hence showing re-crystallization. This cool-down process shows an initial decrease in mass (Fig. 4.5I), followed by a negative exponential increase (Fig. 4.5II) which merges into a linear increase (Fig. 4.5III).

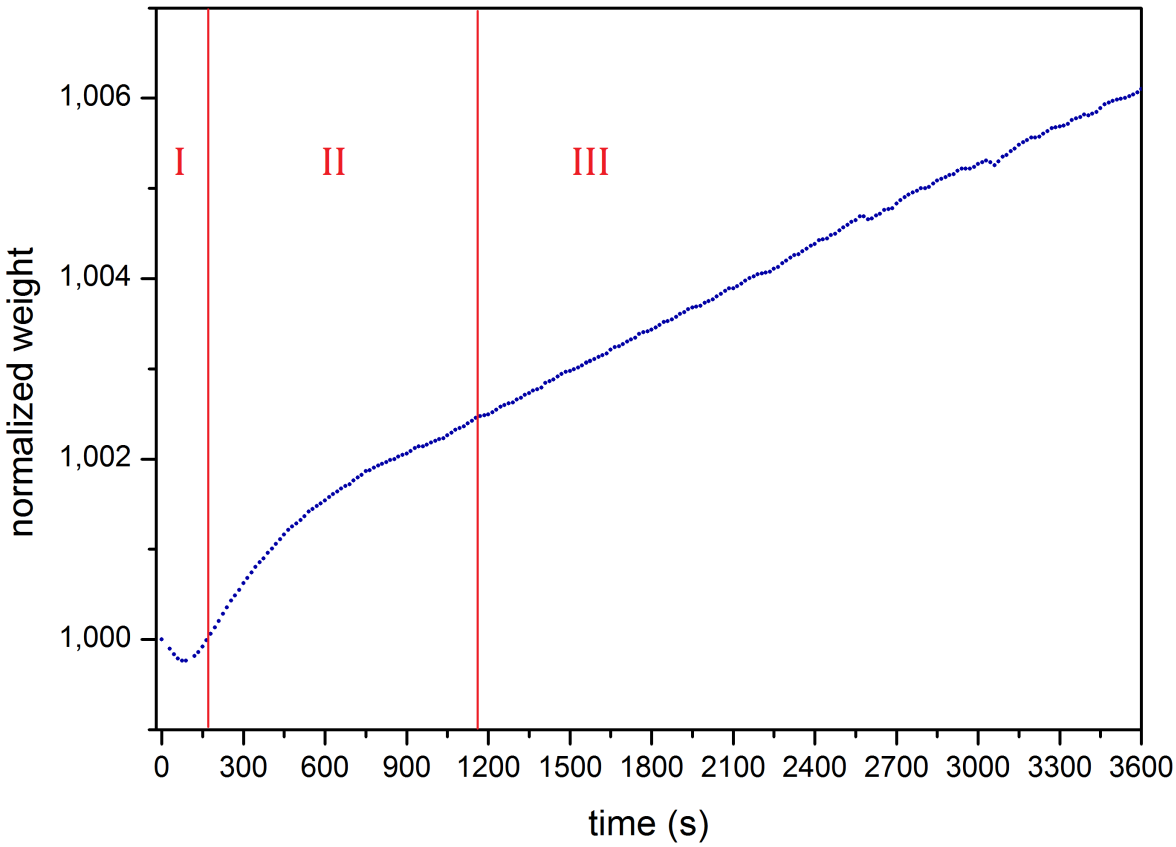

Figure 4.5: Pattern of mass increase in the water uptake experiment.

I. The most obvious explanation for the initial mass loss is a possible displacement of water upon recrystallization. However, the mass loss behavior is present even for the sample without any added water. But since the mixture is highly hygroscopic, a completely water-free sample cannot be guaranteed once it is exposed to the air for a few minutes which might be the reason.

II. The deminishing increase lets assume that a concentration-dependent process is involved, which could be initial fast surface adsorption. The step **II**-type increase is fitted on the basis of a TEMKIN adsorption isotherm[50]. The TEMKIN approach is based on a decrease of adsorption heat due to adsorbent–adsorbent-interaction. Since the samples were transferred

on the balance at a temperature of $\sim$ 60 °C, the measurement started while a cooling process took place, which mimics the fundamental thought of the TEMKIN adsorption theory.

$$q_e = \frac{RT}{b_T} \cdot \ln\left(A_T \cdot C_e\right) \tag{4.1}$$

$$q_e = \frac{RT}{b_T} \cdot \ln A_T + \left(\frac{RT}{b_T}\right) \cdot \ln C_e \tag{4.2}$$

$$y = a + b \cdot \ln\left(x + c\right) \tag{4.3}$$

The TEMKIN isotherm constants a and c cannot be compared since they depend on initial sample mass as well as starting time of the measurement and recrystallization. The parameter b represents the steepness of the mass increase and is used to evaluate the speed of water uptake. Table 4.1 summarizes the initial mass loss as well as the logarithmic fitting parameters according to Eq. 4.3 and the linear slope.

Table 4.1: Fitting parameters for all ChCl–Im samples, logarithmic fitting (type **II**) as well as linear fitting (type **III**) parameters are shown.

sample no.	water content	a	b $\cdot -10^3$	c $\cdot 10^{-2}$	R^2	k $\cdot 10^{-6}$	R^2
1	0 %	0.83	**1.18**	0.83	0.999	1.18	0.999
2	1.1 %	0.97	**1.57**	0.97	0.999	1.49	0.998
3	2.0 %	1.29	**1.60**	1.02	0.999	1.14	0.997
4	4.5 %	1.28	**1.76**	2.14	0.998	0.75	0.986
5	9.1 %	1.56	**1.61**	3.45	0.999	0.79	0.996
6	13.1 %	1.28	**1.18**	3.39	0.999	0.79	0.998
7	20.0 %	1.29	**0.75**	1.27	0.998	0.71	0.995
8	33.6 %	1.31	**0.68**	2.84	0.997	0.56	0.993
9	43.1 %	1.31	**0.84**	1.04	0.998	1.05	0.993

Figure 4.6 shows this fitting parameter b dependent on the initial water content in the sample. It can be seen that the speed of water uptake increases until $\sim$ 5 % of initial water content and then decreases again until a plateau is reached. From Fig. 4.6 it can be assumed that small water contents in the sample facilitate the water adsorption. The underlying effect for a fast surface adsorption could be a higher number of adsorption sites *e.g.* because of a fast absorption of surface-bound water molecules into the bulk, unblocking their adsorption sites. At water contents of $\sim$ 10 %, the adsorption speed decreases until it reaches a plateau starting from $\sim$ 20 % water content. It seems that only the small water content samples up to 10 % show increased uptake speeds.

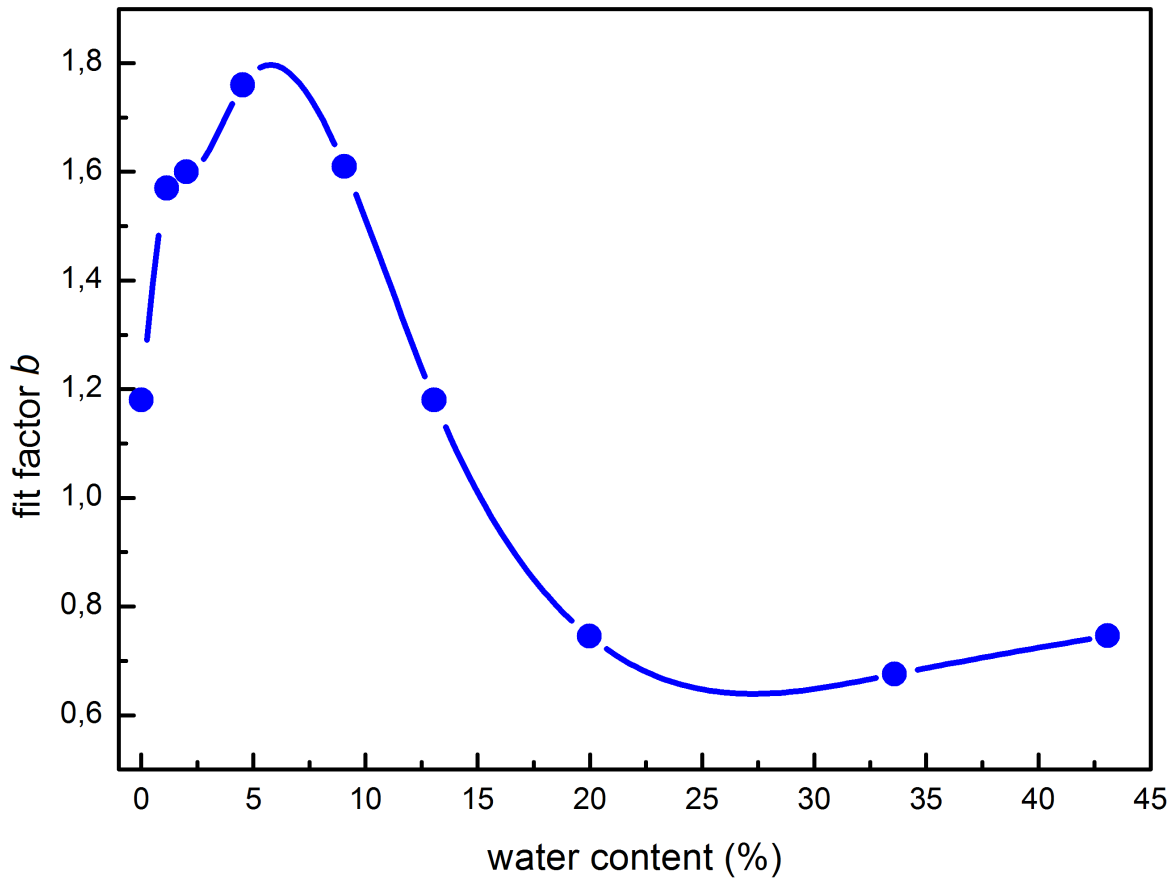

Figure 4.6: Logarithmic fitting parameter b representing the type **II** speed of water uptake for samples with different initial water content.

III. After a time of $\sim$ 10 minutes the mass increase follows a linear rate for every sample. If the type **II** increase really is governed by surface adsorption, the absorption into the bulk is a process that takes place simultaneously until the absorption rate is at equilibrium with the adsorption rate (type **III**).

A long-term experiment revealed that this linear mass increase will not stop until the water content in the sample reaches approx. 60 % (*cf.* Appendix Fig. A6). It can be assumed that at this water content, the sample molecules are fully solvated. A similar experiment has been performed by Meng et al. who studied a mixture of choline chloride and urea[51].

4.3.2 Spectroscopic analyses

EPR spectroscopy

As stated in Section 3.3.3, EPR spectroscopy is a powerful tool to unravel underlying micro-heterogeneity in a sample structure. For the mixture of imidazole and choline chloride, the spin probes Frémy's salt and TEMPO have been chosen in order to show a different interaction and enrichment if two or more nanophases are present. The idea was that the double negatively charged Frémy's salt interacts the most with the choline cation whereas TEMPO will be pushed into a more non-polar regime, if existent. This would lead to different immobilization temperatures between both spin probes and different polarities of both spin probe's environments as seen in the hyperfine coupling, *i.e.* the A'_{zz} value.

In Fig. 4.7 the A'_{zz} value of Frémy's salt in the choline chloride–imidazole mixture for different temperatures and small water contents is shown.
At temperatures between +10 and −10 °C, the A'_{zz} value seems to increase at first upon cooling down the sample but then drops back to the baseline, hence indicating two distinct components. Noteworthy hereby is, that all ChCl–Im samples have the same baseline and curve progression belov −10 °C regardless of their water content. Additionally, the anomaly peak also exists in the sample without any water. However, with increasing water content this anomaly peak shifts to lower temperatures and becomes more prominent. It thus can be

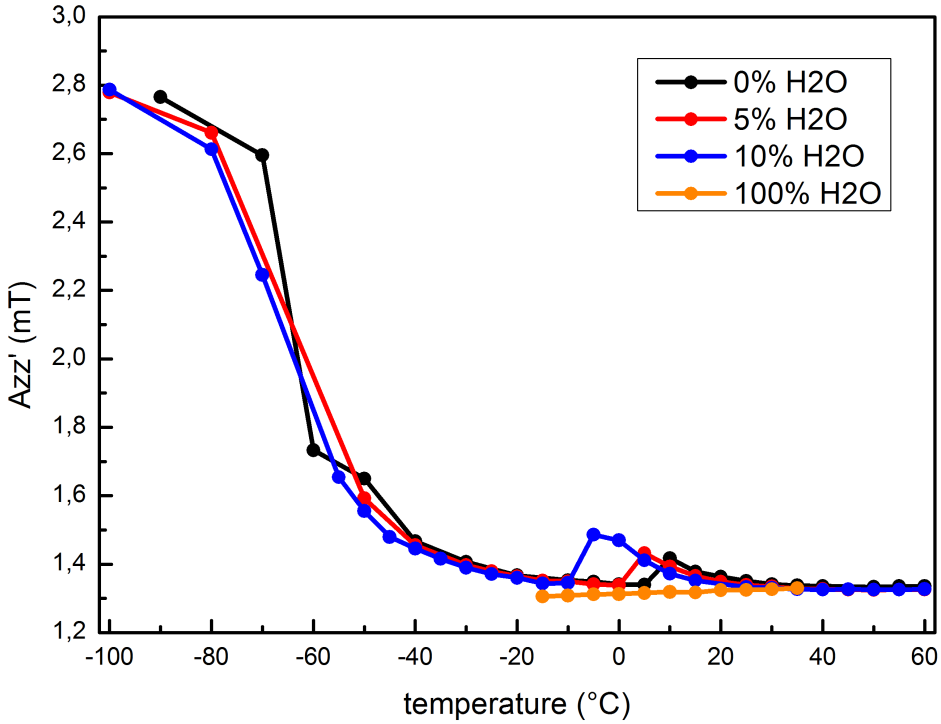

Figure 4.7: A'_{zz} values of Frémy's salt in samples with small water contents in the temperature range between -100 and $+60\,°C$.

assumed that two different Frémy's salt species exist because there are two different phases in the sample with which the added spin probe can interact. These phases already exist even if no water is added, which can be seen in Fig. 4.7 at the 0 % curve.

In order to further investigate the 0 % water and the possible existence of structural heterogeneity, the more hydrophobic spin probe TEMPO was used. Figure 4.8 shows selected spectra of this sample. With decreasing temperature, spin exchange interaction becomes apparent through the disappearance of the three distinct peaks merging into one. With increasing water content the exchange interaction becomes less present although the existence of two (or more) spin species is visible. Especially the sample with 10 % water content shows the change of intensity of two different components at the low-field peak (see Fig. 4.9).

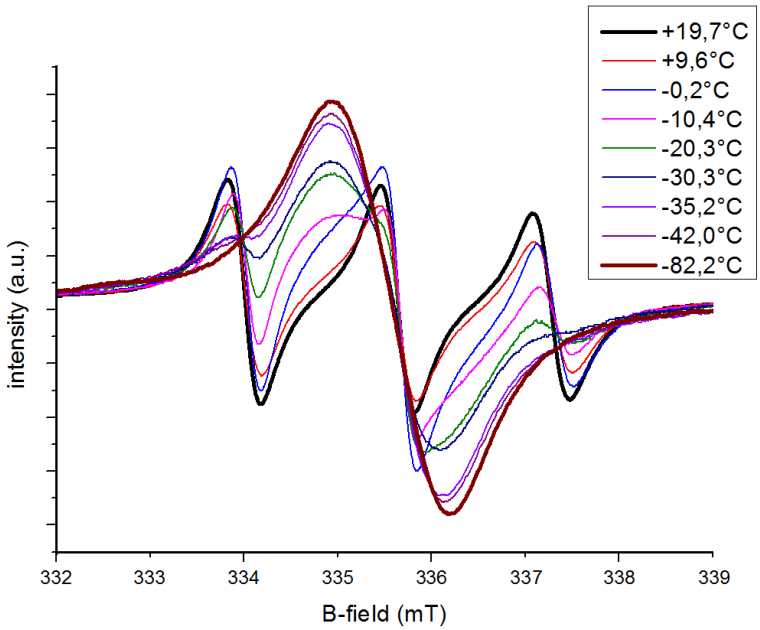

Figure 4.8: Selected spectra of TEMPO in the 0 % water sample. The thick black line denotes the highest measured temperature, the thick redk line the lowest temperature.

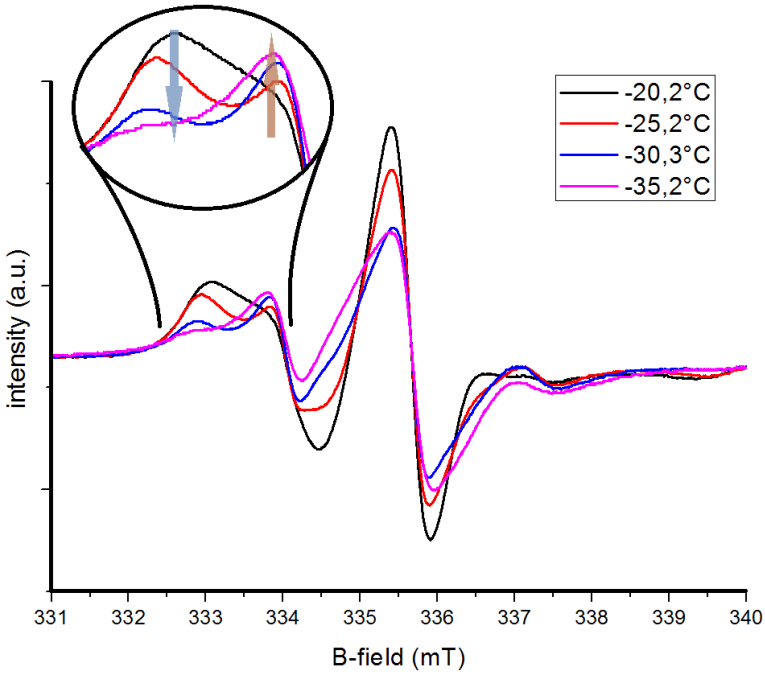

Figure 4.9: Selected spectra of TEMPO in the 10 % water sample, focus on low-field peak.

Solid state NMR spectroscopy

In order to help gain further insight on the existence of different domains and their size, solid state NMR was performed for the choline chloride–imdazole mixture without water content. By means of NMR spectroscopy, the different components of the mixture can be tracked individually. Figure 4.10 shows the ssNMR spectra of the mixture with two different repetition times (3 s in Fig. 4.10a vs. 240 s in Fig. 4.10b). Considering that the peak at $\sim$ 52 ppm, originating from the choline cation, has the similar intensity in both measurements, the peak intensity for the three imidazole peaks vary extremely with a change in repetition times. It thus becomes very apparent, that the T_1 relaxation times of both molecules must be very different.

Very different relaxation times give a hint for a high spatial separation of both molecules, otherwise the relaxation times would average each other out. However, a spatial separation is expected in solid eutectic mixtures and EPR spectroscopy indicates formation of different domains as well. Interestingly, the line width of the choline methyl group at $\sim$ 52 ppm is so large that it includes the resonance of the neighboring CH_2-group. Broad lines in ssNMR indicate a high molecular dynamic. This seems to be the case for the choline-rich phase, whereas the imidazole resonances do not show a high line broadening, which indicates a lower molecular dynamic of the imidazole-rich phase. These results are contrary to the findings of Chap. 3 where the excess component was the more mobile due to a lack of H-bonding partners. Here, the choline-rich phase seems to be more mobile although imidazole is added in excess. Since the chloride anion probably acts as bridging partner between choline- and imidazole-rich phase, it leaves the choline-rich phase in its bulk depleted with negative charges. Consequently, Coulomb repulsion between choline cations might create voids and leaves the cations more free space to move. This mobility effect gets enhanced upon addition of water which lowers the microviscosity.

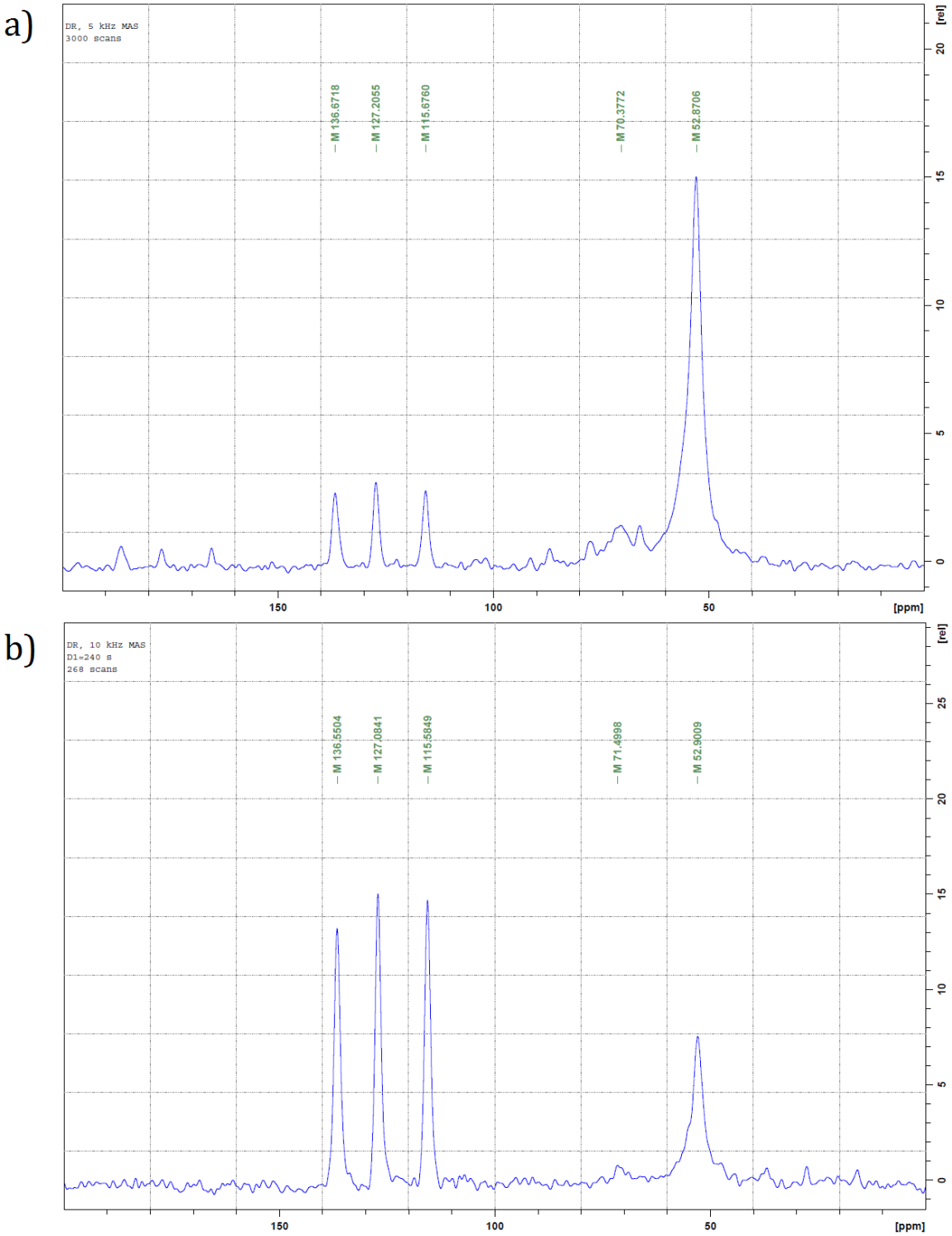

Figure 4.10: Solid state MAS NMR spectra for two different repetition times.

In contrast to solid state NMR, liquid state NMR reveals that imidazole shows one less resonance peak in its liquid state (see Fig. 4.11). In solution, the proton bound to one of the nitrogen atoms of the imidazole ring undergoes fast exchange, which makes both of the CH_2–CH_2 carbons chemically equivalent. In its solid state, both carbon atoms can be distinguished. Due to strong ppm shifts for samples with higher water content, one of the imidazole peaks has been marked as reference and the deviations to the other peaks were calculated to generate the plot in Fig. 4.11a. There, the chemical shift change for every signal with increasing water content is shown. What is very obvious is that the hydroxy-group hydrogen atom is highly influenced by increased water content. All other peaks only show a slight upfield shift. At a closer look it can be seen that the peak **(6)** features a very strong upfield shift, whereas esp. peaks **(2)** and **(3)** stay rather unaffected. The first peak belongs to the trimethylammonium-group (see Fig. 4.11b). Thus, it can be assumed that the choline-rich phase is stronger affected by increasing water content. A detailed view of all NMR spectra can be found in the Appendix.

Explanation of the physicochemical properties with spectroscopic findings

In order to gain insight on what happens to the eutectic mixture structure upon adding water, physicochemical measurements as well as spectroscopic experiments were performed. Thereby, the density measurements give very important information. Upon adding water, the density of the mixture increases although the density of pure water is lower than the density of the pure choline chloride–imidazole mixture. This means that the water is built into the mixtures structure without increasing the volume, *i.e.* into molecular voids. Figure 4.3 lets assume that the mixture easily takes up to 20–25 % of water. Water uptake measurements give another hint on how the uptake process could take place. When the samples were placed on the scale in their liquid state at $\sim$ 60 °C, the mass decreased upon recrystallizing under room temperature before the mass increase through water uptake started. Since this effect happened for the sample without any added water, a possible reason for the initial mass decrease is the displacement of air molecules out of the sample leaving behind molecular voids.

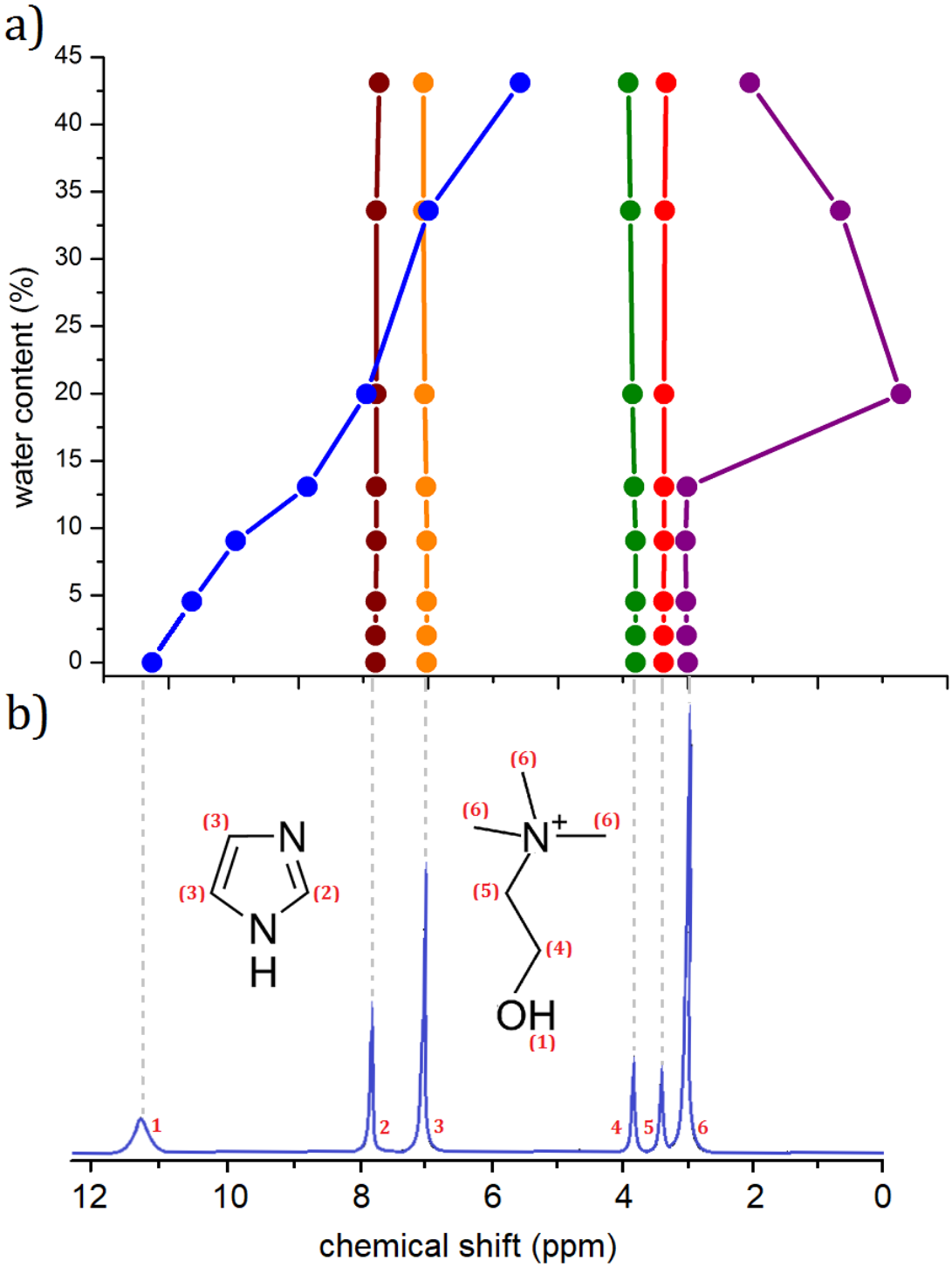

Figure 4.11: **(a)** Liquid state NMR chemical shift change with increasing water content; **(b)** reference spectrum of the sample with 0 % water content.

Electron paramagnetic spectroscopy showed two distinct spin probe species in the choline chloride–imidazole-mixture, with as well as without water. When transferring the single spectra into the A'_{zz} view, it becomes apparent that the minor spin component creates a small peak at temperatures around 5 °C ±10 °C. The minor spin component seems to be incorporated in a phase with very high immobilization temperature, since the transition from fast movements (*i.e.* low A'_{zz} values) to slow tumbling/immobilization (*i.e.* high A'_{zz} values) takes place $\sim$ 45 °C higher than for the major component where the median immobilization temperature is at −60 °C. Frémy's salt is a double negatively charged radical anion, although it could form hydrogen bonds with the imidazole, the Frémy's salt should accumulate rather in the choline phase due to the possibility to undergo COULOMB interactions with the choline cations. Thus, it is likely that Frémy's salt in the imidazole-rich phase presumably represents the minor component whereas Frémy's salt in the choline-rich phase can be assumed to be the main component. That being stated, the minor spin component shows a very early immobilization upon cooling which lets suggest that the imidazole-rich phase is very rigid, whereas the choline-rich phase has a higher molecular dynamic. The minor component peak in Fig. 4.7 of the EPR measurements does indeed change with added water. However, the shift to lower temperatures and the slightly increased intensity can easily be explained with the higher overall fluidity of the sample and with the dilution of the positively charged choline-rich phase due to the added water. Also the more hydrophobic spin-probe TEMPO suggests that heterogeneity on the nanoscale is existent. For the sample without any water, the TEMPO molecules are assumed to be restricted to the rigid imidazole-rich phase. And indeed, rotational hinderance at room temperature is visible (see Fig. 4.8) until broad spin exchange takes place at very low temperatures. Spin exchange at the used concentrations as low as 1 mg per ml of sample can only be explained by agglomeration of TEMPO molecules. Therefore it is unlikely that the TEMPO molecules are present in the choline-rich phase where there are voids for the spin probe molecules to freely rotate. Thus, it is expected for the spectra of TEMPO in samples with added water that a separation into two spin species will not take place in the extent that could be seen for Frémy's salt. Only the 10 % water sample showed a slight rise of a second spin species at the low-field peak (*cf.* Fig. 4.9).

Solid state NMR showed extremely different relaxation times between the imidazole signals and the choline signals. Reason for this is relatively high spatial distance between both phases. A high line broadening of the choline signals gives another evidence that the choline-rich phase is very dynamic compared to the imidazole-rich phase. However, EPR and solid state NMR did not prove to be suitable methods to explain what happens when water is added to the mixture. Therefore, NMR experiments in the liquid state were performed. In order to achieve the liquid state while ensuring comparability with the 0 % water reference sample, the measurements were done at 60 °C. As can be seen in the change of chemical shifts, the choline signals were affected the most upon addition of water. Hence, it can be assumed that the water is incorporated in the choline-rich phase rather than in the imidazole-rich phase, which makes the choline-rich phase even more fluid. Choline chloride *per se* is quite hygroscopic, it would only be logical that water mixes with the choline-rich phase. Due to the large cation size compared to common salts, the choline–chloride lattice is relatively loose, which manifests also in its low melting point of only 302 °C. This loose lattice gives the possibility to incorporate molecular voids, where the water molecules can be built in without increasing the overall volume. A previous study also showed that the Coulomb interactions between the ions of a salt is decreased when a hydrogen bond donor is added, since the HBD forms hydrogen bonds with the salt's anion [1]. If now a part of the chloride anions is accumulated to the choline chloride–imidazole interface, it leaves the local choline chloride bulk depleted with chloride anions. Hence Coulomb repulsion between choline cations is enforced which may be another source for voids in the choline-rich phase where water can be absorbed into. This would explain the massive increase of density when the actual less dense water is added. The water uptake measurements showed higher steepness of the logarithmic mass increase for the samples with low water content until $\sim$ 10 %. Most likely, this is the amount of water that can be easily accommodated in the accessible molecular voids. At higher water contents, the voids get rarer, the uptake speeds will decrease and the volume of the sample will increase.

The spectroscopic data let suggest that the choline chloride–imidazole-mixture exhibits distinct nanophase segregation and separation. Thereby, the imidazole phase seems to be very rigid and unaffected by water whereas the choline phase is highly dynamic and susceptible to water incorporation. This duality might be the underlying reason for the extremely different influence small water contents have on selected physicochemical properties. Density and viscosity undergo a strong change when water is added (see Fig. 4.4), the reason is originated in the choline-rich phase getting affected by water easily. The water heavily increases the local fluidity which then dominates the overall viscosity. Every property that is dependent on molecular movement should show the same results. In contrast, there are properties that do not change strongly when water is added, *e.g.* refractive index or pH value. The rigid imidazole lattice seems to shield the additional water for making an impact on the refractive index. When comparing the pH measurements with a pure high-concentrated imidazole solution (see Appendix Fig. A7), it can be seen that even though the pH of the mixture does not change linearly when adding water, it shows stronger changes to lower pH values than the pure imidazole solution. Imidazole can be protonated very well which leaves a OH^- group behind, thus leading to very high pH values. In the mixture with choline chloride however, it seems like a part of the imidazole is not reached by the water to undergo full protonization. This again supports the assumption of water incorporation mostly in the choline-rich phase while the imidazole lattice stays intact.

4.4 Conclusions

The deep-eutectic solvent mixture choline chloride–imidazole was investigated regarding the influence small water contents have on its physicochemical properties. Since water is the most prevailing impurity when handling substances under ambient air humidity (*e.g.* in laboratories or technical facilities of the chemical industry), knowledge about the impact of the water is the key in finding the right application and/or necessary conditions. The investigated sample was a 3 : 7 mixture of choline chloride and imidazole. At this specific mixing ratio, the mixture features a eutectic point with a melting point of $\sim$ 56 °C, which makes it possibly

applicable under mild conditions in chemical industry. Water uptake measurements showed that the mixture is indeed very hygroscopic and extracts water from the air humidity very fast until the water content in the sample equals the air humidity. Hence it is reasonable to unravel the influence of water on basic physicochemical properties. An extensive analysis with electron paramagnetic resonance as well as solid state nuclear magnetic resonance spectroscopy gave a well-founded view on the sample's structure on the nanoscale. Both methods showed that a nanophase segregation between choline chloride and imidazole exists. Thereby, the choline-rich phase exhibits a high molecular dynamic whereas the imidazole-rich phase is very rigid and may act as a lattice. It is assumed that the existing duality of rigid solid imidazole lattice and fluid solid choline phase is the reason for the different impact that water has on different physicochemical properties. Additionally, a previous study showed that upon addition of a hydrogen bond donor to a salt, the anion is able to form hydrogen bonds with the HBD, thus lowering the COULOMB interactions to the partner cation[1]. If now part of the anions from the choline chloride phase accumulate at the choline chloride–imidazole interface due to hydrogen bonding, the choline chloride bulk is left with a lack of anions. Hence, COULOMB repulsion takes place between the choline cations, their intermolecular distance gets increased and water then has an easy way to be incorporated into the choline-rich phase without increasing the sample's volume, the mixture thus can be described as a porous-like liquid. Figure 4.12 visualizes the water incorporation into the choline-rich phase. The extensive water incorporation has a great impact on some of the physicochemical properties, such as density and viscosity. Other properties seem to be influenced rather by the rigidity of the imidazole lattice and/or the inaccessibility of all imidazole molecules and thus show only small changes upon the addition of water, *e.g.* refractive index, pH and conductivity. It was once again shown that a detailed knowledge about the microscopic structure of a substance is key in order to explain macroscopic properties.

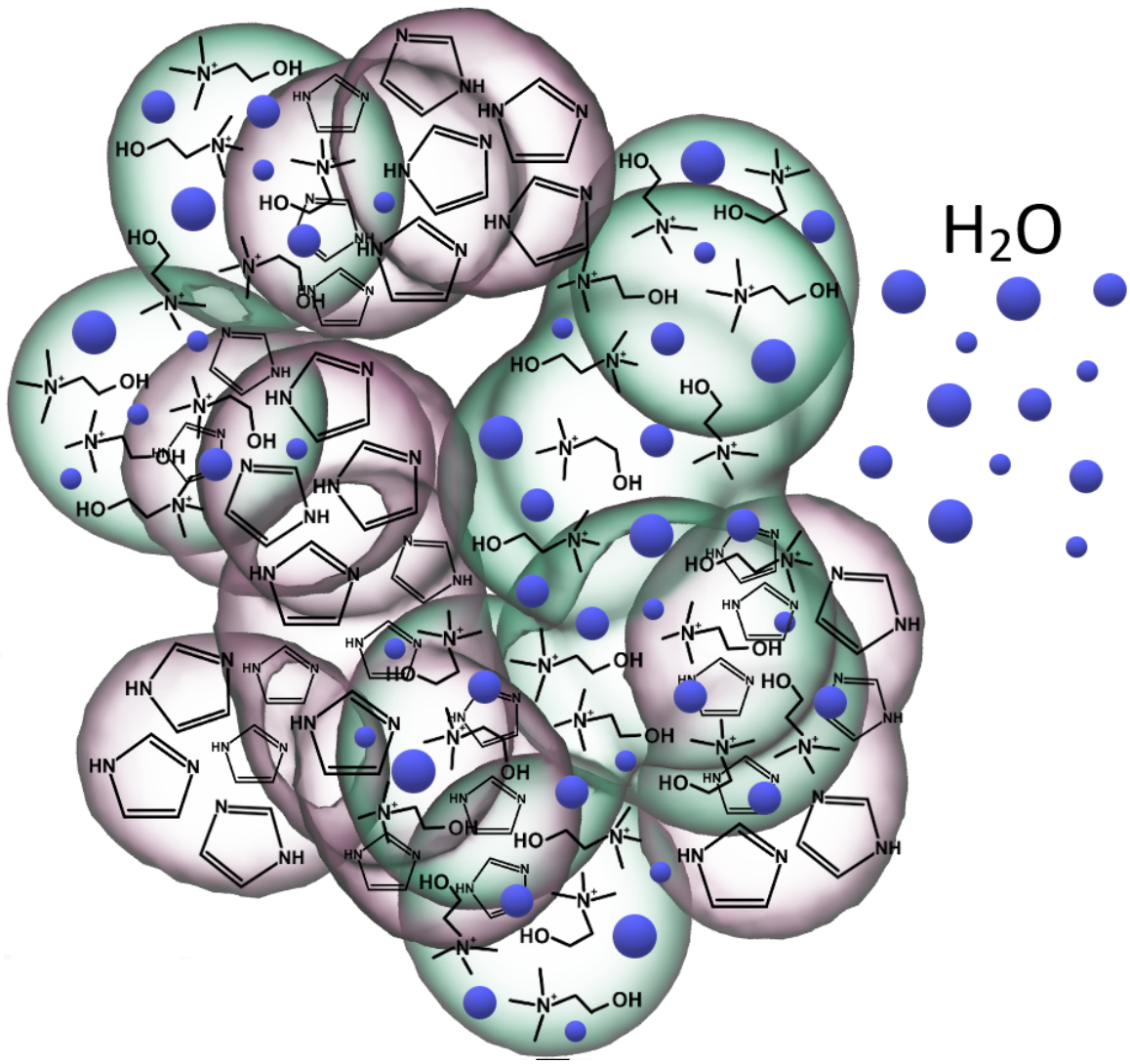

Figure 4.12: Schematic representation of the incorporation of water into the choline-rich phase of the choline chloride–imidazole mixture.

5 Investigation of structure formation of MBP induced by ionic liquids

5.1 Introduction

As investigated in the previous studies substantially, ionic liquids and ionic liquid-like DES show a high extent of self-aggregation and formation of nano-domains. In this study the effect of these structures on the myelin basic protein was investigated. The myelin basic protein (MBP) belongs to the intrinsically disordered proteins, its formation of protein tertiary structures takes place only at presence of lipid bilayers of biomembranes.[19,20] MBP is a component of the myelin sheath which insulates the nerve cell axons. It has been determined that the myelin sheath of multiple sclerosis (MS) patients become porous and a leakage of MBP arises.[21] Until now no possibility has been found to crystallize the myelin basic protein. The aim of this study is to investigate the MBP's structure in presence of the unique transient bulk structures provided by ionic liquids in order to contribute to the understanding of factors and parameters that enhance or diminish the structure formation of MBP.

Thereby, three imidazolium-based ionic liquids were used with different alkyl chain length in order to mimic the Van der Waals forces and the underlying hydrophobic effect which is also the determining factor in lipid self-assembly. Figure 5.1 shows the structure of the three used ionic liquids: 1-Ethyl-3-methyl-imidazolium tetrafluoroborate ([EMIm][BF_4], **a**), 1-Butyl-3-methyl-imidazolium tetrafluoroborate ([BMIm][BF_4], **b**) and 1-Hexyl-3-methyl-imidazolium tetrafluoroborate ([HMIm][BF_4], **c**) with increasing alkyl chain length, respectively.

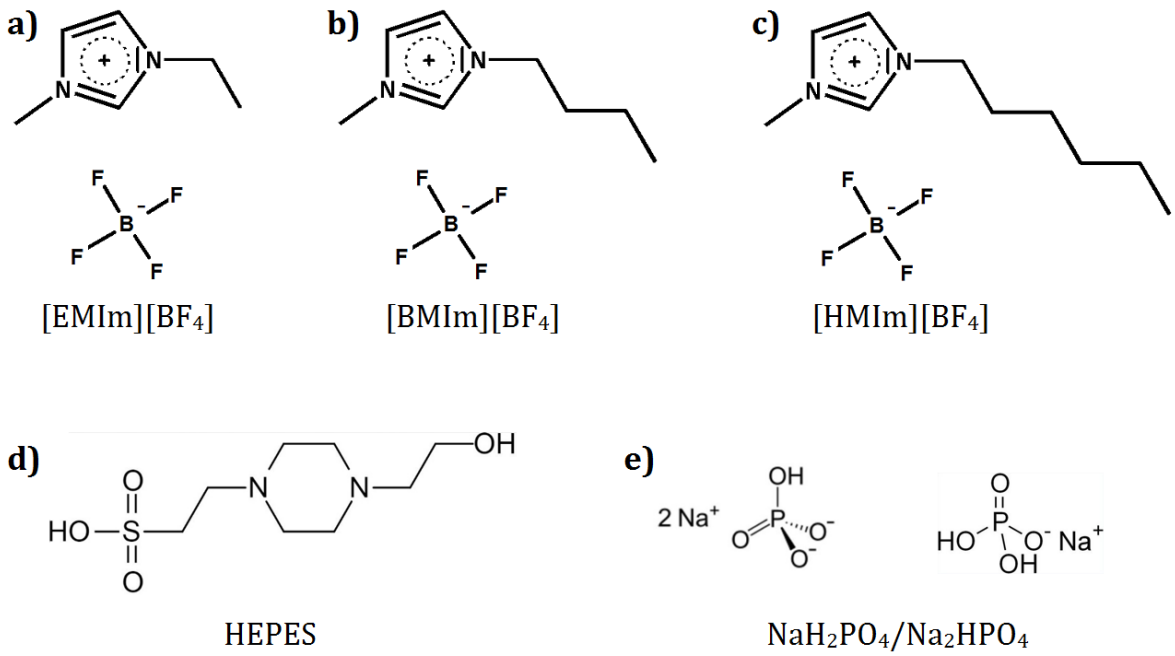

Figure 5.1: Structures of the used ionic liquids and buffer systems.

5.2 Experimental

5.2.1 Sample preparation

The freeze-dried MBP was solvated in a buffer solution and stirred slowly and carefully to avoid foaming. To ensure noise-free dynamic light scattering measurements, it is crucially important that the samples were free of any dust particles or other impurities. Therefore, a fresh buffer solution was filtered and then mixed with the ionic liquid in different mixing ratios and subsequently filtered a second time before combining it with the protein–buffer-solution. The protein solution could not be filtered because of the high adsorption affinity of the MBP on the filter surface. Following parameters were varied: the type of IL, the buffer, the protein concentration and the IL content, adding up to a total of 76 different samples (see Tab. 5.1). For the samples without buffer solution, *i.e.* in pure ionic liquid, an aqueous MBP solution was added to the IL to ensure a homogenous distribution of the protein in the sample. The samples then were lyophilized over night to remove the water.

Table 5.1: Parameter variation of all samples investigated.

		[EMIm][BF$_4$]			
phosphate	0 µM 0 % IL	0 µM 10 % IL	0 µM 25 % IL	0 µM 50 % IL	
	2 µM 0 % IL	2 µM 10 % IL	2 µM 25 % IL	2 µM 50 % IL	
	5 µM 0 % IL	5 µM 10 % IL	5 µM 25 % IL	5 µM 50 % IL	2 µM 100 % IL
	10 µM 0 % IL	10 µM 10 % IL	10 µM 25 % IL	10 µM 50 % IL	2 µM 100 % IL
HEPES	0 µM 0 % IL	0 µM 10 % IL	0 µM 25 % IL	0 µM 50 % IL	5 µM 100 % IL
	2 µM 0 % IL	2 µM 10 % IL	2 µM 25 % IL	2 µM 50 % IL	10 µM 100 % IL
	5 µM 0 % IL	5 µM 10 % IL	5 µM 25 % IL	5 µM 50 % IL	
	10 µM 0 % IL	10 µM 10 % IL	10 µM 25 % IL	10 µM 50 % IL	

		[BMIm][BF$_4$]			
phosphate	–	0 µM 10 % IL	0 µM 25 % IL	0 µM 50 % IL	
	–	2 µM 10 % IL	2 µM 25 % IL	2 µM 50 % IL	
	–	5 µM 10 % IL	5 µM 25 % IL	5 µM 50 % IL	0 µM 100 % IL
	–	10 µM 10 % IL	10 µM 25 % IL	10 µM 50 % IL	2 µM 100 % IL
HEPES	–	0 µM 10 % IL	0 µM 25 % IL	0 µM 50 % IL	5 µM 100 % IL
	–	2 µM 10 % IL	2 µM 25 % IL	2 µM 50 % IL	10 µM 100 % IL
	–	5 µM 10 % IL	5 µM 25 % IL	5 µM 50 % IL	
	–	10 µM 10 % IL	10 µM 25 % IL	10 µM 50 % IL	

		[HMIm][BF$_4$]	
phosphate	–	0 µM 10 % IL	
	–	2 µM 10 % IL	
	–	5 µM 10 % IL	0 µM 100 % IL
	–	10 µM 10 % IL	2 µM 100 % IL
HEPES	–	0 µM 10 % IL	5 µM 100 % IL
	–	2 µM 10 % IL	10 µM 100 % IL
	–	5 µM 10 % IL	
	–	10 µM 10 % IL	

5.2.2 Dynamic light scattering

All DLS experiments were performed at the Anton Paar Litesizer 500 with a low volume quartz measurement cell. Both, sidescatter as well as backscatter mode were measured to obtain more information about the shape of the particles. For comparison, only the backscatter plots were used because they showed higher overall intensities. The analysis model was set to "narrow" and the cumulant model to "advanced". The viscosity and refractive indices were measured beforehand and entered into the menu sheet. For each sample, 6 measurements with 30 seconds of measurement time each were performed at 25 °C.

5.2.3 Rheology and refractive index

All solvent mixtures were investigated regarding their viscosity and refractive indices at 25 °C. Viscosity measurements were perfomed at a Physica MCR 301 from Anton Paar with a CP 25-2/TG spindel. Refractive indices were measured on a Anton Paar device.

5.3 Results and discussion

5.3.1 Dynamic light scattering

Characterization of the reference systems

Although being a very impurity-sensitive method, dynamic light scattering cannot give information on composition and structure of particles, only on size and size distribution. Therefore, conclusions on the behavior of MBP in different media can only be made by comparing the particle sizes of the respective sample with those of the protein in pure buffer solution as well as the pure solvent mixture without the protein. Since a fitting of the autocorrelation data is used to derive particle size distribution, a detailed evaluation of the significance of each reference sample's autocorrelation is crucial. In general, an autocorrelation ($g(t) \in [1, 2]$) above 1.3 is expected to be significant [52]. For correlations below that value, only trends can be given but the respective particle size distributions might not be substantial.

(EMIm)(BF_4) autocorrelations Figure 5.2 summarizes the dynamic light scattering autocorrelations of different amounts of the ionic liquid 1-ethyl-3-methyl-imidazolium tetrafluoroborate ([EMIm][BF_4]) in both used buffer solutions HEPES and phosphate buffer.

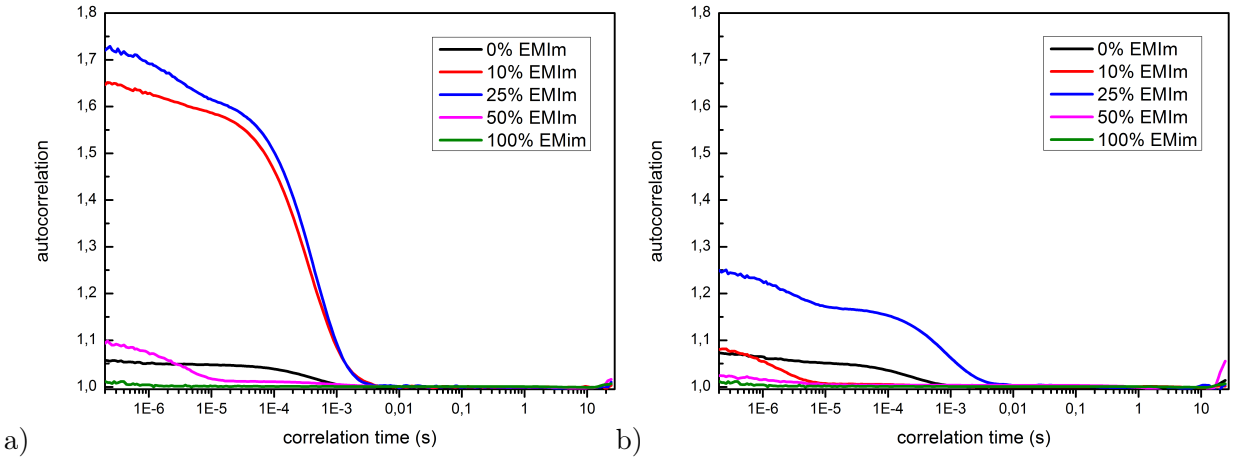

Figure 5.2: [EMIm][BF_4] in phosphate **(a)** and HEPES **(b)** buffer, shown are autocorrelation functions for different [EMIm][BF_4] contents.

Noticeable at first glance is the difference of the [EMIm][BF_4] autocorrelation in both buffers. In presence of the phosphate buffer the solvent mixture shows much higher $g(t)$ values (up to 1.8) than in HEPES buffer. Apparently, the small sodium phosphate salt molecules enforce a stronger structure formation of the solvent molecules compared to the hydroxyethyl-piperazine-ethanesulfonic acid (HEPES) molecules which are only partly dissociated ($pK_{a2} = 7.5$). The position of the autocorrelation decrease on the time axis is a measure of the particle size and thus, different species can be identified directly from the autocorrelation function by means of a multiple-step decrease.

Both, the pure buffer solution (black) as well as the pure ionic liquid (green) show very low autocorrelations (< 1.1). However, the small autocorrelations have a distinctive drop at certain positions on the x-axis (at $\log(t) \sim 0.000001$ and $\log(t) \sim 0.0001$, respectively). If now the solvent composition is raised, the overall autocorrelation increases at first and decreases again after a certain IL content. As can be exerpted from Fig. 5.2, the autocorrelation of the

[EMIm][BF_4]–phosphate buffer mixture behaves as following: 15 % > 25 % > 10 % ≫ 50 % ≳ 0 % ≳ 35 % ≳ 100 % [EMIm][BF_4]. In HEPES buffer solution the autocorrelation overall is not as high, but the descending order is similar: 15 % ≫ 25 % ≫ 10 % ≳ 0 % ≳ 35 % ≳ 50 % ≳ 100 %. In the HEPES buffer solution it becomes particularily apparent that the curves show a two step decline, one originating from the structures that form in pure buffer solution (at $\log(t) = 0.0001$; cf. black line in Fig. 5.2) and one which seems to stem from structures composed of ionic liquid clusters ($\log(t) = 0.000001$).

(BMIm)(BF_4) autocorrelations If now the alkyl side chain of the IL cation is increased from ethyl to butyl, the hydrophobic domain gets enlarged which has an effect on water solubility and the possibility to form structures (e.g. lamellar or micellar aggregation by means of the hydrophobic effect). Figure 5.3 shows the reference samples with the same parameters and mixture contents as for the [EMIm][BF_4] described above.

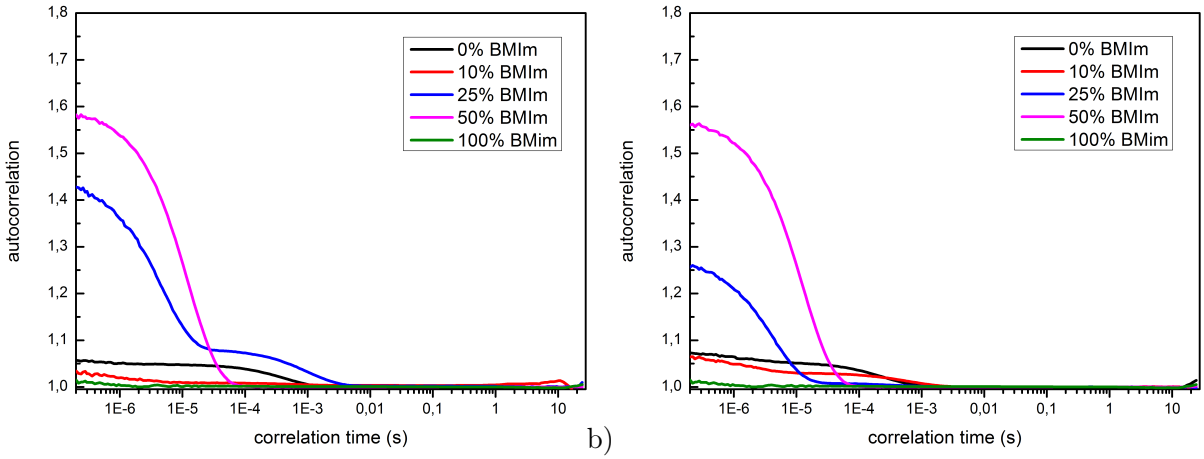

Figure 5.3: [BMIm][BF_4] in phosphate **(a)** and HEPES **(b)** buffer, shown are autocorrelation functions for different [BMIm][BF_4] contents.

In terms of autocorrelation amplitude, the maximum of [BMIm][BF_4] in phosphate buffer is smaller compared to [EMIm][BF_4] in phosphate buffer (1.6 for the 50 % [BMIm][BF_4] vs. 1.8 for the 15 % [EMIm][BF_4]). The mentioned 50 % [BMIm][BF_4] sample also shows the highest autocorrelation in HEPES buffer, higher than any of the [EMIm][BF_4] samples in HEPES. It

seems that this specific mixture with a [BMIm][BF_4] content of 50 % shows overall very high autocorrelations and is not affected significantly by the choice of the buffer.

Reason for the immunity to the choice of buffer might be that the structure forming parameter for the [BMIm][BF_4] samples is their non-polar butyl chains which probably outweigh the polar regions. Therefore the small charged phosphate ions have a less impact compared to the [EMIm][BF_4] samples.

The structures that come from the pure buffer (black line, small shoulder at $\log(t) = 0.0001$), both, in phosphate and HEPES are still present at low [BMIm][BF_4] contents but seem to collaps at [BMIm][BF_4] contents of $\sim$ 35 %. Starting from this IL concentration, the autocorrelation at $\log(t) = 0.0001$ is vanished and only a strong autocorrelation at $\log(t) = 0.000001$, which starts to arise at 10 % of [BMIm][BF_4], is visible. Interestingly, the sample of 35 % [BMIm][BF_4] in HEPES buffer shows an anomaly by having a very low autocorrelation compared to both, the 25 and 50 % [BMIm][BF_4] samples.

However, the [BMIm][BF_4] samples show a very high autocorrelation which means that they allow for strong structure formation if a mixture of 50 : 50 (v/v) [BMIm][BF_4] : buffer solution is established, in both, phosphate and HEPES buffer. Their butyl chains may cause the formation of micellar-like structures, thereby the critical micelle concentration seems to be somewhere above 25 % [BMIm][BF_4], the ideal [BMIm][BF_4] concentration is evaluated in a later study and was estimated to be at $\sim$ 46 %.[53].

(HMIm)(BF_4) autocorrelations [HMIm][BF_4] has a hexyl side chain and thus, the non-polar domains are even larger. Unfortunately, this leads to a limited solubility in water. Therefore only the 10 % [HMIm][BF_4] sample could be prepared without causing phase separation. As it can be seen in Fig. 5.4, the two [HMIm][BF_4] samples, 100 % and 10 % [HMIm][BF_4] content, show extremely low autocorrelations: 1.01 and 1.12, respectively. It seems that in its pure form as well as in mixture, the [HMIm][BF_4] cannot form optically distinguishable structures.

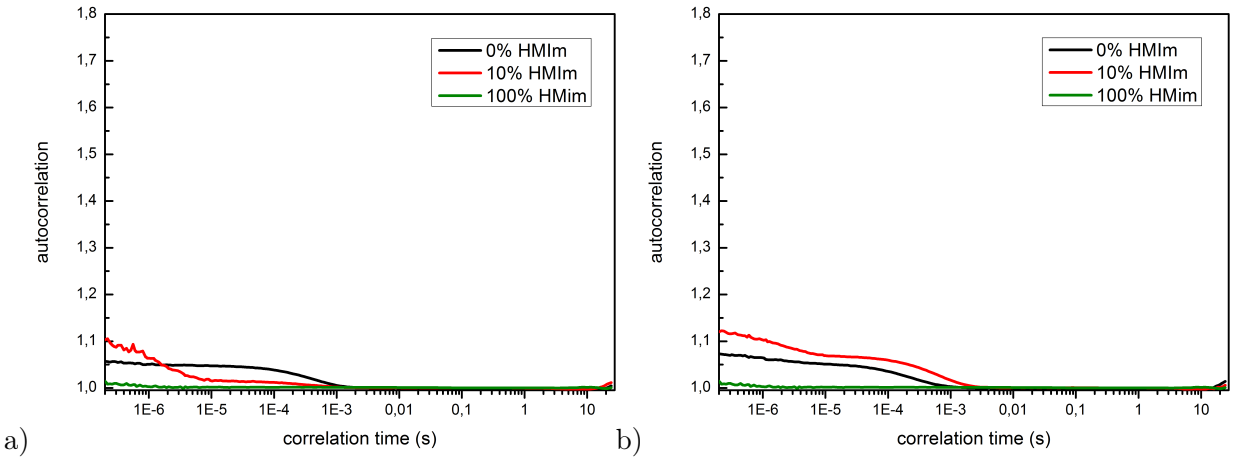

Figure 5.4: [HMIm][BF_4] in phosphate **(a)** and HEPES **(b)** buffer, shown are autocorrelation functions for different [HMIm][BF_4] contents.

For all three different ionic liquids, it is the [BMIm][BF_4] in its 50 % mixture that shows the highest structure formation which is also unaffected by the choice of buffer solution. Apart from that specific mixture, it is the phosphate buffer that enhances structure formation, probably because of its small charged particles which can interact very well with the ionic liquid. The [HMIm][BF_4] samples could only be prepared up to a content of 10 % without phase separation happening and they show very low optically distinguishable structures in solution.

MBP autocorrelations Measurements showed that the MBP itself tends to form aggregates in buffer solution. Figure 5.5 visualizes the autocorrelations of MBP in both buffer solutions in three different concentrations, 2, 5 and 10 µM. In HEPES buffer, the autocorrelation is similar for all protein concentrations at $\sim$ 1.5. In phosphate buffer the autocorrelation increases with increased protein concentration. Apparently, the HEPES buffer tends to stabilize the aggregates even in lower protein concentrations. Noticeable is that the buffer itself shows structure formation to some extent but their autocorrelation is very low.

If now the autocorrelation functions are converted into particle size distributions (Fig. 5.6), it becomes apparent that the structures are of sizes between 500 and 1000 nm, whereas the

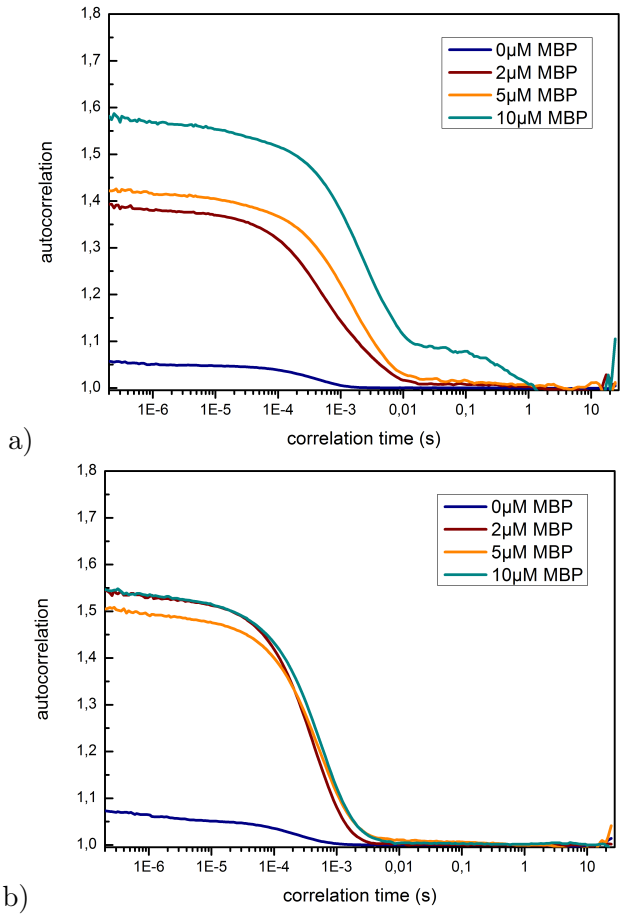

Figure 5.5: Reference autocorrelation functions of the protein samples in different concentrations in phosphate **(a)** and HEPES **(b)** buffer solutions without any added ionic liquid.

structures in HEPES show a broader size distribution, possibly including several different sized species, whereas in phosphate buffer we have two distinct and differently sized species. However, the large sizes do indeed confirm the presence of aggregates.

In the following, the effect of the ionic liquids on the MBP aggregates and *vice versa*, the effect of the MBP on the ionic liquid structures is investigated. Thereby, the particle size distributions are compared which give a more comprehensive view on the structural changes upon variation of the parameters.

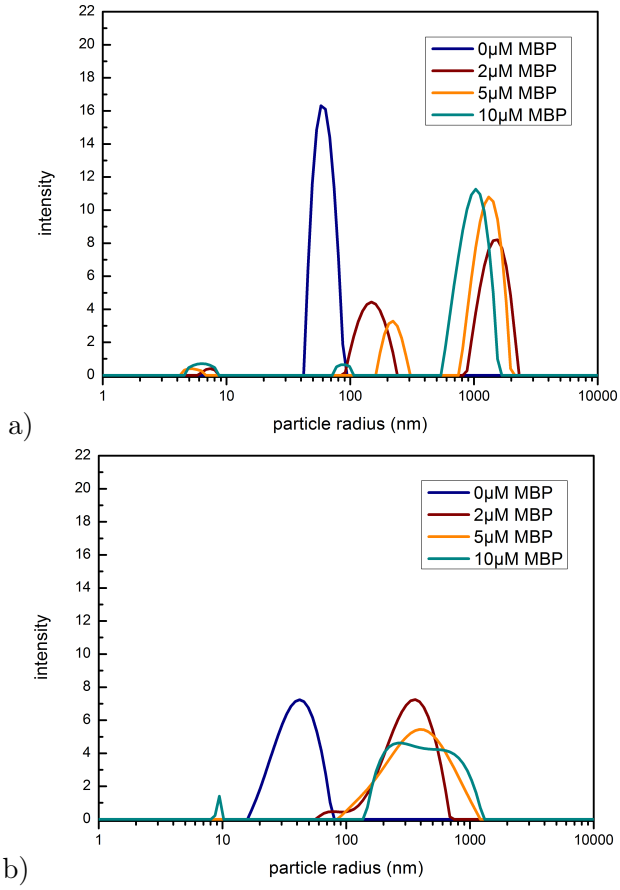

Figure 5.6: Reference particle size distributions calculated from the autocorrelations of the protein samples in different concentrations in phosphate **(a)** and HEPES **(b)** buffer solutions without any added ionic liquid.

MBP in (EMIm)(BF_4)

Considering Fig. 5.2 it was determined that the autocorrelations of the pure [EMIm][BF_4]–buffer-mixtures are generally quite low. From the three measured IL mixtures (10, 25, 50 %), the 25 % mixture shows the highest autocorrelation with $\sim$ 1.25, this means that the particle size distribution charts although showing a distinct peak for the pure solution mixture are probably only insignificantly few structures.

Particle size distributions in HEPES buffer Figure 5.7 shows the particle size distributions of different added amounts of [EMIm][BF_4] in HEPES buffer solution with 2 µM of added

MBP. For each frame the structures of the pure IL–buffer solvent mixture without protein (black), the pure protein–buffer-solution without ionic liquid (red) and the actual sample of interest – protein in IL-buffer mixture (blue) are compared.

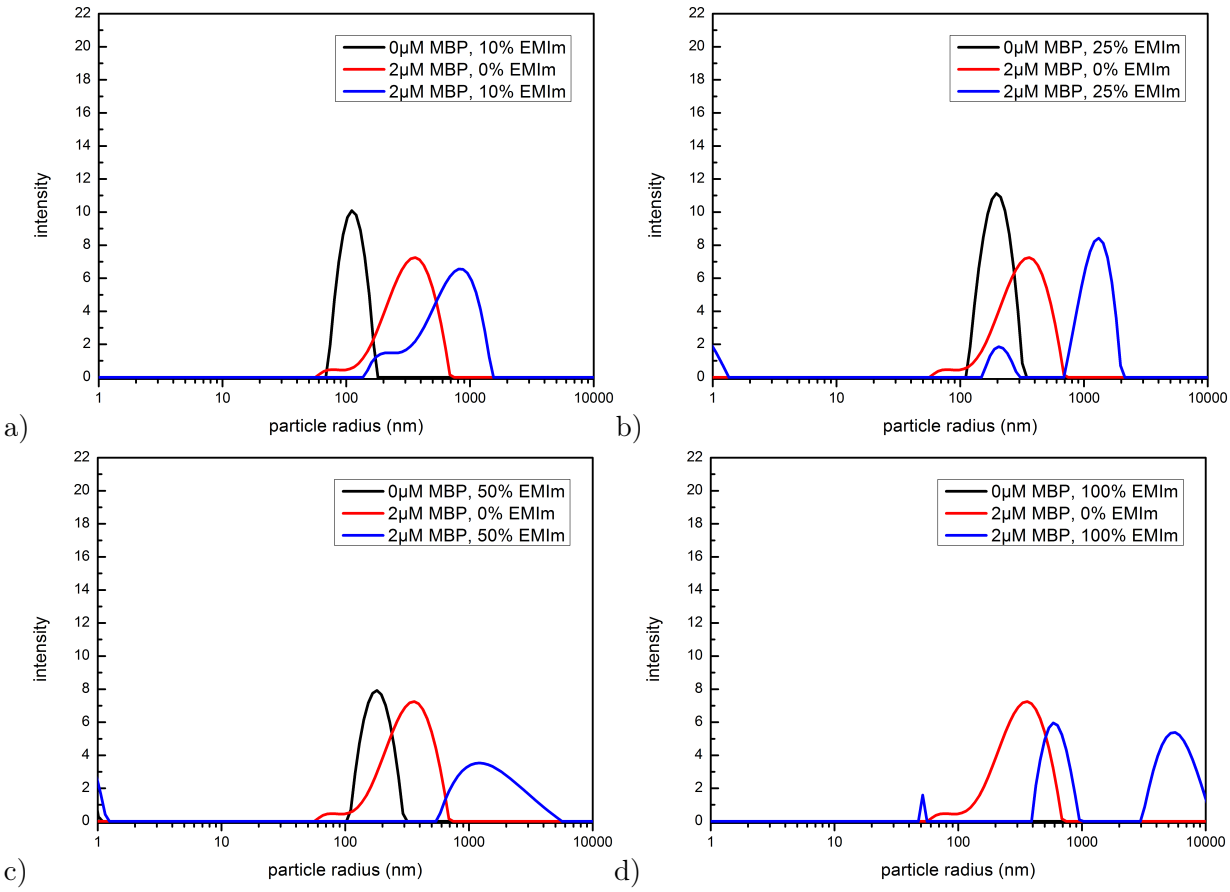

Figure 5.7: Particle size distributions of MBP in [EMIm][BF_4]–phosphate buffer mixtures: **(a)** 10 % [EMIm][BF_4], **(b)** 25 % [EMIm][BF_4], **(c)** 50 % [EMIm][BF_4], **(d)** 100 % [EMIm][BF_4]. For each image, the reference plots of the pure solvent mixtures without MBP as well as the MBP in pure buffer solution are shown.

Figure 5.7a shows the particle size distributions of 2 µM MBP in a solvent mixture consisting of 10 % [EMIm][BF_4] and 90 % HEPES buffer solution. The protein in buffer solution forms structures represented by the red two-peaked size distribution, one peak at $\sim$ 70 nm and the second at $\sim$ 400 nm. When MBP is introduced into the 10 : 90 [EMIm][BF_4]–buffer-mixture,

the particle sizes shift to higher values (blue line), 220 and 880 nm, respectively. It seems as if the protein aggregates become enlarged due to the presence of [EMIm][BF_4]. Both aggregate sizes are shifted equally, reason for this could be agglomeration of the charged [EMIm][BF_4] onto the charged protein hence enlarging the already existing structures.

With increased concentration of the [EMIm][BF_4] in HEPES buffer, the particle size distributions shift to higher radii. In the pure ionic liquid, the MBP forms different sizes of aggregates.

If not the ionic liquid but the protein concentration is increased while the ionic liquid content in HEPES buffer is constant, a shift to higher particle sizes can be observed, implying increased aggregation.

Particle size distributions in phosphate buffer Figure 5.8 displays the particle size distributions of the same amounts of [EMIm][BF_4] and the same MBP concentrations as above, but in a phosphate buffer solution.

It can be seen that the particle size distribution in phosphate buffer is more complex. The addition of 10 % [EMIm][BF_4] causes a decrease of the protein aggregate intensity and the distribution of different particle sizes is broadened (*cf.* red line to blue line), indicating aggregate structures of different sizes and shapes. With increased [EMIm][BF_4] concentration two separate particle sizes become apparent at 15 and 18 nm, respectively. These intensities decrease while a new peak at very small particle sizes emerges (however, the dynamic light scattering method limits at particle sizes around 1 nm). This phenomenon can be explained with a dissolving of the protein aggregates in smaller oligomeric units with low scatter intensity. Interestingly, the large structures that are formed by pure [EMIm][BF_4] in phosphate buffer solution disappear once the MBP is added (*cf.* black line vs. blue line). In pure [EMIm][BF_4] no intrinsic structures are formed, but Fig. 5.8d gives information about how the MBP aggregates in phosphate buffer change if the buffer is substituted with pure [EMIm][BF_4]. For each pure solvent, there are 3 different sizes of MBP aggregates present. However, the particle size distributions each switch to sizes approx. 5 times larger if [EMIm][BF_4] is the solvent

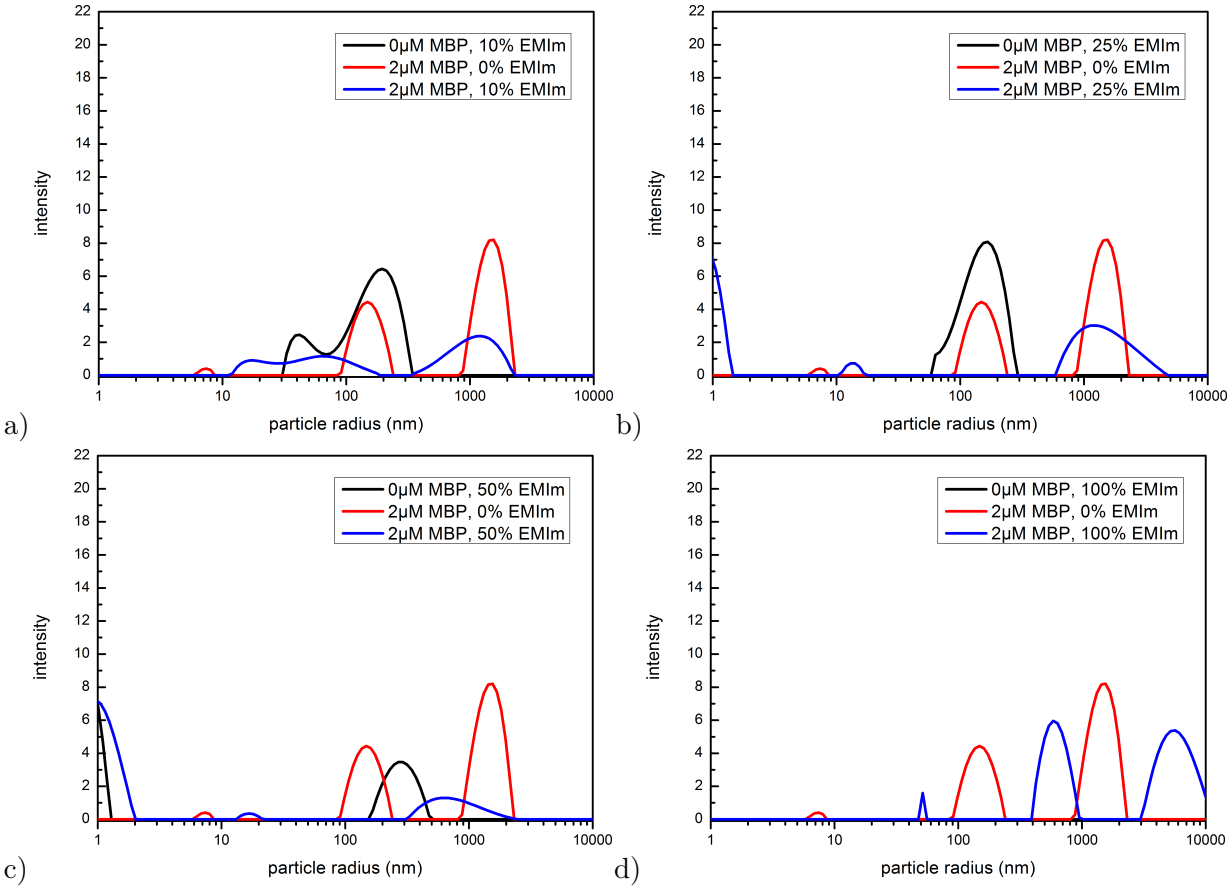

Figure 5.8: Particle size distributions of MBP in [EMIm][BF_4]–phosphate buffer mixtures: **(a)** 10 % [EMIm][BF_4], **(b)** 25 % [EMIm][BF_4], **(c)** 50 % [EMIm][BF_4], **(d)** 100 % [EMIm][BF_4]. For each image, the reference plots of the pure solvent mixtures without MBP as well as the MBP in pure buffer solution are shown.

compared to phosphate buffer. It seems that the solvent shell is much bigger if it is comprised of [EMIm][BF_4]. The interactions between [EMIm][BF_4] molecules are stronger compared to the diluted phosphate salts, which even may cause agglutination of several MBP aggregates including their [EMIm][BF_4] solvent shells. Another hint to agglutination of the MBP aggregates shows the sample with 5 µM MBP in pure [EMIm][BF_4] (see Fig. A16) where only a single aggregate particle size distribution at $\sim$ 1000 nm becomes apparent. The same effect is visible for the 10 µM MBP samples (Fig. A17), big aggregates are formed in pure ionic liquid.

MBP in (BMIm)(BF_4)

As has been stated in Chap. 5.3.1, the autocorrelations for certain [BMIm][BF_4] contents in both buffers were extraordinarily high and with an early decay. Thus, a strong structure formation can be assumed for these [BMIm][BF_4]–buffer-mixtures. For further characterization of these assumed structures, the particle size distributions are taken into consideration. A study of Zheng et al. showed that at a mole fraction of water $x_{\mathrm{w}} > 0.9$ – which is a mixture of [BMIm][BF_4] : water approx. 50 : 50 v/v – the cation–anion pair/cluster interaction gets broken apart[54]. This probably facilitates hydrophobic butyl–butyl interaction. Additionally it was shown that the BF_4^- anion does not form strong hydrogen bonds with the $BMIm^+$ cation which might be the reason for easy nanophase separation[55].

Particle size distributions in HEPES buffer Analoguous to the [EMIm][BF_4] samples, the particle size distributions of the [BMIm][BF_4] samples are shown in Fig. 5.9.
In agreement with the analysis of the autocorrelation functions, the 10 and 100 % [BMIm][BF_4] samples show no particle size distributions. Interestingly, when the [BMIm][BF_4] content is increased to 25 % and subsequently to 50 %, the solvent alone without added protein already shows a defined particle size distribution with a maximum at $\sim$ 2.9 and 5.1 nm respectively (see Fig. 5.9b and c, black lines). It thus can be assumed that structures are formed and that they have relatively small diameters compared to the structures observed for [EMIm][BF_4]. If now the MBP is introduced to these structures it can be seen that the peak intensity of the large MBP aggregates decreases and a new peak at small particle sizes emerges (see Fig. 5.9b and c, blue lines). The disappearance of the aggregates could either be a complete dissolving of the MBP molecules or an incorporation of MBP into the structures that are formed by [BMIm][BF_4]. The size of the particles formed by [BMIm][BF_4] is in the range of small micelles. In pure [BMIm][BF_4] where no intrinsic structures by the ionic liquid itself exist, the DLS shows a sharp particle size distribution at $\sim$ 174 nm upon addition of the MBP. The [BMIm][BF_4] medium seems to force the MBP into aggregates which are smaller than the aggregates in HEPES buffer alone.

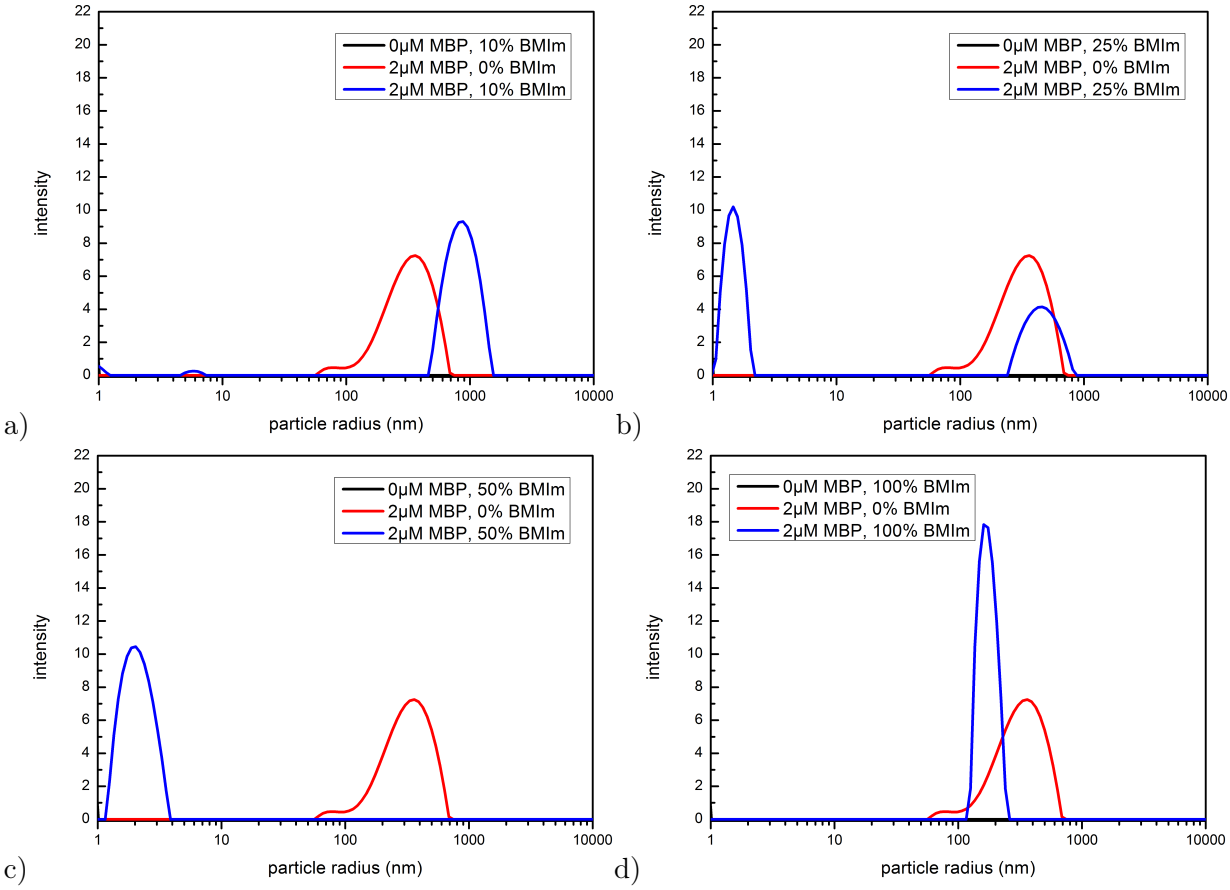

Figure 5.9: Particle size distributions of MBP in [BMIm][BF_4]–phosphate buffer mixtures: **(a)** 10 % [BMIm][BF_4], **(b)** 25 % [BMIm][BF_4], **(c)** 50 % [BMIm][BF_4], **(d)** 100 % [BMIm][BF_4]. For each image, the reference plots of the pure solvent mixtures without MBP as well as the MBP in pure buffer solution are shown.

The same particle size formation can be observed for higher MBP concentrations as well. However, the protein concentration is too high to be dissolved/incorporated completely, so that additionally to the smaller structures, aggregates are still visible in the particle size distribution plots in Figs. A18 and A19.

Particle size distributions in phosphate buffer In phosphate buffer solution, the structures formed by the ionic liquid itself and by the MBP are more complex.

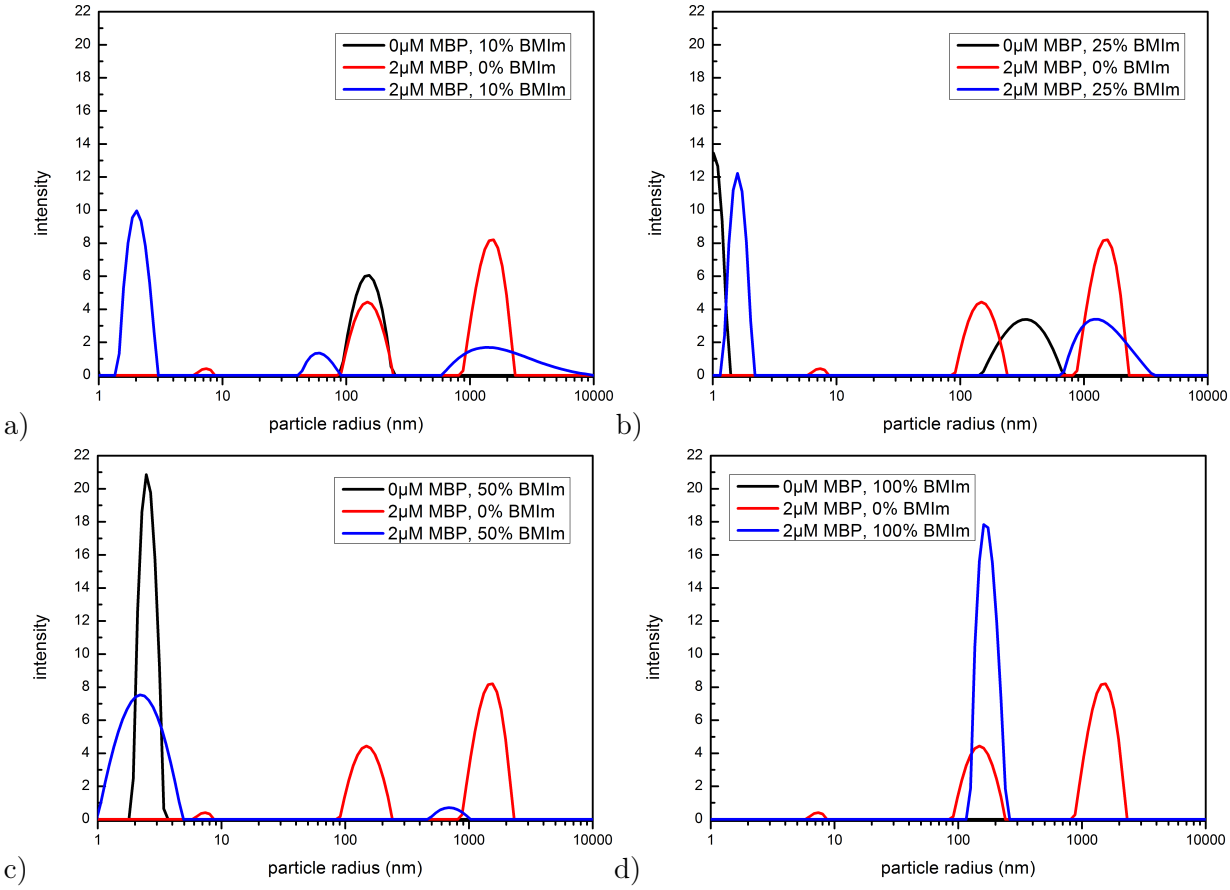

Figure 5.10: Particle size distributions of MBP in [BMIm][BF_4]–phosphate buffer mixtures: **(a)** 10 % [BMIm][BF_4], **(b)** 25 % [BMIm][BF_4], **(c)** 50 % [BMIm][BF_4], **(d)** 100 % [BMIm][BF_4]. For each image, the reference plots of the pure solvent mixtures without MBP as well as the MBP in pure buffer solution are shown.

A detailed view on the particle size distributions of the pure solvent without added protein with increasing [BMIm][BF_4] content (Fig. 5.10a–d) reveals that there are initial structures with relatively large particle radii ($\sim$ 150 nm). If 25 % [BMIm][BF_4] content is reached, the structures get enlarged to $\sim$ 350 nm while a second peak at very low sizes emerges. This is in agreement with the autocorrelations for 15 and 25 % [BMIm][BF_4] in Chap. 5.3.1 which show

a two-step decline. At 50 % [BMIm][BF_4] content is reached however, only a single species can be observed in the particle size distribution plot (see Fig. 5.10c). The maximum of this narrow peak lies at $\sim$ 2.5 nm, which is slightly smaller than the structures observed in HEPES buffer.

MBP in phosphate buffer solution shows several peaks at different size distributions. Apparently, the charged character of the phosphate compared to HEPES prevents the MBP to fully agglomerate, instead, several smaller aggregates exist. If 10 % [BMIm][BF_4] are added, which intrinsically forms structures at about 150 nm in size, there are still 3 peaks with different particle size distributions visible. However, the peak of the largest particle size (large MBP aggregate peak) gets broadened, whereas the other two peaks shift to smaller sizes. Interestingly hereby is the very sharp and intense peak at $\sim$ 2 nm, which lies in the size order of small micelles or nanocluster. The peak becomes more intense if the [BMIm][BF_4] content is increased to 25 %. At 50 % [BMIm][BF_4] content, the size of the structures formed by the [BMIm][BF_4] itself has the same size as the small structures that start forming once a bit of [BMIm][BF_4] is added to the MBP in phosphate buffer (*cf.* Fig. 5.10a-c; blue lines vs. 5.10c; black line). However, at 50 % [BMIm][BF_4] – the mixture which showed very sharp micellar structures when mixed with HEPES buffer – the peak at 2–2.5 nm gets broadened when MBP is introduced to the solvent mixture. Maybe both species, small MBP clusters as well as [BMIm][BF_4] micelles co-exist at the same time, or the MBP gets incorporated into the [BMIm][BF_4] structures. This cannot be distinguished by dynamic light scattering at this time.

MBP in (HMIm)(BF_4)

[HMIm][BF_4] is the most non-polar of the three investigated ionic liquids. It is miscible with water up to 10 %, therefore only samples with 0, 10 and 100 % [HMIm][BF_4] were prepared. The autocorrelation functions already revealed that the autocorrelation values are very low, hence any peaks that can be seen in Figs. 5.11a or 5.12a (black lines) should not be taken as stable structures that are present in high quantities.

Particle size distributions in HEPES buffer In pure HEPES buffer solution the typical MBP aggregate peak can be seen in Fig. 5.11, red line.

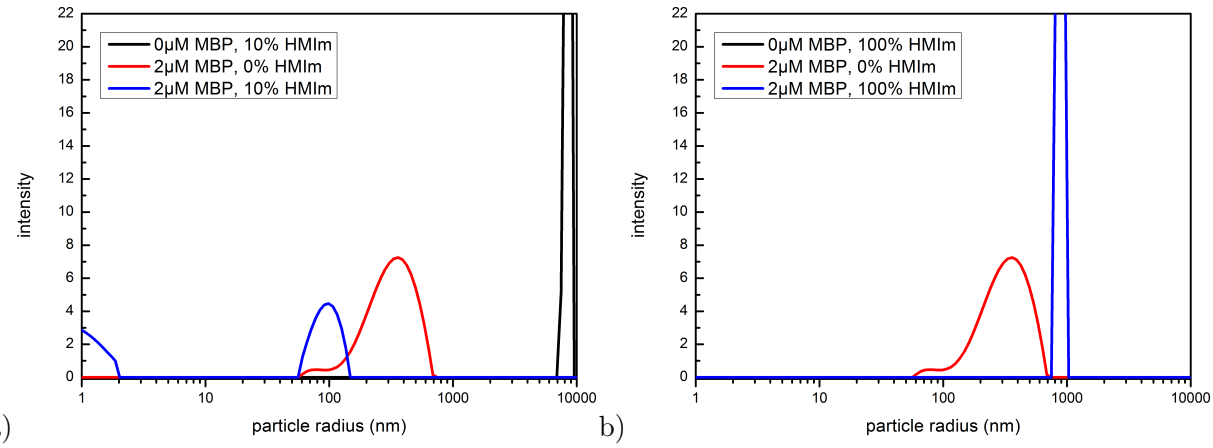

Figure 5.11: Particle size distributions of MBP in [HMIm][BF_4]–HEPES buffer mixtures: **(a)** 10 % [HMIm][BF_4], **(b)** 100 % [HMIm][BF_4]. For each image, the reference plots of the pure solvent mixtures without MBP as well as the MBP in pure buffer solution are shown.

If now 10 % of [HMIm][BF_4] are added, the aggregate peak has completely vanished, instead, two other peaks emerge, one at very low particle sizes (< 2 nm) and one at $\sim$ 95 nm (Fig. 5.11, blue line). But from autocorrelation analysis that show very low values, a significance of these structures cannot be justified. The most interesting is that the MBP aggregate peak has completely disappeared. This means that only 10 % of added [HMIm][BF_4] lead to a dissolving of the MBP aggregates. However, in pure [HMIm][BF_4], a strong aggregation of MBP is enforced which can be seen in Fig. 5.11b; a very narrow peak at $\sim$ 880 nm is visible.

Particle size distributions in phosphate buffer In phosphate buffer solution MBP aggregation can be seen (Fig. 5.12, red line), however, with 10 % added [HMIm][BF_4], the particle sizes look very complex.

They are distributed over a wide range from $\sim$ 7–1000 nm with 3 local maxima. As the samples with [EMIm][BF_4] and [BMIm][BF_4] in phosphate buffer already showed, that the

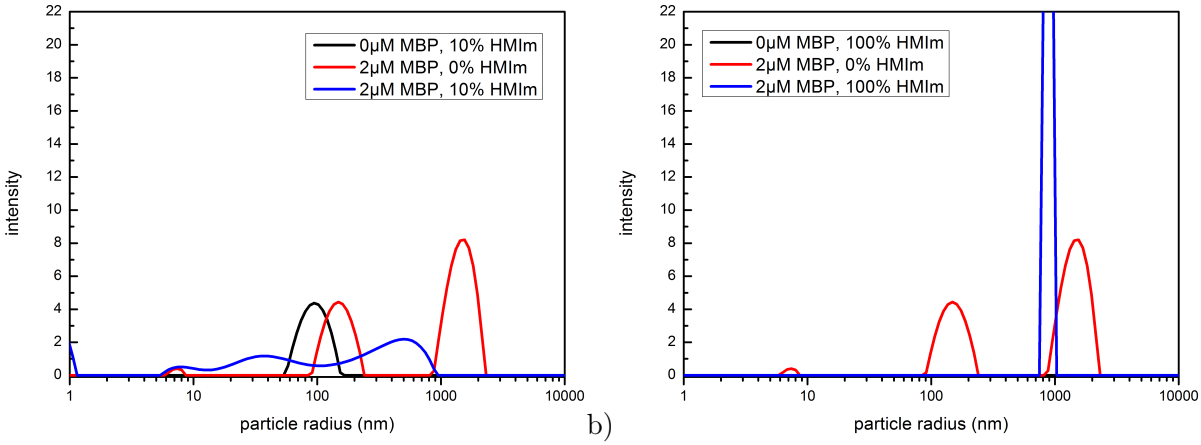

Figure 5.12: Particle size distributions of MBP in [HMIm][BF_4]–phosphate buffer mixtures: **(a)** 10 % [HMIm][BF_4], **(b)** 100 % [HMIm][BF_4]. For each image, the reference plots of the pure solvent mixtures without MBP as well as the MBP in pure buffer solution are shown.

small charged phosphate molecules act as competitor ions with the ionic liquid, enforcing a larger variety of structures of the ionic liquids themselves as well as of the protein clusters.

Summary

The analyses of the samples with three different ionic liquids, two different buffer solutions and three different protein concentrations revealed a very delicate balance of all three factors regarding structure formation.

The ionic liquids [EMIm][BF_4] and [HMIm][BF_4] showed no significant intrinsic structure formation in buffer solution. All used ionic liquids are rather amphiphilic, their charged imidazolium ring serves as a hydrophilic head group and their alkyl chains with varying length are the hydrophobic tails. Thereby, the length of the alkyl chain dictates the hydrophobicity and hence, the ability to form micellar/lamellar structures. Dynamic light scattering data let assume that [EMIm][BF_4] and its rather short ethyl chain is not sufficiently hydrophobic in order to form stable structures. On the contrary, the hydrophobic domains in [HMIm][BF_4] are too large, resulting in phase separation after an addition of more than 10 % v/v to the buffer solu-

tion. Therefore, both ionic liquids are not able to offer structures where the MBP molecules are bound to. For [EMIm][BF_4], an enlargement of MBP aggregates can be observed, presumably the [EMIm][BF_4] molecules form a large solvation shell around the MBP aggregates. However, [HMIm][BF_4] shows the opposite: the MBP aggregates are dissolved completely, but since the autocorrelations are very low, it can be assumed that there is no structure formation between MBP–[HMIm][BF_4]–buffer. The exception hereby is the [BMIm][BF_4] at a mixing ratio of 50:50 $v : v$ which already showed strong autocorrelations and high peak intensities at particle sizes in the size order of micellar/tubular structures. And indeed, upon presenting these structures to MBP aggregates, the aggregates disappear and the strongly visible small (micellar) structures are preserved. It is very likely that the MBP molecules can be incorporated into the structures offered by the [BMIm][BF_4], in the same way that MBP forms structures in biomembranes[19]. This is in agreement with studies of [BMIm][Cl] mixed with other proteins (*e.g.* BdpA) where the author's found out that the $BMIm^+$ cation strongly accumulate at each other and around the protein surface, hence expelling water as well as chloride anions out of the protein's proximity and therefore protecting the carbonyl backbone from H-bonds. This effect enhances the protein structure stability[56].

The buffer The choice of buffer solution has an impact on both, the MBP aggregation as well as the ionic liquid structures. The autocorrelation analyses showed that the ionic liquid structures in phosphate buffer are stronger than those in HEPES buffer solution. It seems like the charged phosphate ions help stabilizing the structures of the ionic liquids. However, the effect on the protein aggregates is different. While HEPES forces MBP into a single aggregate species, phosphate buffer causes the formation of several MBP aggregates of different sizes. Hence, there are two opposing effects that come together when the MBP is introduced into the ionic liquid–buffer mixture. In summary, the samples with the most uniform and stable particles are those in HEPES buffer solution, although phosphate should facilitate stabilizing the intrinsic structures formed by ionic liquids. Obviously, the phosphate ions pose a stronger competition to the ionic liquids regarding the molecular interactions between MBP and ionic liquids, causing several different sized MBP–ionic liquid clusters. Only exception are the

[BMIm][BF_4]–buffer samples with a mixing ratio of 50 : 50 v/v. For both buffers, a single species at the similar low particle sizes is visible in the DLS measurements. This means that the structures formed by [BMIm][BF_4] are not affected significantly by the choice of buffer. Hence, the structures are probably caused by the hydrophobic effect of the butyl side chains in water.

The MBP concentration The effect of an increase of protein concentration is very similar overall for every sample investigated. With increased MBP content, the aggregate sizes as well as their quantity increases. If there were several aggregate peaks at low MBP concentrations in the first place, an increase of added protein concentration causes a fusion into only one aggregate species. The above Fig. 5.6 shows a comparative example of the effect of protein concentration raise.

5.3.2 Small angle X-ray scattering

In order to get a confirmed image on the assumed micellar structures in the [BMIm][BF_4]–buffer samples with a mixing ratio of 50 : 50 v/v, small angle X-ray scattering was performed. The time between sample preparation and measurement however exceeded the average protein stability. Nevertheless, a first coarse measurement of the 50 : 50 [BMIm][BF_4]–buffer mixture indeed showed micellar-like structures. Further detailed measurements are planned.

5.4 Conclusions

The myelin basic protein is an intrinsically disordered protein in solution. In its natural biological surrounding – the myelin sheath – it is able to form tertiary structures in the presence of a membrane double layer, especially with negatively charged lipids. Ionic liquids are known to feature a high self-organizing character. When combining the MBP with its need for external structures with the ionic liquids and their ability for self-organization, different effects come to presence, depending on the length of alkyl side chain of the ionic liquids, their content, the choice of buffer and the protein concentration. The main factor for IL–MBP-interaction was established to be the ionic liquid's alkyl chain length. The balance of polar and non-polar

domains in the ionic liquid dictates the extent of self-organization and thus, the ability to interact with MBP. [EMIm][BF_4] did not show significant formation of self-organized structures and caused the MBP aggregates to grow larger in size. [HMIm][BF_4] however did also not show structure formation in the 10 % content sample but caused the MBP aggregate peaks to vanish in the DLS measurements, indicating a dissolving of MBP in the [HMIm][BF_4]–buffer samples. The non-polar domains in [HMIm][BF_4] are very large and probably can penetrate the MBP aggregates and hence causes them to break up. In contrast, [BMIm][BF_4] mixed with aqueous buffer solution in a 1 : 1 ratio showed the formation of micellar/short tubular structures which could be confirmed by means of SAXS measurements as well. In that case, the non-polar domains would point inward and the imidazolium cationic heads would form the outer micellar wall, surrounded by the BF_4^- anions through Coulomb interaction. Interestingly, these structures caused the MBP aggregates to vanish, indicating a possible incorporation of the protein into the micelles. This would mean that indeed, the [BMIm][BF_4] micelles – that formally appear negatively charged because of the anionic shell – are able to mimic a biomembrane in the MBP's point of view. With the knowledge that MBP can be forced into folding by providing an artificial membrane, more directed investigation towards e.g. the MBP leakage of Alzheimer's patients can be initiated.

6 Summary and outlook

In this study, three different topics about ionic liquids and ionic-like systems were studied. For the first experiment, a mixture of 1-ethyl-3-methyl-imidazolium chloride with urea is investigated. [EMIm][Cl] already is an ionic liquid with a melting point of 80 °C (90 °C determined by Tsuda et al.[22], respectively). With addition of urea the melting point can be decreased even further. However, over the whole molar fraction range, two local melting point minima at 25 : 75 [EMIm][Cl] : urea and 72.5 : 27.5 [EMIm][Cl] : urea and a melting point maximum at 50 : 50 [EMIm][Cl] : urea exist, *i.e.* a dystectic mixture is formed. For an easier access to this system's liquid states, especially its melting point minima are of interest. Curiously, both melting point minima have a similar melting temperature (60 ± 2 °C), which raises the question if their structural origin is similar as well. Differential scanning calorimetry revealed that two glass transitions exist, whereby the first glass transition differs for both samples at eutectic mixing ratio and the second glass transition is similar for both. To further unreavel the underlying structural features for the concurring difference and similarity, PFG NMR as well as EPR spectroscopy were performed. It could be shown that the excess component in each eutectic sample was the more mobile component. This is in agreement with mean square displacements of MD simulations as well as with rheology data. EPR spectroscopy with different spin probe molecules gave hints on the formation of H-bond networks in the samples. Thereby, it is the anion that plays a key role in bridging the $[EMIm]^+$ with the urea. The ratio between [EMIm][Cl] and urea dictates the extent of this bridging network. For the dystectic 50 : 50 mixture, the urea-rich and $[EMIm]^+$ rich phases are well interconnected. However, for both eutectic mixture samples (25 : 75 and 72.5 : 27.5 [EMIm][Cl] : urea, respectively) nanophase segregation weakens this complex interconnection and the $[EMIm]^+$–Cl^-–urea net-

work (which has the same glass transition temperature for every sample) shrinks. Since the minor component of both eutectic samples is fully interconnected with the anion, it is the excess component that stays mobile and which then dictates the second glass transition temperature and thus is the reason for the macroscopic melting point depression of the mixture.

The second part also highlights a eutectic system: a mixture of choline chloride (2-hydroxyethyl)trimethylammonium chloride) and imidazole. In contrast to Chap. 3, the used organic salt here has a melting point of 302 °C and therefore is no ionic liquid by definition. However, upon addition of imidazole in a mixing ratio of 3 : 7 ChCl : Im, the melting point gets depressed to 56 °C, *i.e.* into the regime of ionic liquids. Since this mixture is highly hygroscopic, an industrial use of this system cannot be achieved without water impurities. Therefore, the influence of small water contents on the physicochemical properties were investigated. It has been found that there are some properties where water has a strong effect on (viscosity, density, water uptake) and some properties that are less affected by small water contents (pH value, refractive index). Interestingly, the density measurements showed a very strong increase of density upon addition of small water contents, exceeding the densities for pure 3 : 7 ChCl : Im mixture and for pure water. Hence, ss NMR, liquid NMR as well as EPR spectroscopy were performed to explain this unusual water uptake mechanism. Solid state NMR revealed that there must be a spatial separation of choline-rich phase and imidazole-rich phase and also that choline is the more mobile component. Liquid state NMR at 60 °C showed that the chemical shifts of the choline cation peaks vary extremely with added water. Hence, it can be assumed that added water is incorporated into the choline-rich phase. In order for the density to increase above the density value for the pure components, the water must fill out exisiting voids in the choline-richt phase. Analog to the findings in Chap. 3, the chloride anion might act as a bridging agent between the two phases, which would leave the choline-rich phase depleted with the anions. A consequence would be Coulomb repulsion between the choline cations which could cause the voids which explains the higher mobility of the choline ions. With this evaluated water uptake mechanism, the changes in physicochemical properties can be explained, where the viscosity and density is dictated by the pseudo-fluid

choline–water-phase and the pH value and refractive index is determined by the preservation of the imidazole lattice.

The third topic features a mixture of three different 1-alkyl-3-methyl-imidazolium tetrafluoroborates with two different buffer solutions as solvent for the intrinsically disordered protein MBP. MBP is known for only showing strong tertiary protein structures in the presence of biomembranes. In the course of this experiment, it is investigated if the molecular ordering and transient structures which are typically present in ionic liquid solutions can act as an "artificial membrane" in the MBP's point of view. In order to gain information on the sample structure and structural changes upon varying measurement conditions, dynamic light scattering was chosen as tracking method. Overall, 76 samples were prepared, thereby three different ionic liquids were used: [EMIm][BF_4], [BMIm][BF_4], and [HMIm][BF_4]; each in different amounts: 0, 10, 25, 50, and 100 % $v : v$, mixed with two different buffer solutions: phosphate and HEPES buffer and with different added concentrations of MBP: 0, 2, 5 and 10 µM. The effect of each factor on the sample particle size was discussed and it could be shown that the choice of ionic liquid – their alkyl chain length, respectively – has the biggest and most meaningful impact on the MBP structure. The 50 : 50 mixture of [BMIm][BF_4] in buffer showed small and defined particles of sizes around 3–5 nm with high autocorrelation. This is the typical size regime of small micellar structures which indeed could form considering the polar imidazolium "head group" and the non-polar butyl chain. The myelin basic protein in buffer forms very large aggregates of 100–1000 nm. In the presence of the 50 : 50 [BMIm][BF_4]–buffer mixture, DLS measurements show no aggregates at all. It can be assumed that the [BMIm][BF_4] structures either dissolve the aggregates or even act as a viable binding site so that single MBP molecules can be incorporated. Interestingly, [HMIm][BF_4] shows a similar effect while not featuring intrinsic structures observed by DLS measurements. However, the particle sizes of [HMIm][BF_4] structures are $\sim$ 100 nm, too large for micelles but fitting for vesicular structures. Again, in the presence of [HMIm][BF_4], dynamic light scattering shows no MBP aggregates anymore. It is still not clear how the transient ionic liquid structures look like exactly, thus, extended studies with *e.g.* small angle X-ray scattering

or neutron scattering should be performed. Since MBP leakage out of the myelin sheath of neuronal cells is a main etiological cause or symptom of multiple sclerosis patients, the knowledge of artificial membrane mimics enforcing MBP tertiary structures might be beneficial for MS research.

Figure 6.1 summarizes the three investigated topics and their different measurement methods and results.

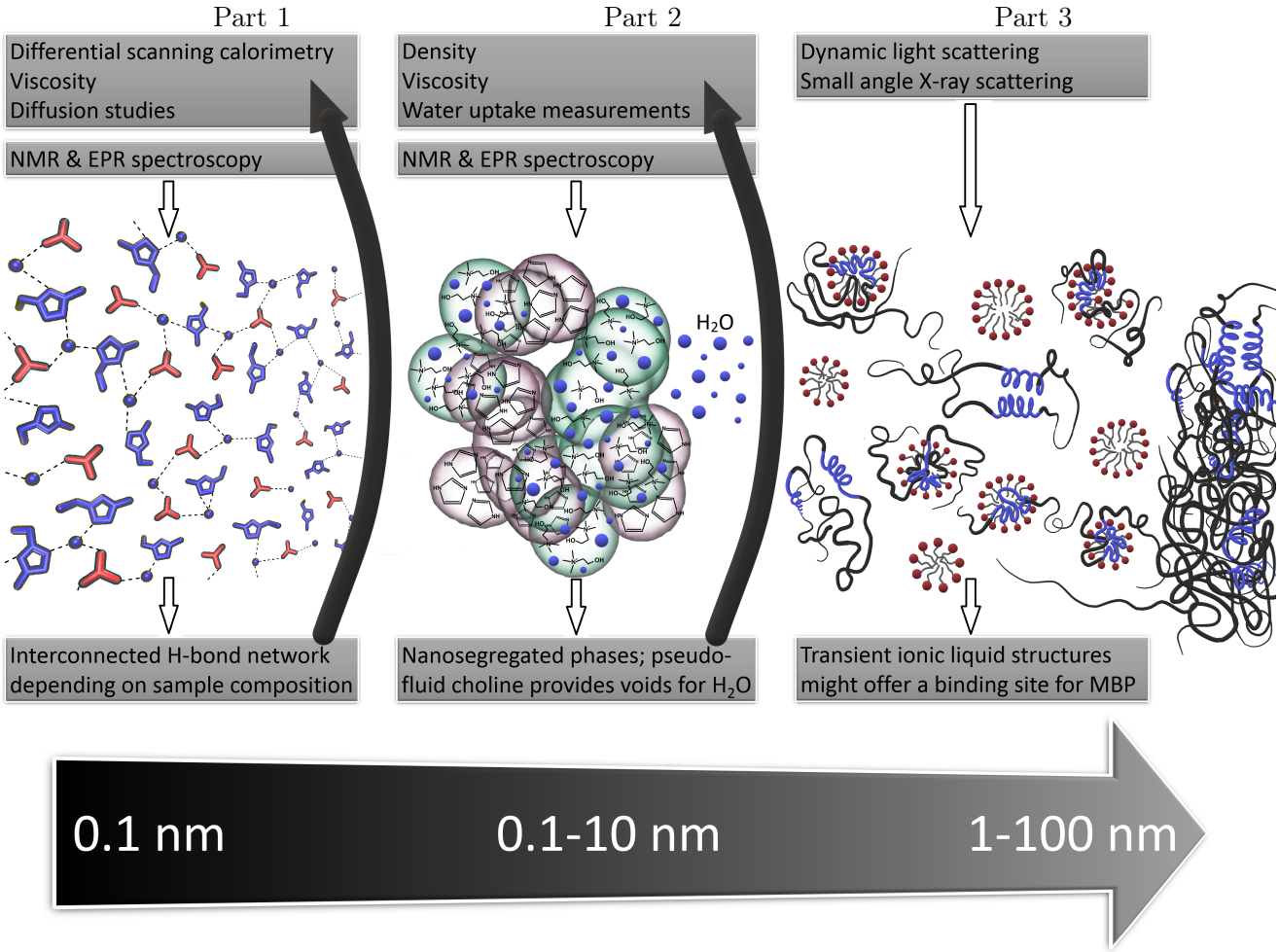

Figure 6.1: Summarizing visualization of the three investigated topics.

It could be proven that by means of physicochemical property measurements combined with spectroscopic data, a microscopic image of the sample's molecular structure can be built. This image is the very basis for the explanation of the actual origin of the unique physicochemical properties of every system (big arrows in Fig. 6.1 for Part 1 and Part 2). It again shows the power of spectroscopy and the so obtained structural information on the nanoscale for the investigation of macroscopic phenomena. In order to confirm these findings, further methods that provide structural information should be performed and used as comparison: *e.g.* X-ray diffraction, neutron scattering, or fluorescence/atomic force microscopy. The investigated water uptake mechanism in Chap. 4 revealed molecular voids that were assumed to originate from anion depletion and thus, COULOMB repulsion between the cations. This effect could play an important role for gas storage, especially for greenhouse gases such as CO_2 where ionic liquids have been discovered to be a viable storage medium[12,57].

For the third research topic in this study, extended small and wide-angle high-energy X-ray scattering methods could be useful to characterize the [BMIm][BF_4]-, [HMIm][BF_4]-, and MBP structures and their interaction mechanics. Since ionic liquids have been proven to be a unique solvent for proteins regarding structure enforcement or disaggregation, a possible protein separation, filtration and purification could be possible when chosing the best fitting ionic liquid. The next step would be to use fully biodegradable and physiological valid ionic liquids for *in vitro* research. Until now there has not been a published synthetization of ionic liquids where both, anion and cation, consist of biogenic ions based on *e.g.* amino acids or lactates. This would make the unique properties of ionic liquids accessible in biology and pharmacy as well, for the development of new pharmaceutical ingredients, cosmetics, harmless antimicrobials or for (*in vivo*) diseases research with proteins, enzymes and DNA.

Ionic liquids and ionic liquid-like systems possess very unique properties which are caused by a very sensitive balance of H-bonding, COULOMB attraction and repulsion, spatial separation, and the hydrophobic effect through their non-polar side chains. There are countless combinations of ions, especially considering the additional possibility to create deep-eutectic

mixtures. Once the perfect ion match is found, ionic liquids have been proven to be superior to commonly used liquids in many fields of application. In order to find easy and cost-efficient solutions for the increasing global warming and atmospheric greenhouse gases, new viable ionic liquids have to be discovered, and already known ionic liquid systems have to be refined and investigated.

7 References

[1] U. Cerajewski, J. Träger, S. Henkel, A. H. Roos, M. Brehm, and D. Hinderberger. Nanoscopic structures and molecular interactions leading to a dystectic and two eutectic points in [EMIm][Cl]/urea mixtures. *Phys. Chem. Chem. Phys.*, 20:29591–29600, 2018. doi: 10.1039/C8CP04912B. URL `http://dx.doi.org/10.1039/C8CP04912B`.

[2] B. Bereiter, S. Eggleston, J. Schmitt, C. Nehrbass-Ahles, T. F. Stocker, H. Fischer, S. Kipfstuhl, and J. Chappellaz. Revision of the Epica Dome C CO_2 record from 800 to 600 kyr before present. *Geophys. Res. Lett.*, 42(2):542–549, 2015. doi: 10.1002/2014GL061957. URL `https://agupubs.onlinelibrary.wiley.com/doi/abs/10.1002/2014GL061957`.

[3] C. P. Morice, J. J. Kennedy, N. A. Rayner, and P. D. Jones. Quantifying uncertainties in global and regional temperature change using an ensemble of observational estimates: The Hadcrut4 data set. *J. Geophys. Res. Atmos.*, 117(D8), 2012. doi: 10.1029/2011JD017187. URL `https://agupubs.onlinelibrary.wiley.com/doi/abs/10.1029/2011JD017187`.

[4] P. Tans and R. Keeling. Mauna Loa CO_2 monthly mean data. Website, 2020. published online at `https://www.esrl.noaa.gov/gmd/ccgg/trends/data.html`.

[5] E. Dlugokencky. Globally averaged marine surface monthly mean data. Website, 2019. published online at `https://www.esrl.noaa.gov/gmd/ccgg/trends_ch4/`.

[6] B. Metz, L. Kuijpers, S. Solomon, S. O. Andersen, O. Davidson, J. Pons, D. de Jager, T. Kestin, M. Manning, and L. Meyer. *International Panel on Climate Change: Safe-*

guarding the Ozone Layer and the Global Climate System. Cambridge University Press, The Edinburgh Building Shaftesbury Road, Cambridge, England, 2005.

[7] European Environment Agency. National emissions reported to the convention on long-range transboundary air pollution (lrtap convention). Website, 2013. published online at https://www.eea.europa.eu/data-and-maps/data/national-emissions-reported-to-the-convention-on-long-range-transboundary-air-pollution-lrtap-convention-7.

[8] J. S. Wilkes and M. J. Zaworotko. Air and water stable 1-ethyl-3-methylimidazolium based ionic liquids. *J. Chem. Soc. Chem. Commun.*, pages 965–967, 1992. doi: 10.1039/C39920000965.

[9] B. C. Ranu and S. Banerjee. Ionic liquid as catalyst and reaction medium. the dramatic influence of a task-specific ionic liquid, [bmim]oh, in michael addition of active methylene compounds to conjugated ketones, carboxylic esters, and nitriles. *Org. Lett.*, 7(14):3049–3052, Jul 2005. doi: 10.1021/ol051004h. URL `http://dx.doi.org/10.1021/ol051004h`.

[10] BASF. BASIL™ – the first commercial process using ionic liquids. published online at `http://www.basf.com/group/corporate/de_DE/innovations/publications/innovation-award/2004/basil`.

[11] P. Navia, J. Troncoso, and L. Romaní. Excess magnitudes for ionic liquid binary mixtures with a common ion. *J. Chem. Eng. Data*, 52(4):1369–1374, 2007. doi: 10.1021/je700076t.

[12] L. A. Blanchard, D. Hancu, E. J. Beckman, and J. F. Brennecke. Green processing using ionic liquids and co_2. *Nature*, 399:28–29, 05 1999. doi: 10.1038/19887. URL `https://doi.org/10.1038/19887`.

[13] H. Lin, P. Bai, and X. Guo. Ionic liquids for SO_2 capture: Development and progress. *Asian J. Chem.*, 26(9):2501–2506, 2014. doi: 10.14233/ajchem.2014.15800.

[14] A. H. M. Fauzi and N. A. S. Amin. An overview of ionic liquids as solvents in biodiesel synthesis. *Renew. Sust. Energy Rev.*, 16(8):5770–5786, 2012. doi: 10.1016/j.rser.2012.06.022. URL `https://doi.org/10.1016/j.rser.2012.06.022`.

[15] A. P. Abbott, G. Capper, D. L. Davies, R. K. Rasheed, and V. Tambyrajah. Novel solvent properties of choline chloride/urea mixtures. *Chem. Commun.*, pages 70–71, 2003. doi: 10.1039/B210714G. URL `http://dx.doi.org/10.1039/B210714G`.

[16] E. J. Arroyo and S. S. Scherer. On the molecular architecture of myelinated fibers. *Histochem. Cell Biol.*, 113:1–18, 2000. doi: 10.1007/s004180050001. URL `http://dx.doi.org/10.1007/s004180050001`.

[17] Z. Fountas. Spiking neural networks for human-like avatar control in a simulated environment. Master's thesis, mperial College London, Department of Computing, South Kensington Campus, London, UK, 9 2011.

[18] K. A. Vassall, K. Bessonov, M. De Avila, E. Polverini, and G. Harauz. The effects of threonine phosphorylation on the stability and dynamics of the central molecular switch region of 18.5-kda myelin basic protein. *PLOS ONE*, 8(7):1–19, 07 2013. doi: 10.1371/journal.pone.0068175. URL `https://doi.org/10.1371/journal.pone.0068175`.

[19] K. A. Vassall, A. D. Jenkins, V. V. Bamm, and G. Harauz. Thermodynamic analysis of the disorder-to-α-helical transition of 18.5-kda myelin basic protein reveals an equilibrium intermediate representing the most compact conformation. *J. Mol. Biol.*, 427:1977–1992, 2015. doi: 10.1016/j.jmb.2015.03.011. URL `http://dx.doi.org/10.1016/j.jmb.2015.03.011`.

[20] D. R. Kattnig, T. Bund, J. M. Boggs, G. Harauz, and D. Hinderberger. Lateral self--assembly of 18.5-kda myelin basic protein (mbp) charge component-c1 on membranes. *Biochim. Biophys. Acta – Biomembranes*, 1818(11):2636–2647, 2012. doi: 10.1016/j.bbamem.2012.06.010. URL `https://doi.org/10.1016/j.bbamem.2012.06.010`.

[21] H. Lassmann. Mechanisms of white matter damage in multiple sclerosis. *Glia*, 62(11): 1816–1830, 2014. doi: 10.1002/glia.22597. URL `https://onlinelibrary.wiley.com/doi/abs/10.1002/glia.22597`.

[22] T. Tsuda, T. Tomioka, and C. L. Hussey. Physicochemical properties of highly conductive urea–EtMeImCl melts. *Chem. Commun.*, pages 2908–2910, Apr 2008. doi: 10.1039/b802386g. URL `http://dx.doi.org/10.1039/b802386g`.

[23] A. Das, S. Das, and R. Biswas. Density relaxation and particle motion characteristics in a non-ionic deep eutectic solvent (acetamide + urea): Time-resolved fluorescence measurements and all-atom molecular dynamics simulations. *J. Chem. Phys.*, 142:034505, 2015. doi: 10.1063/1.4906119. URL `http://dx.doi.org/10.1063/1.4906119`.

[24] Y. Akdogan, J. Heller, H. Zimmermann, and D. Hinderberger. The solvation of nitroxide radicals in ionic liquids studied by high-field EPR spectroscopy. *Phys. Chem. Chem. Phys.*, 12:7874–7882, 2010. doi: 10.1039/c001602k.

[25] T. L. Greaves, D. F. Kennedy, S. T. Mudie, and C. J. Drummond. Diversity observed in the nanostructure of protic ionic liquids. *J. Phys. Chem. B*, 114:10022–10031, 2010.

[26] S. S. Hossain and A. Samanta. Solute rotation and translation dynamics in an ionic deep eutectic solvent based on choline chloride. *J. Phys. Chem. B*, 121:10556–10565, 2017. doi: 10.1021/acs.jpcb.7b08472. URL `http://dx.doi.org/10.1021/acs.jpcb.7b08472`.

[27] R. G. Evans, A. J. Wain, C. Hardacre, and R. G. Compton. An electrochemical and ESR spectroscopic study on the molecular dynamics of tempo in room temperature ionic liquid solvents. *ChemPhysChem*, 6:1035–1039, 2005. doi: 10.1002/cphc.200500157.

[28] V. Strehmel, A. Laschewski, R. Stoesser, A. Zehl, and W. Herrmann. Mobility of spin probes in ionic liquids. *J. Phys. Org. Chem.*, 19:318–325, 2006. doi: 10.1002/poc.1072.

[29] N. M. Atherton. *Principles of Electron Spin Resonance*. Number ISBN 0-137-21762-5. Ellis Horwood PTR Prentice Hall, 1993.

[30] S. Stoll and A. Schweiger. Easyspin, a comprehensive software package for spectral simulation and analysis in EPR. *J. Magn. Reson.*, 178:42–55, 2006.

[31] Sandia National Laboratories. *LAMMPS Users Manual*, 24 Jan 2013 version, 2013. 24 Jan 2013 version.

[32] J. N. Canongia Lopes and A. A. H. Pádua. Molecular force field for ionic liquids composed of triflate or bistriflylimide anions. *J. Phys. Chem. B*, 108(43):16893–16898, 2004. doi: 10.1021/jp0476545.

[33] W. L. Jorgensen, D. S. Maxwell, and J. Tirado-Rives. Development and testing of the OPLS all-atom force field on conformational energetics and properties of organic liquids. *J. Am. Chem. Soc.*, 118(45):11225–11236, 1996. doi: 10.1021/ja9621760. URL `http://dx.doi.org/10.1021/ja9621760`.

[34] S. Nosé. A unified formulation of the constant temperature molecular dynamics methods. *J. Chem. Phys.*, 81:511–519, 1984. doi: 10.1063/1.447334.

[35] M. Brehm and B. Kirchner. TRAVIS – a free analyzer and visualizer for Monte Carlo and Molecular Dynamics trajectories. *J. Chem. Inf. Model.*, 51:2007–2013, 2011.

[36] C. D'Agostino, L. F. Gladden, M. D. Mantle, A. P. Abbott, E. I. Ahmed, A. Y. M. Al-Murshedi, and R. C. Harris. Molecular and ionic diffusion in aqueous deep eutectic solvent mixtures: probing inter-molecular interactions using PFG NMR. *Phys. Chem. Chem. Phys.*, 17:15297–15304, 2015. doi: 10.1039/c5cp01493. URL `http://dx.doi.org/10.1039/c5cp01493`.

[37] A. Efimova, L. Pfützner, and P. Schmidt. Thermal stability and decomposition mechanism of 1-ethyl-3-methylimidazolium halides. *Thermochim. Acta*, 604:129–136, 2015. doi: 10.1016/j.tca.2015.02.001. URL `https://doi.org/10.1016/j.tca.2015.02.001`.

[38] A. van den Bruinhorst, S. Theodora, J.-R. Hill, and M. C. Kroon. Experimental and molecular modeling evaluation of the physicochemical properties of proline-based deep

eutectic solvents. *J. Phys. Chem. B*, 122:369–379, 2018. doi: 10.1021/acs.jpcb.7b09540. URL http://dx.doi.org/10.1021/acs.jpcb.7b09540.

[39] Y. Hou, G. Yinngying, S. Zhang, F. Yang, H. Ding, and Y. Shan. Novel binary eutectic mixtures based on imidazole. *J. Mol. Liq.*, 143:154–159, 2008. doi: 10.1016/j.molliq.2008.07.009. URL http://dx.doi.org/10.1016/j.molliq.2008.07.009.

[40] K. Hayamizu, Y. Aihara, H. Nakagawa, T. Nukuda, and W. S. Price. Ionic conduction and ion diffusion in binary room-temperature ionic liquids composed of [EMIM][BF_4] and $LiBF_4$. *J. Phys. Chem. B*, 108:19527–19532, 2004. doi: 10.1021/jp0476601. URL http://dx.doi.org/10.1021/jp0476601.

[41] D. V. Wagle, G. A. Baker, and E. Mamontov. Differential microscopic mobility of components within a deep eutectic solvent. *J. Phys. Chem. Lett.*, 6:2924–2928, 2015. doi: 10.1021/acs.jpclett.5b01192. URL http://dx.doi.org/10.1021/acs.jpclett.5b01192.

[42] A. Faraone, D. V. Wagle, G. A. Baker, E. C. Novak, M. Ohl, D. Reuter, P. Lunkenheimer, A. Loidl, and E. Mamontov. Glycerol hydrogen-bonding network dominates structure and collective dynamics in a deep eutectic solvent. *J. Phys. Chem. B*, 122:1261–1267, 2018. doi: 10.1021/acs.jpcb.7b11224. URL http://dx.doi.org/10.1021/acs.jpcb.7b11224.

[43] J. N. A. Canongia Lopes and A. A. H. Pádua. Nanostructural organization in ionic liquids. *J. Phys. Chem. B*, 110(7):3330–3335, 2006. doi: 10.1021/jp056006y. URL https://doi.org/10.1021/jp056006y.

[44] D. Kurzbach, M. J. N. Junk, and D. Hinderberger. Nanoscale inhomogeneities in thermoresponsive polymers. *Macromol. Rapid Commun.*, 34(2):119–134, 2013. doi: 10.1002/marc.201200617. URL https://onlinelibrary.wiley.com/doi/abs/10.1002/marc.201200617.

[45] J. Dupont. On the solid, liquid and solution structural organization of imidazolium ionic liquids. *J. Brazil. Chem. Soc.*, 15:341–350, 2004. doi: 10.1590/S0103-50532004000300002. URL http://doi.org/10.1590/S0103-50532004000300002.

[46] M. Deetlefs, C. Hardacre, M. Nieuwenhuyzen, A. A. H. Padua, O. Sheppard, and A. K. Soper. Liquid structure of the ionic liquid 1,3-dimethylimidazolium bis(trifluoromethyl)-sulfonylamide. *J. Phys. Chem. B*, 110(24):12055–12061, 2006. doi: 10.1021/jp060924u. URL `http://doi.org/10.1021/jp060924u`.

[47] C. Hardacre, J. D. Holbrey, S. E. J. McMath, D. T. Bowron, and A. K. Soper. Structure of molten 1,3-dimethylimidazolium chloride using neutron diffraction. *J. Chem. Phys.*, 118 (1):273–278, 2003. doi: 10.1063/1.1523917. URL `http://doi.org/10.1063/1.1523917`.

[48] C. G. Hanke, S. L. Price, and R. M. Lynden-Bell. Intermolecular potentials for simulations of liquid imidazolium salts. *Mol. Phys.*, 99(10):801–809, 2001. doi: 10.1080/00268970010018981. URL `http://doi.org/10.1080/00268970010018981`.

[49] Y. Chen, D. Yu, W. Chen, L. Fu, and T. Mu. Water absorption by deep eutectic solvents. *Phys. Chem. Chem. Phys.*, 21:2601–2610, 2019. doi: 10.1039/C8CP07383J. URL `http://dx.doi.org/10.1039/C8CP07383J`.

[50] M. Temkin and V. Pyzhev. Kinetics of ammonia synthesis on promoted iron catalysts. *Acta Physicochim. URSS*, 12:217–222, 1940.

[51] X. Meng, K. Ballerat-Busserolles, P. Husson, and J.-M. Andanson. Impact of water on the melting temperature of urea + choline chloride deep eutectic solvent. *New J. Chem.*, 40:4492–4499, 2016. doi: 10.1039/C5NJ02677F. URL `http://dx.doi.org/10.1039/C5NJ02677F`.

[52] J. Stetefeld, S. A. McKenna, and T. R. Patel. Dynamic light scattering: a practical guide and applications in biomedical sciences. *Biophys. Rev.*, pages 409–427, Oct 2016. doi: 10.1007/s12551-016-0218-6. URL `http://dx.doi.org/10.1007/s12551-016-0218-6`.

[53] J. Vollmer and D. Hinderberger. DLS measurements with refined solvent and measurement parameters of the system [BMIM][BF_4]/water/MBP. not published yet, 2020.

[54] Y. Zheng, Y.-Z. Zhou, G. Deng, R. Guo, and D.-F. Chen. A combination of FTIR and DFT to study the microscopic structure and hydrogen-bonding interaction properties of

the [BMIM][BF_4] and water. *Spectrochim. Acta Part A: Mol. Biomol. Spectrosc.*, 226: 117624, 2020. doi: 10.1016/j.saa.2019.117624. URL `https://doi.org/10.1016/j.saa.2019.117624`.

[55] S. Cha, M. Ao, W. Sung, B. Moon, B. Ahlström, P. Johansson, Y. Ouchi, and D. Kim. Structures of ionic liquid–water mixtures investigated by IR and NMR spectroscopy. *Phys. Chem. Chem. Phys.*, 16:9591–9601, 2014. doi: 10.1039/C4CP00589A. URL `http://dx.doi.org/10.1039/C4CP00589A`.

[56] Q. Shao. On the influence of hydrated imidazolium-based ionic liquid on protein structure stability: A molecular dynamics simulation study. *J. Chem. Phys.*, 139(11):115102, 2013. doi: 10.1063/1.4821588. URL `https://doi.org/10.1063/1.4821588`.

[57] D. Camper, J. E. Bara, D. L. Gin, and R. D. Noble. Room-temperature ionic liquid–amine solutions: Tunable solvents for efficient and reversible capture of CO_2. *Ind. Eng. Chem. Res.*, 47(21):8496–8498, 2008. doi: 10.1021/ie801002m.

Appendix

Chapter 1

A1.1 Viscosity data

The rheological measurements were performed with a Physica MCR 301 from Anton Paar with a CP 25-2/TG measurement spindel. The samples were pre-heated to a target temperature of 85° and quickly applied on the rheometer. Due to strong scattering of η values around the glass/phase transition temperatures, a temperature of 85°C was chosen where the DSC results show finished transitions for every investigated sample.

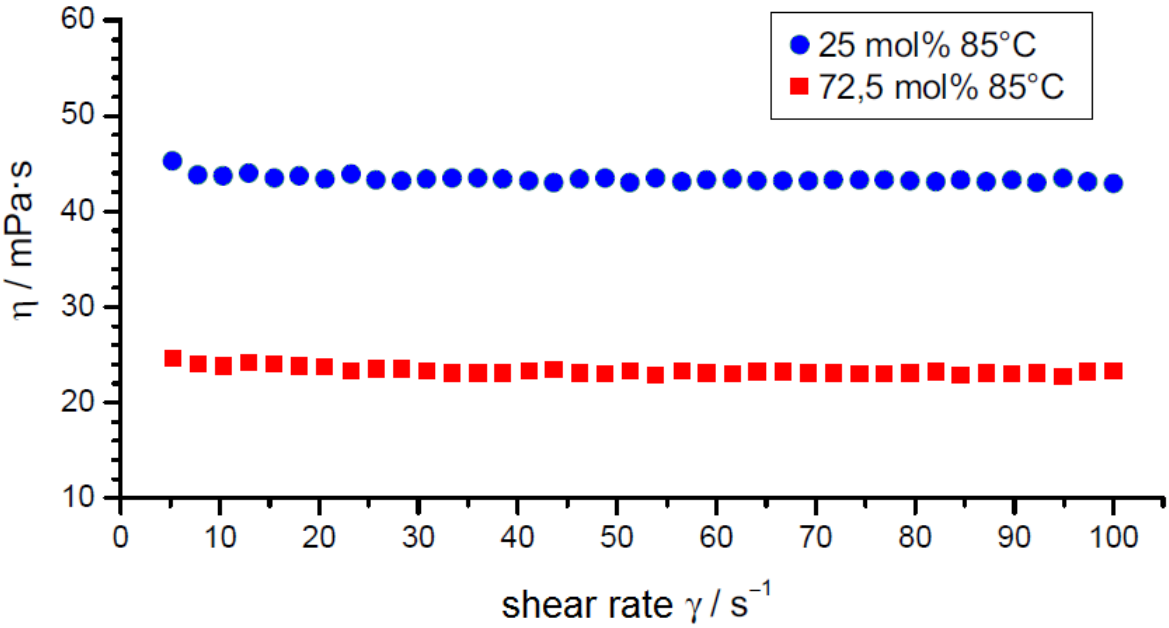

Figure A1: Viscosities for the 25 % and 72.5 % urea samples at 85°C with varying shear rate.

A1.2 Radial distribution function

Radial distribution functions (RDFs) are an expression for the correlation of two particles as a function of distance and can be generated by statistical neighborhood analysis of a reference molecule and subsequent exerpting the nearest particles and their distances. Thus, a pair correlation ($g(r)$) value of 1 means that the probability of the observed particle to be found around the reference particle at the respective distance is equal to its probability at uniform particle density. In Fig. A2 it becomes clear that the hydrogen bonding between the urea NH_2-groups and the chloride is the strongest, their distance is $\sim$ 30 pm less and their pair correlation significantly higher than any of the EMIm ring hydrogen interactions.

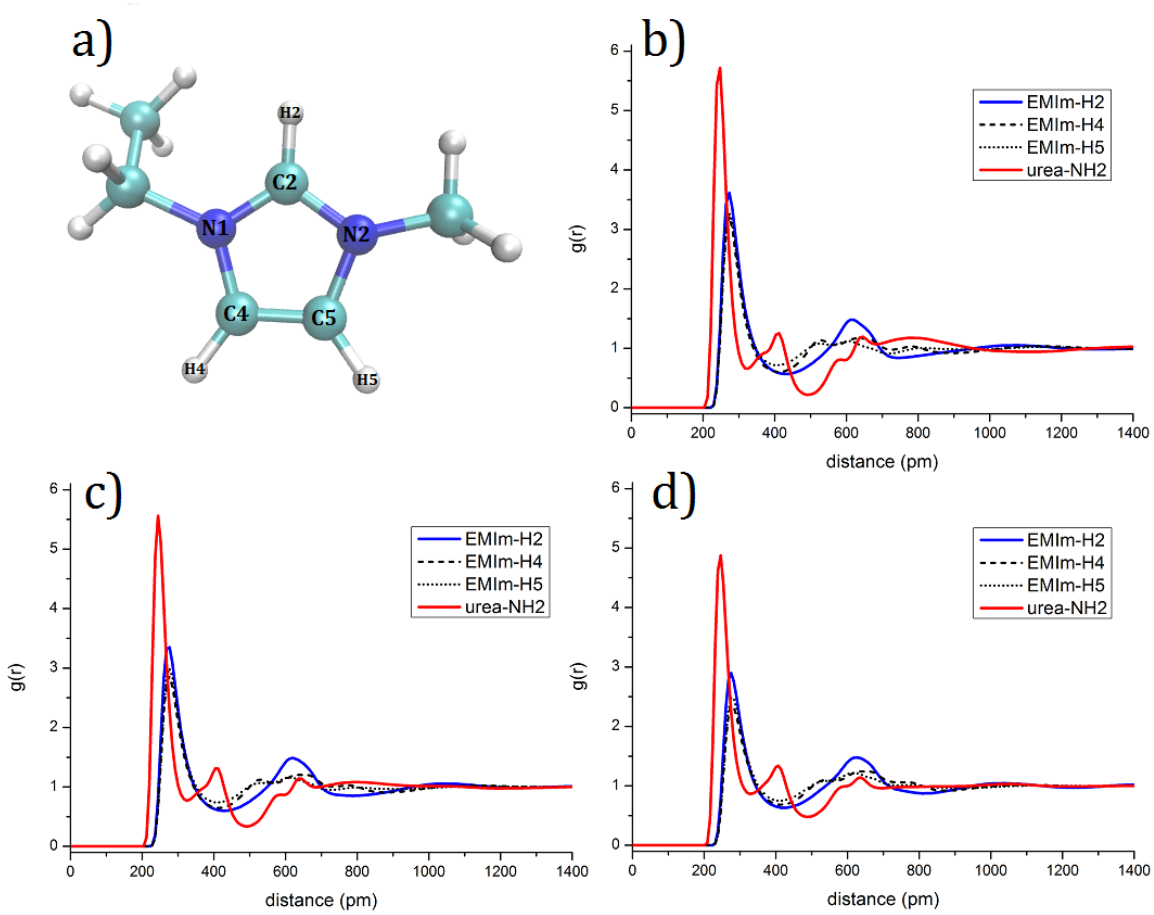

Figure A2: Radial distribution of chloride around selected atoms/group functions (see **a**) of the 25 % **(b)**, 50 % **(c)**, 72.5 % **(d)** urea samples.

A1.3 Frémy's salt spectra

Due to its thermal instability the spin probe disodium nitrosodisulfonate (Frémy's salt) could not be used to perform EPR spectroscopy of the higher melting mixing ratios 12.5, 37.5, 62.5 and 87.5 %. The A'_{zz} progression for the 25 %, 50 % and 72.5 % urea samples are shown in Fig. A3. Note that the axes are scaled to match those of the nitroxide-based spin probes in the main article for better comparison, meaning that the absolute A'_{zz} values (especially for low temperatures) are significantly lower. Given the assumption that Frémy's salt resides in the [EMIm]-rich regions due to its charge, the different curve of the 72.5 % can be explained with the sample's distinct domain-formation.

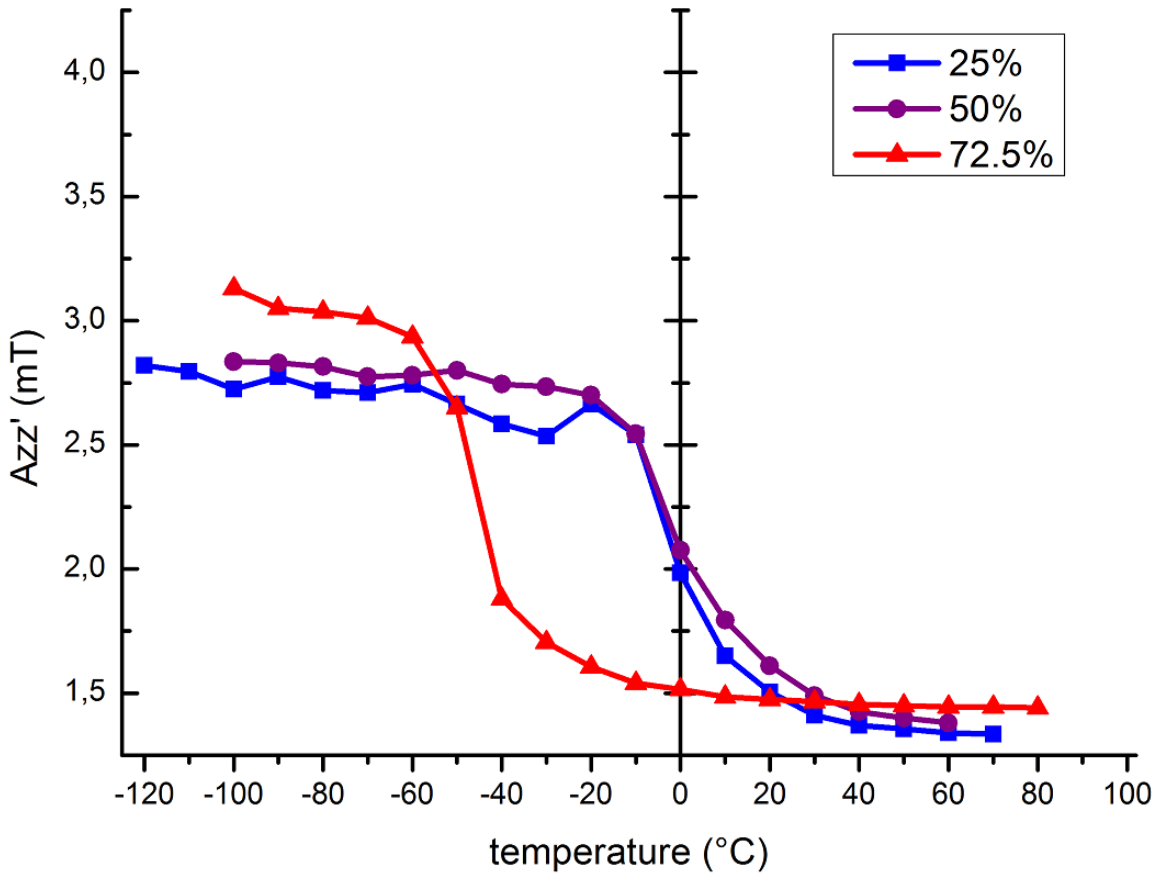

Figure A3: A'_{zz} values of Frémy's salt in all three investigated samples in the temperature range between −100 and +100 °C.

A1.4 TEMPOL spectra in the 62.5 % sample

When investigating the individual CW EPR spectra, TEMPOL in the 62.5 % sample shows an anomaly between −20 and −40°C. Spectra simulation unravels the additional component to the expected rigid limit spectral species, shown in Fig. A4.

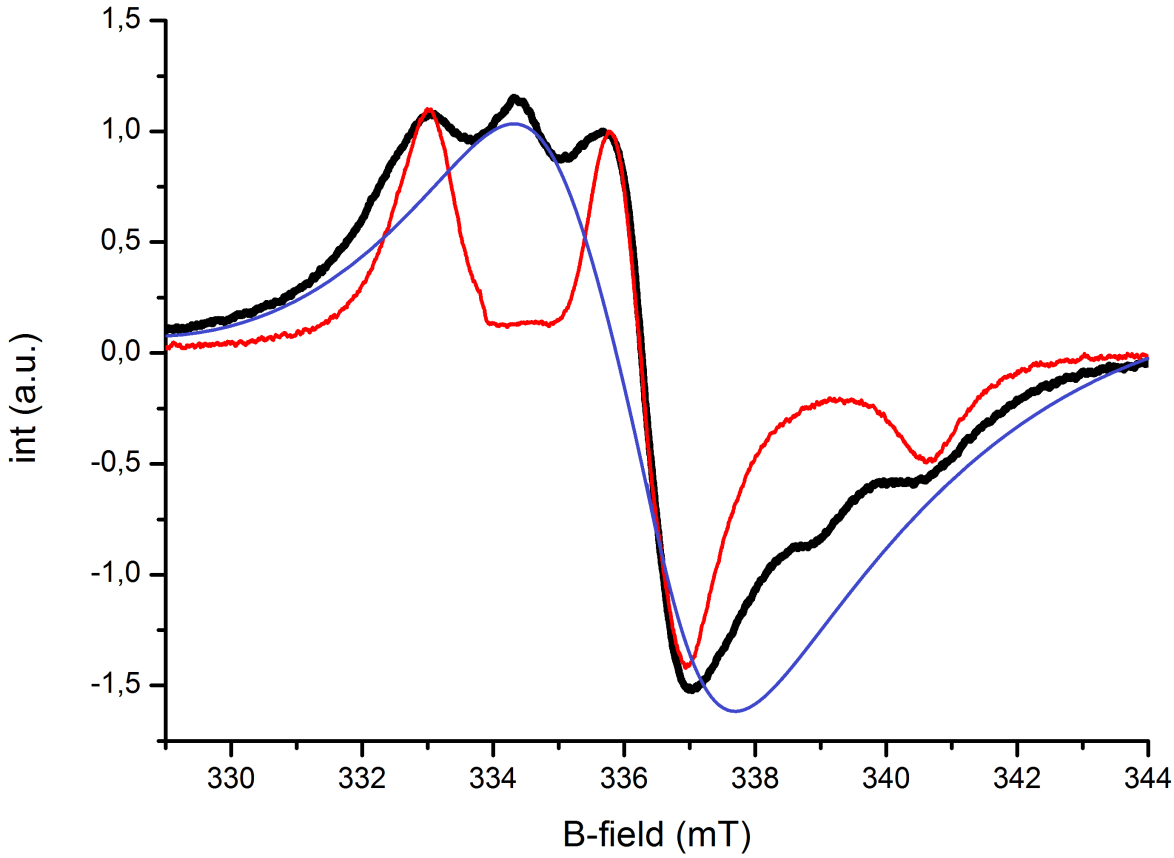

Figure A4: Individual TEMPOL-spectrum in the 62.5 % urea sample at −30° (black, thick). Assumed spectral components are a species at rigid limit (red) and a species featuring spin exchange induced dispersion (blue).

A1.5 Simulated spectra

Selected spectra and their simulations with EasySpin's `chili` function for fast rotation and slow-motion regime, shown exemplarily for TEMPOL in the 25 % urea sample in the respective temperature range.

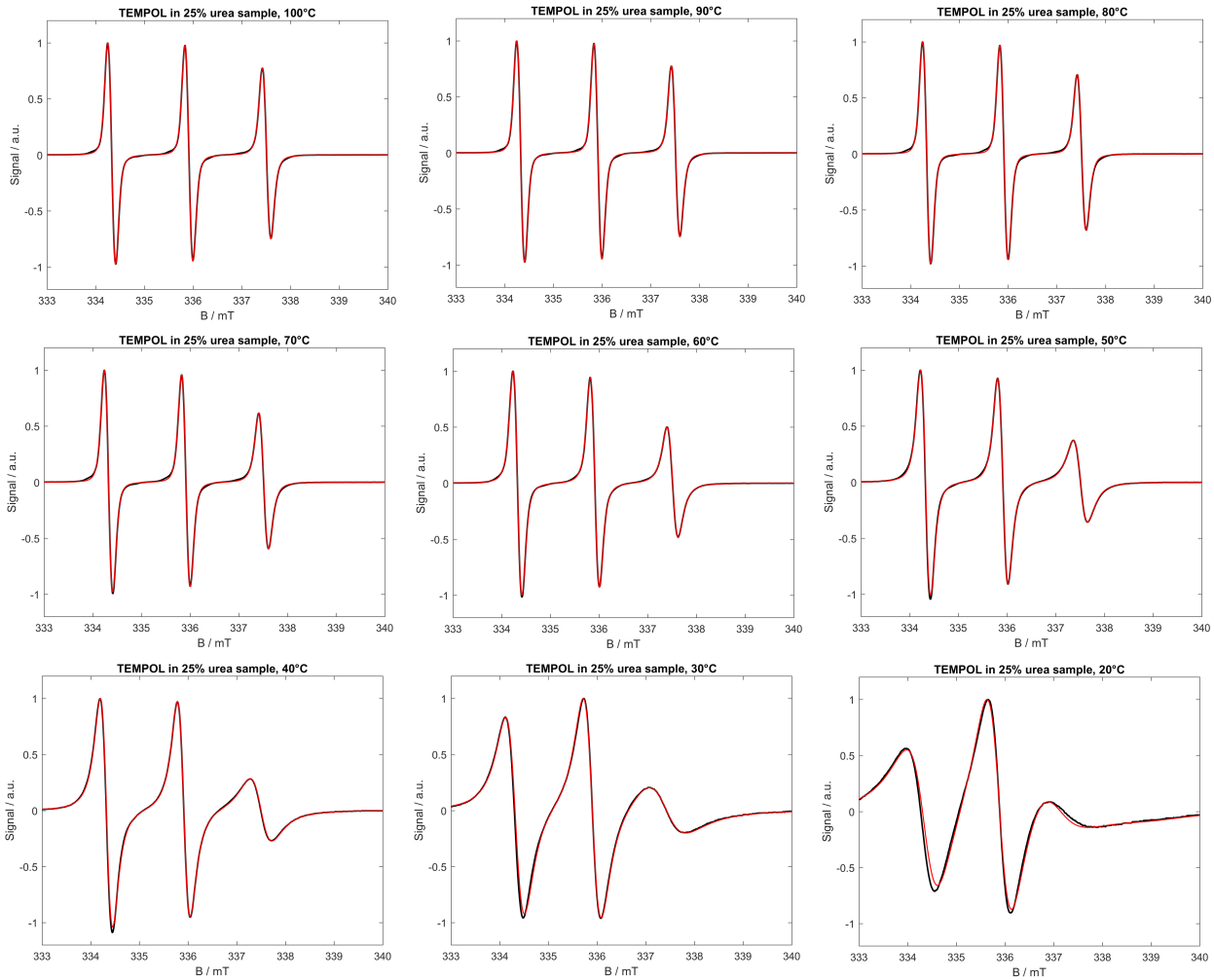

Figure A5: Experimental (black) and simulated (red) individual CW EPR spectra for TEMPOL in the 25 % urea sample at different temperatures.

Chapter 2

A2.1 Long-term water uptake

For this experiment, a 1.29 g sample was placed on a balance with a constant humidity of 55 %. Every few hours/days, the mass increase was tracked until a constant value was reached.

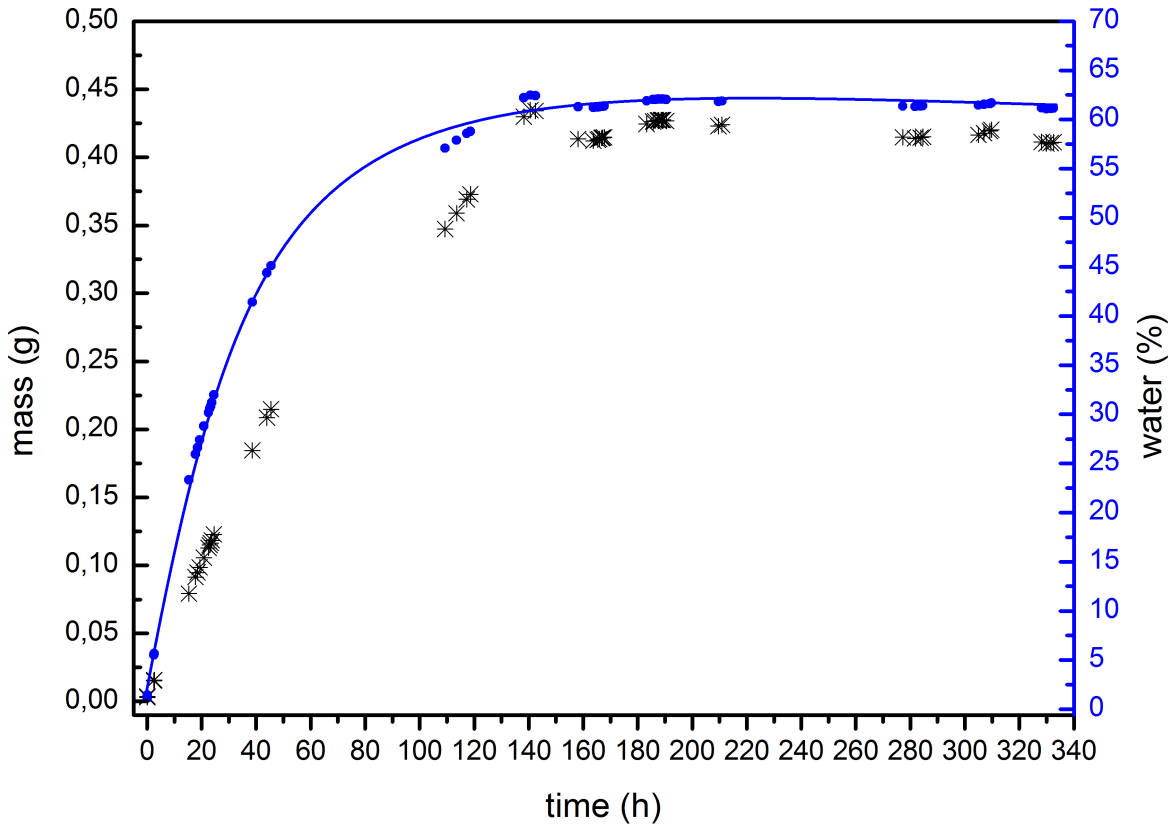

Figure A6: Long-term water uptake measurements. Mass increase data is shown in black crosses and is used to calculate the actual water content, shown in blue.

A2.2 pH values of an aqueous imidazole solution

Imidazole solutions with increasing dilution were prepared and the pH was measured at 25 °C with a pH electrode.

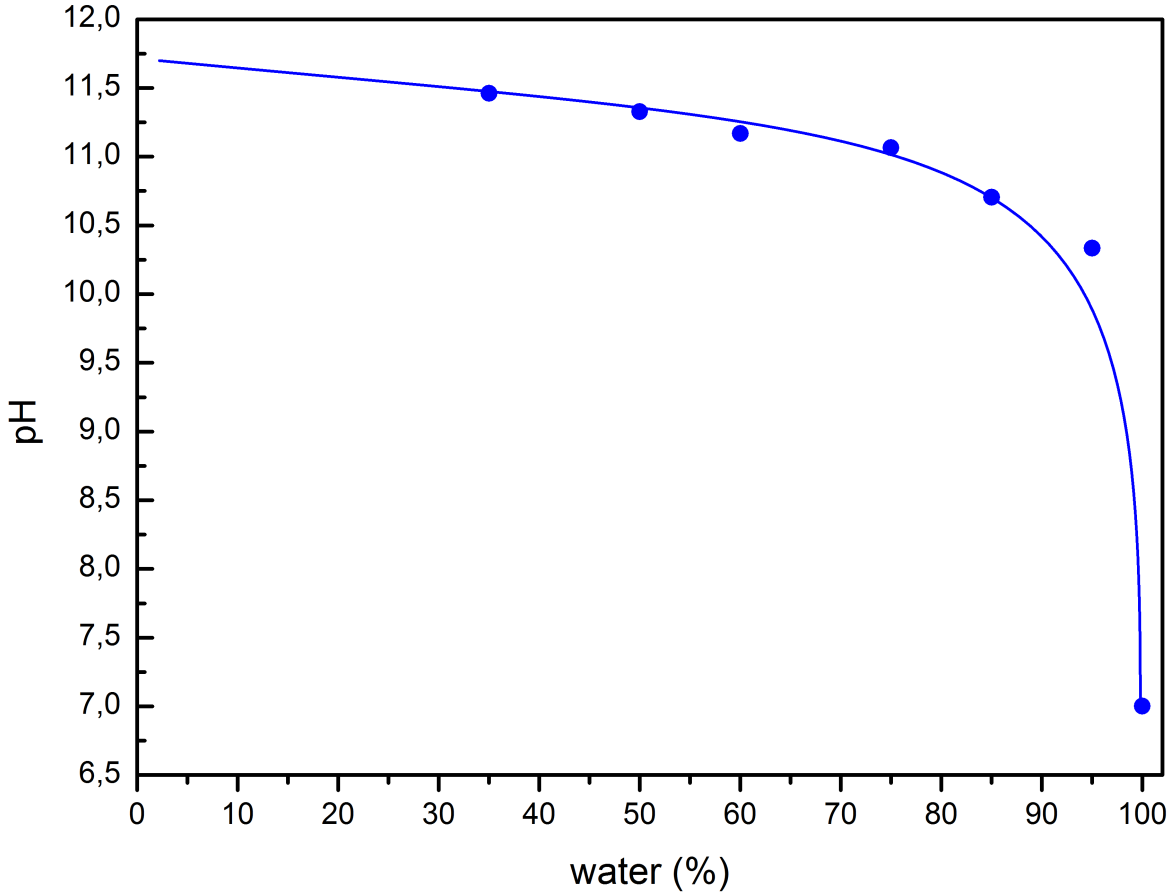

Figure A7: Reference pH measurements of an aqueous imidazole solution.

A2.3 NMR spectra

Liquid state NMR measurements have been performed at 60 °C with an internal coaxial tube containing the deuterated solvent (D_2O) for external D-locking without allowing D–H-exchange and dilution of the sample.

a)

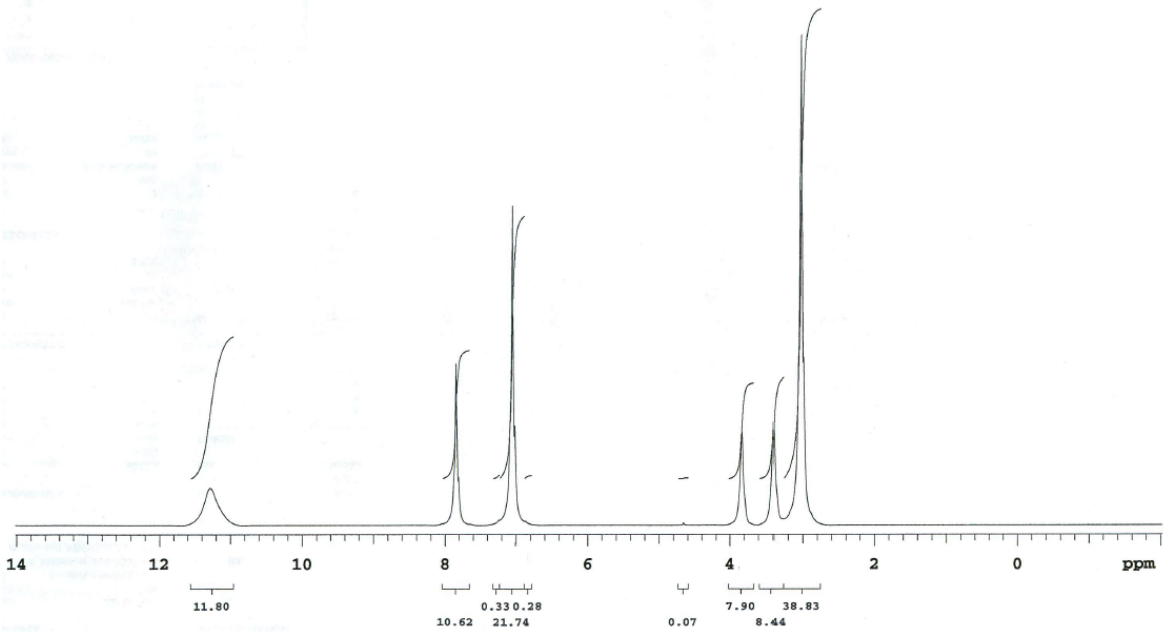

b)

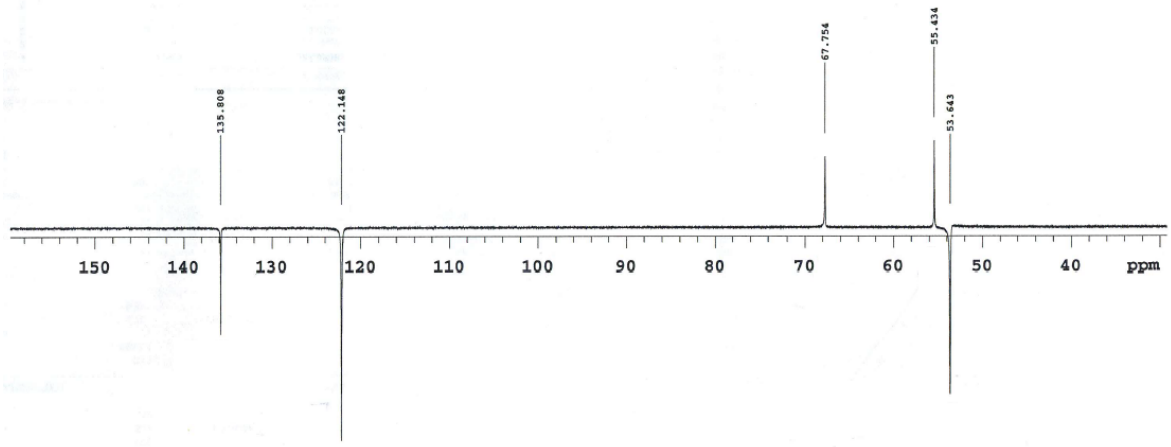

Figure A8: **(a)** ^{1}H NMR spectrum and **(b)** ^{13}C APT NMR spectrum for the sample with 0 % water content.

Table .1: Peak assignment of the sample with 0 % water content.

	peak position	intensity	assignment
^{1}H spectrum	11.28 ppm	8.03	$(CH_3)_3N^+$–CH_2–CH_2–O**H**; –N**H**–CH=N–CH=CH–
	7.85 ppm	34.92	–NH–C**H**=N–CH=CH–
	7.06 ppm	69.35	–NH–CH=N–C**H**=C**H**–
	3.84 ppm	20.13	$(CH_3)_3N^+$–CH_2–C$\mathbf{H_2}$–OH
	3.40 ppm	20.54	$(CH_3)_3N^+$–C$\mathbf{H_2}$–CH_2–OH
	3.03 ppm	106.05	(C$\mathbf{H_3}$)$_3$N$^+$–CH_2–CH_2–OH
^{13}C spectrum	135.82 ppm	−22.89	–NH–**C**H=N–CH=CH–
	122.16 ppm	−45.90	–NH–CH=N–**C**H=**C**H–
	67.76 ppm	15.31	$(CH_3)_3N^+$–**C**H_2–CH_2–OH
	55.44 ppm	18.69	$(CH_3)_3N^+$–CH_2–**C**H_2–OH
	53.65 ppm	−36.05	(**C**H_3)$_3$N$^+$–CH_2–CH_2–OH

Table .2: Peak assignment of the sample with 2 % water content.

	peak position	intensity	assignment
^{1}H spectrum	7.86 ppm	42.60	–NH–C**H**=N–CH=CH–
	7.08 ppm	81.23	–NH–CH=N–C**H**=C**H**–
	3.86 ppm	22.00	$(CH_3)_3N^+$–CH_2–C$\mathbf{H_2}$–OH
	3.42 ppm	22.91	$(CH_3)_3N^+$–C$\mathbf{H_2}$–CH_2–OH
	3.05 ppm	126.81	(C$\mathbf{H_3}$)$_3$N$^+$–CH_2–CH_2–OH
^{13}C spectrum	135.84 ppm	−25.47	–NH–**C**H=N–CH=CH–
	122.18 ppm	−45.90	–NH–CH=N–**C**H=**C**H–
	67.80 ppm	14.82	$(CH_3)_3N^+$–**C**H_2–CH_2–OH
	55.47 ppm	22.59	$(CH_3)_3N^+$–CH_2–**C**H_2–OH
	53.67 ppm	−30.60	(**C**H_3)$_3$N$^+$–CH_2–CH_2–OH

a)

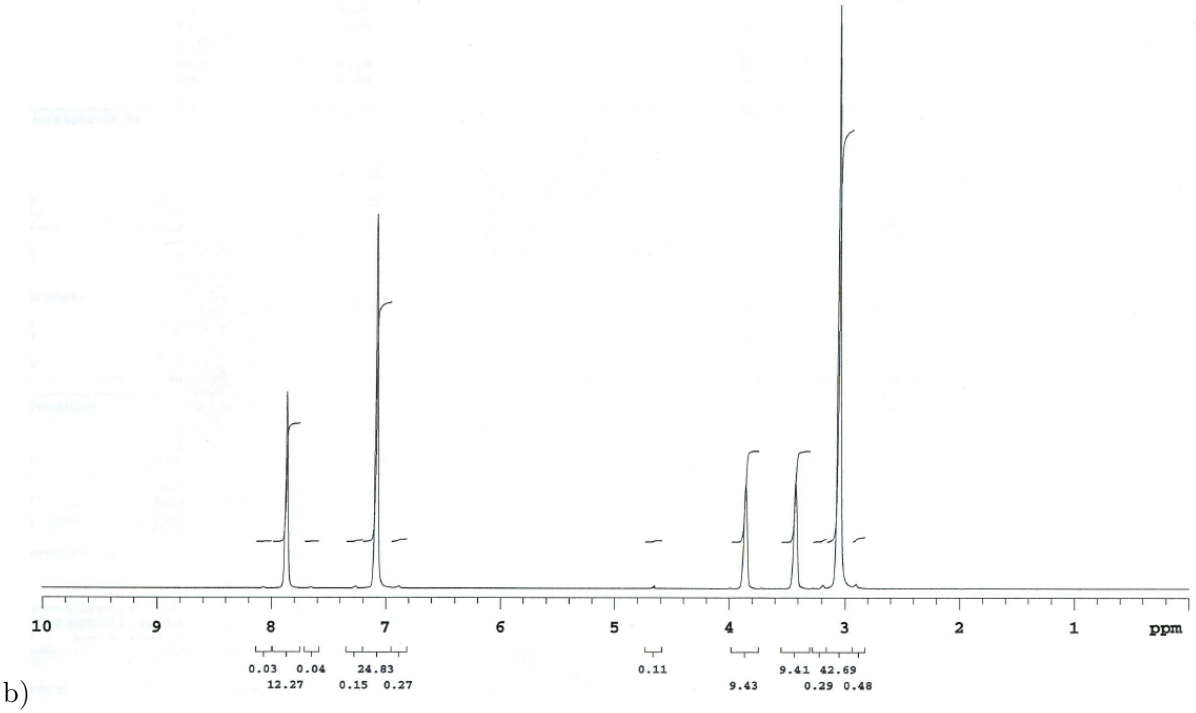

b)

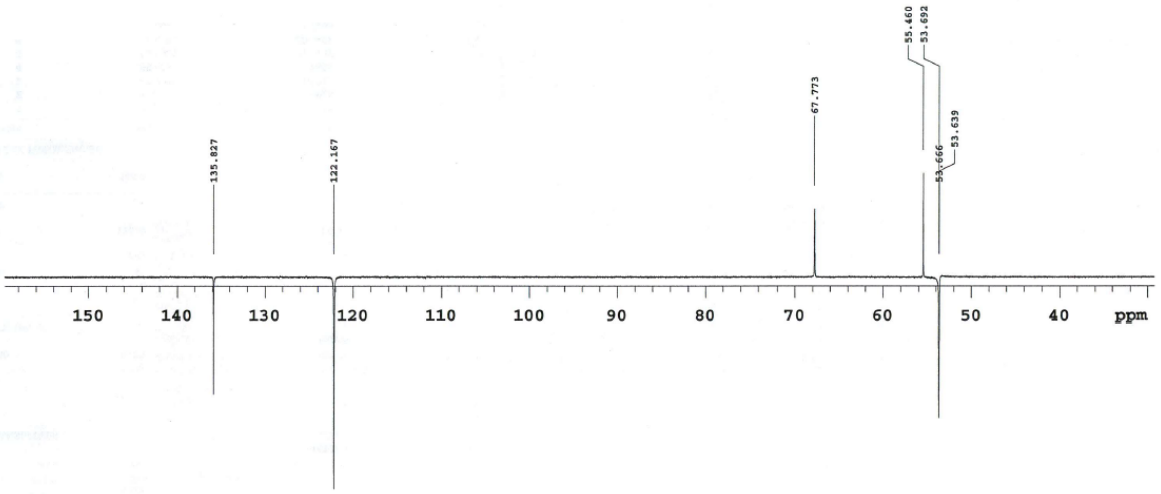

Figure A9: **(a)** ^{1}H NMR spectrum and **(b)** ^{13}C APT NMR spectrum for the sample with 2.01 % water content.

a)

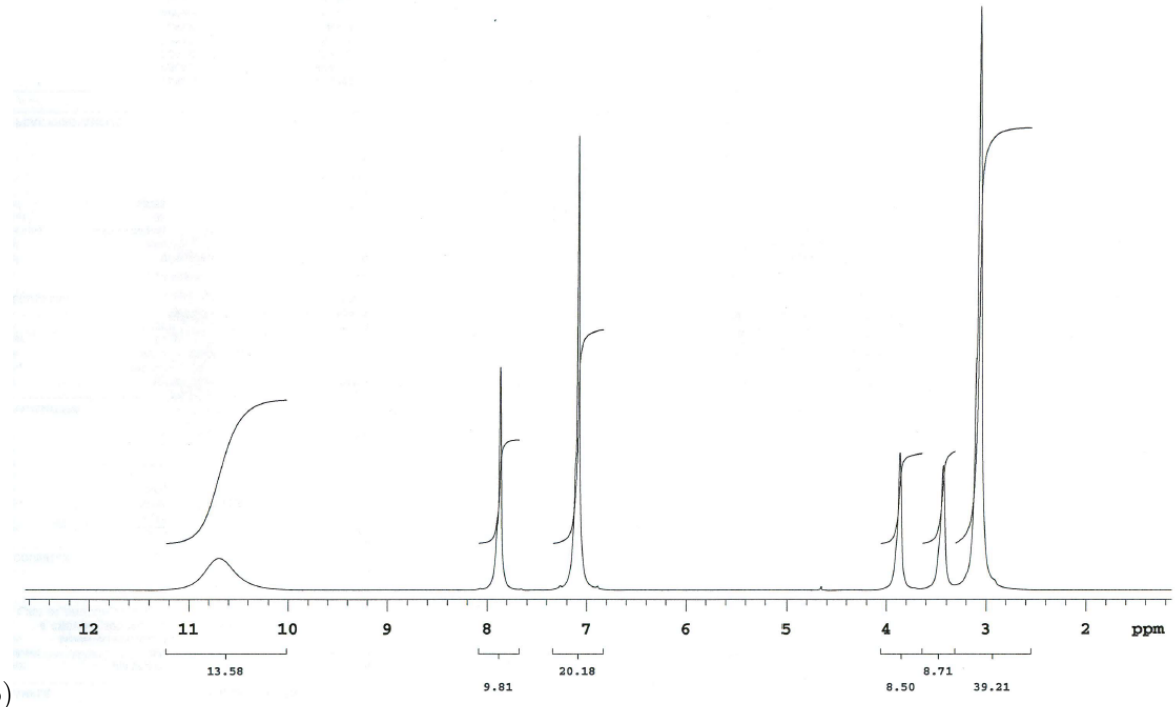

b)

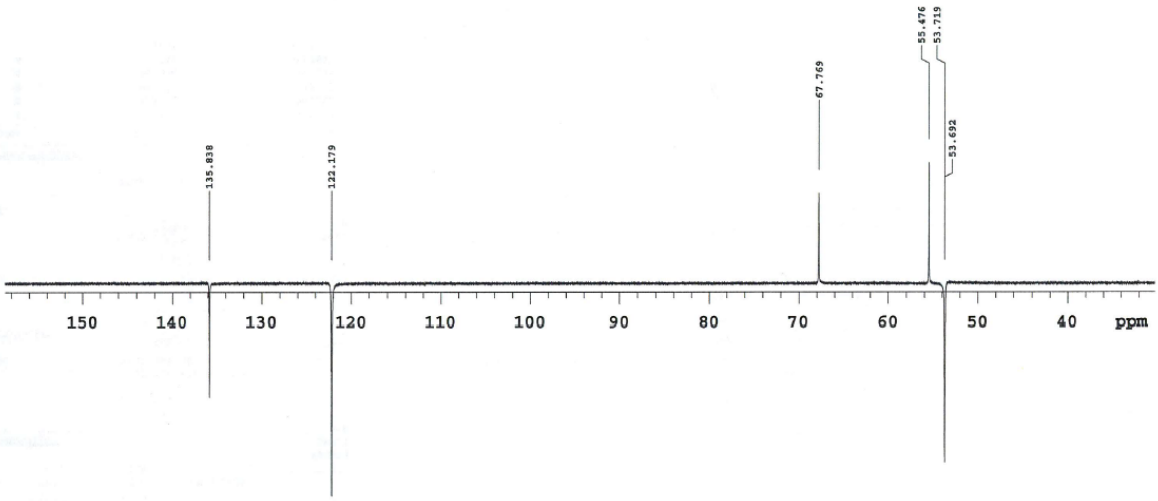

Figure A10: **(a)** ^{1}H NMR spectrum and **(b)** ^{13}C APT NMR spectrum for the sample with 4.53 % water content.

Table .3: Peak assignment of the sample with 4.53 % water content.

	peak position	intensity	assignment
^{1}H spectrum	10.70 ppm	6.85	$(CH_3)_3N^+$–CH_2–CH_2–O**H**; –N**H**–CH=N–CH=CH–
	7.87 ppm	48.36	–NH–C**H**=N–CH=CH–
	7.08 ppm	98.49	–NH–CH=N–C**H**=C**H**–
	3.86 ppm	29.75	$(CH_3)_3N^+$–CH_2–C$\mathbf{H_2}$–OH
	3.43 ppm	50.49	$(CH_3)_3N^+$–C$\mathbf{H_2}$–CH_2–OH
	3.06 ppm	126.80	(C$\mathbf{H_3}$)$_3$N$^+$–CH_2–CH_2–OH
^{13}C spectrum	135.85 ppm	−24.75	–NH–**C**H=N–CH=CH–
	122.19 ppm	−46.23	–NH–CH=N–**C**H=**C**H–
	67.78 ppm	19.51	$(CH_3)_3N^+$–**C**H_2–CH_2–OH
	55.48 ppm	26.13	$(CH_3)_3N^+$–CH_2–**C**H_2–OH
	53.70 ppm	−38.86	(**C**H_3)$_3$N$^+$–CH_2–CH_2–OH

Table .4: Peak assignment of the sample with 9.06 % water content.

	peak position	intensity	assignment
^{1}H spectrum	10.03 ppm	3.66	$(CH_3)_3N^+$–CH_2–CH_2–O**H**; –N**H**–CH=N–CH=CH–
	7.87 ppm	37.73	–NH–C**H**=N–CH=CH–
	7.09 ppm	70.66	–NH–CH=N–C**H**=C**H**–
	3.87 ppm	20.53	$(CH_3)_3N^+$–CH_2–C$\mathbf{H_2}$–OH
	3.43 ppm	19.81	$(CH_3)_3N^+$–C$\mathbf{H_2}$–CH_2–OH
	3.07 ppm	106.58	(C$\mathbf{H_3}$)$_3$N$^+$–CH_2–CH_2–OH
^{13}C spectrum	135.87 ppm	−24.24	–NH–**C**H=N–CH=CH–
	122.20 ppm	−45.90	–NH–CH=N–**C**H=**C**H–
	67.78 ppm	19.30	$(CH_3)_3N^+$–**C**H_2–CH_2–OH
	55.51 ppm	24.50	$(CH_3)_3N^+$–CH_2–**C**H_2–OH
	53.73 ppm	−35.74	(**C**H_3)$_3$N$^+$–CH_2–CH_2–OH

a)

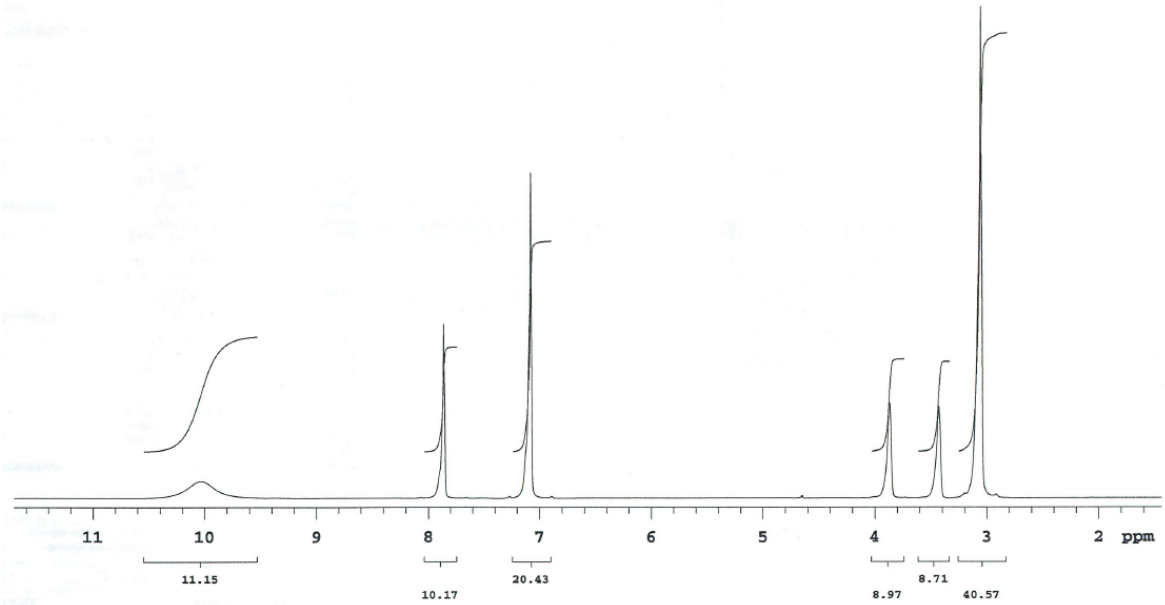

b)

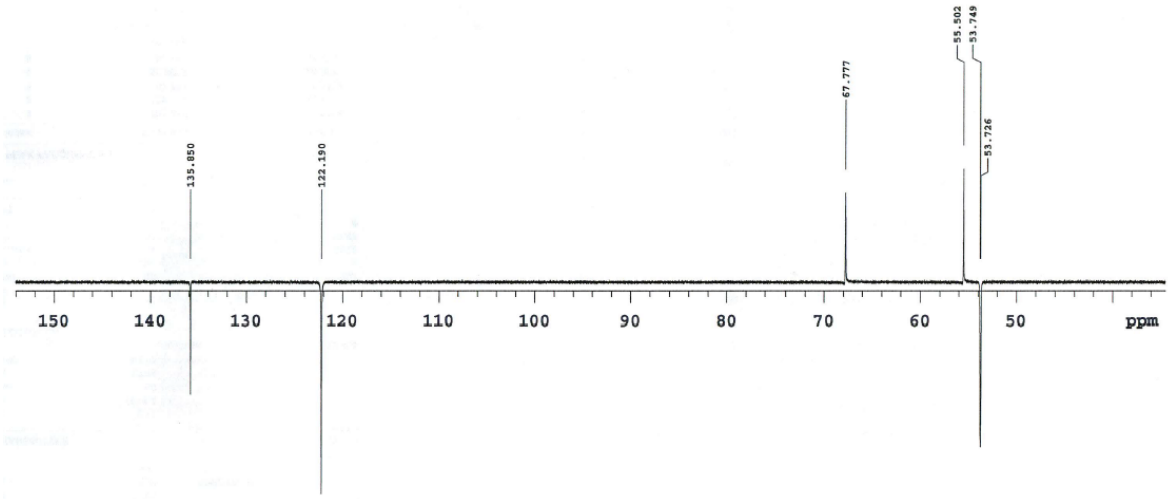

Figure A11: **(a)** ^{1}H NMR spectrum and **(b)** ^{13}C APT NMR spectrum for the sample with 9.06 % water content.

a)

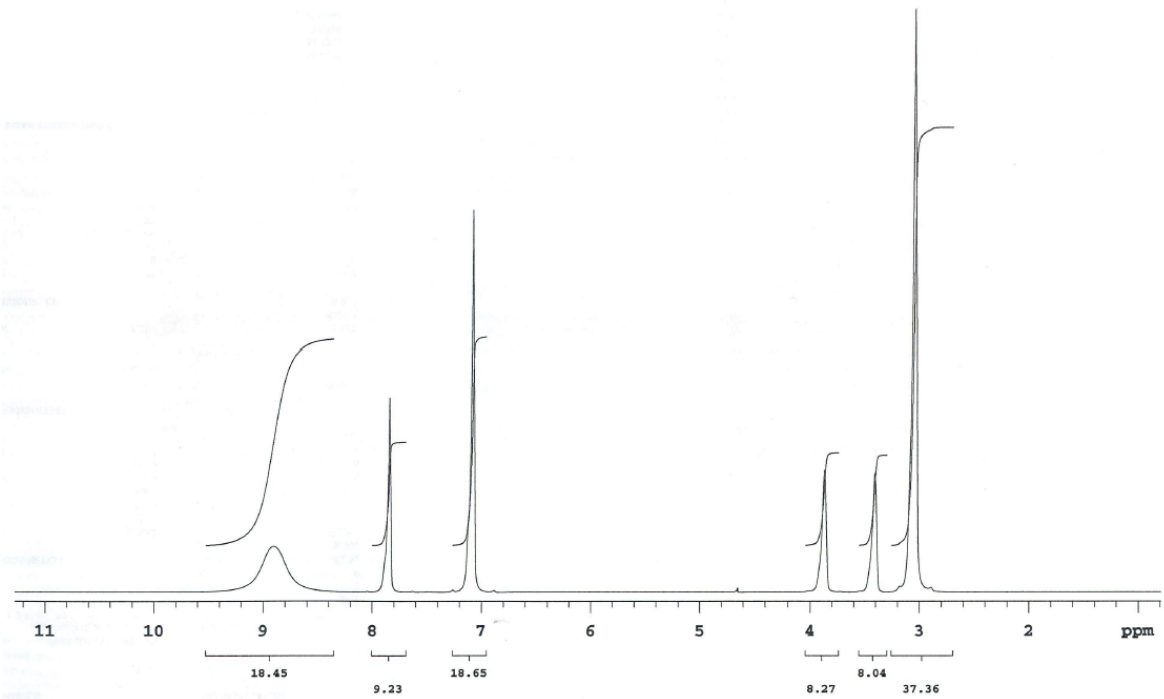

b)

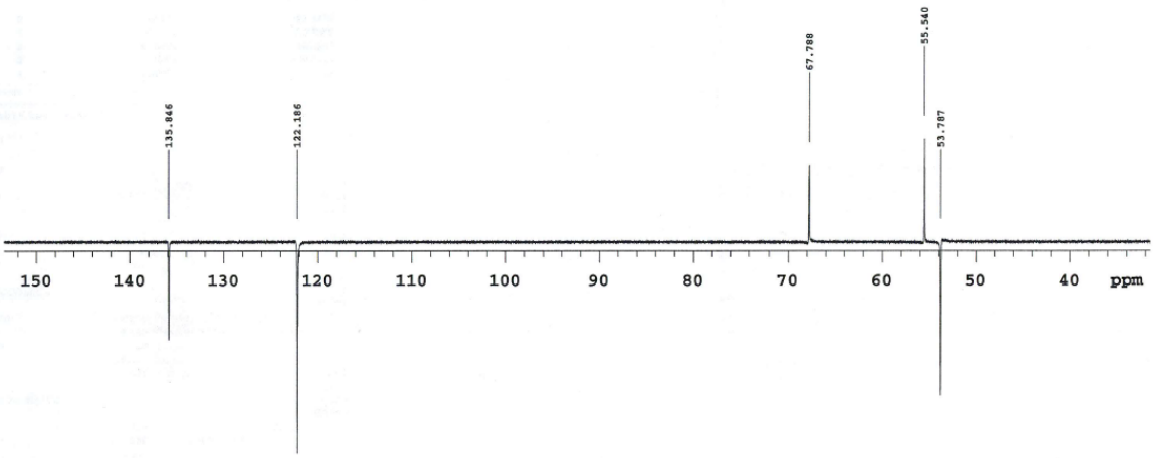

Figure A12: **(a)** ^{1}H NMR spectrum and **(b)** ^{13}C APT NMR spectrum for the sample with 13.06 % water content.

Table .5: Peak assignment of the sample with 13.06 % water content.

	peak position	intensity	assignment
^{1}H spectrum	8.90 ppm	9.84	$(CH_3)_3N^+$–CH_2–CH_2–O**H**; –N**H**–CH=N–CH=CH–
	7.84 ppm	42.09	–NH–C**H**=N–CH=CH–
	7.08 ppm	82.97	–NH–CH=N–C**H**=C**H**–
	3.87 ppm	26.43	$(CH_3)_3N^+$–CH_2–C$\mathbf{H_2}$–OH
	3.41 ppm	25.71	$(CH_3)_3N^+$–C$\mathbf{H_2}$–CH_2–OH
	3.04 ppm	126.75	$(C\mathbf{H_3})_3N^+$–CH_2–CH_2–OH
^{13}C spectrum	135.86 ppm	−21.29	–NH–**C**H=N–CH=CH–
	122.20 ppm	−46.01	–NH–CH=N–**C**H=**C**H–
	67.80 ppm	16.68	$(CH_3)_3N^+$–**C**H_2–CH_2–OH
	55.55 ppm	22.39	$(CH_3)_3N^+$–CH_2–**C**H_2–OH
	53.79 ppm	−33.41	$(\mathbf{C}H_3)_3N^+$–CH_2–CH_2–OH

Table .6: Peak assignment of the sample with 19.97 % water content.

	peak position	intensity	assignment
^{1}H spectrum	4.70 ppm	8.79	$(CH_3)_3N^+$–CH_2–CH_2–O**H**; –N**H**–CH=N–CH=CH–
	4.55 ppm	36.03	–NH–C**H**=N–CH=CH–
	3.80 ppm	70.11	–NH–CH=N–C**H**=C**H**–
	0.60 ppm	17.99	$(CH_3)_3N^+$–CH_2–C$\mathbf{H_2}$–OH
	0.11 ppm	19.09	$(CH_3)_3N^+$–C$\mathbf{H_2}$–CH_2–OH
	−0.28 ppm	106.32	$(C\mathbf{H_3})_3N^+$–CH_2–CH_2–OH
^{13}C spectrum	135.86 ppm	−21.29	–NH–**C**H=N–CH=CH–
	122.20 ppm	−46.01	–NH–CH=N–**C**H=**C**H–
	67.80 ppm	16.68	$(CH_3)_3N^+$–**C**H_2–CH_2–OH
	55.55 ppm	22.39	$(CH_3)_3N^+$–CH_2–**C**H_2–OH
	53.79 ppm	−33.41	$(\mathbf{C}H_3)_3N^+$–CH_2–CH_2–OH

a)

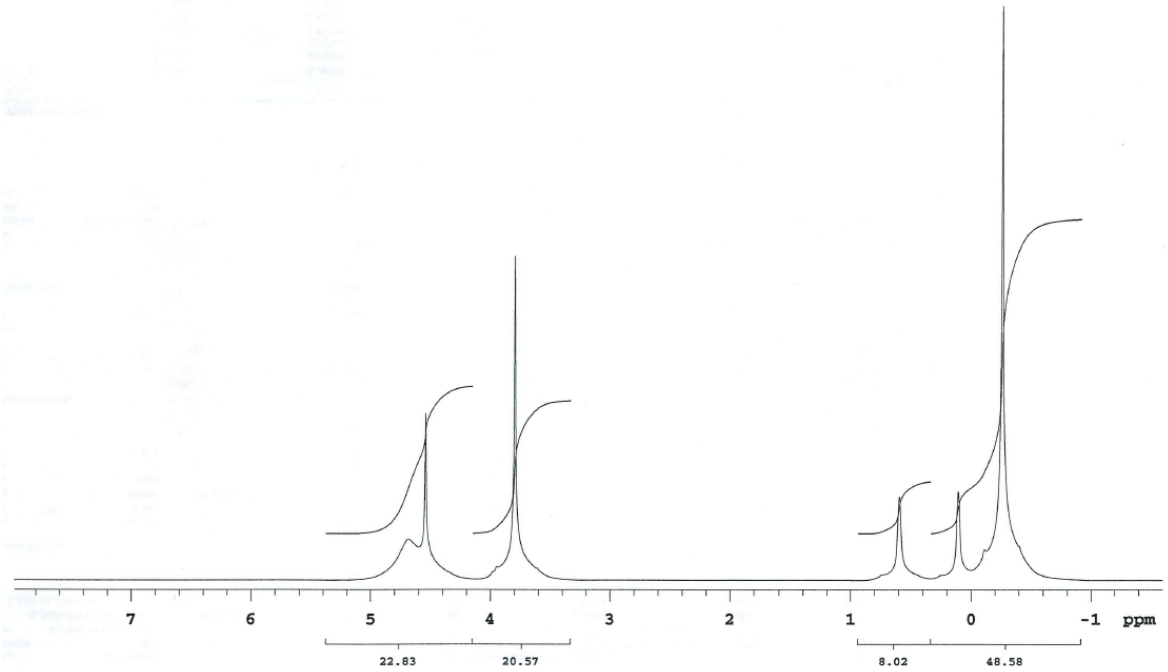

b)

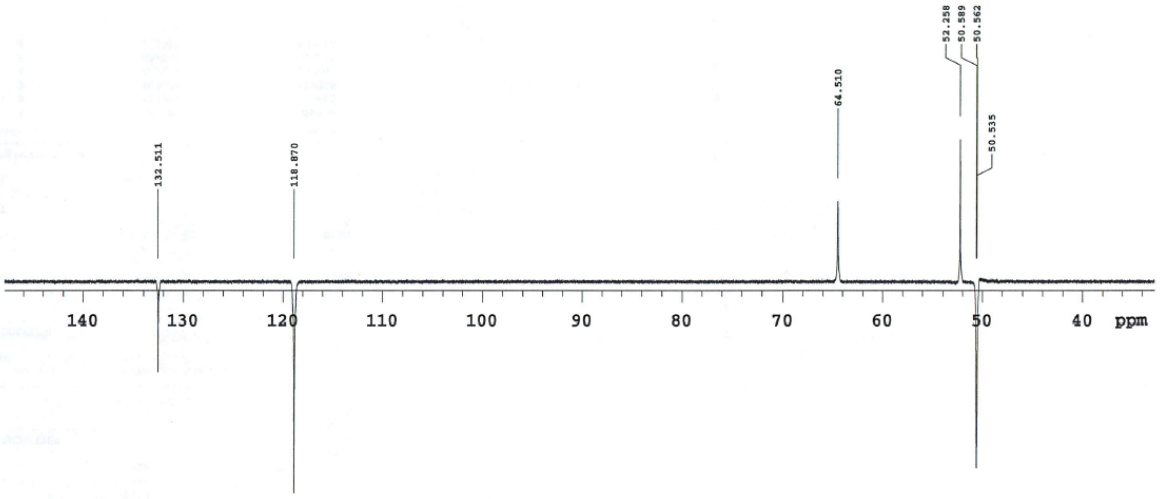

Figure A13: **(a)** ^{1}H NMR spectrum and **(b)** ^{13}C APT NMR spectrum for the sample with 19.97 % water content.

a)

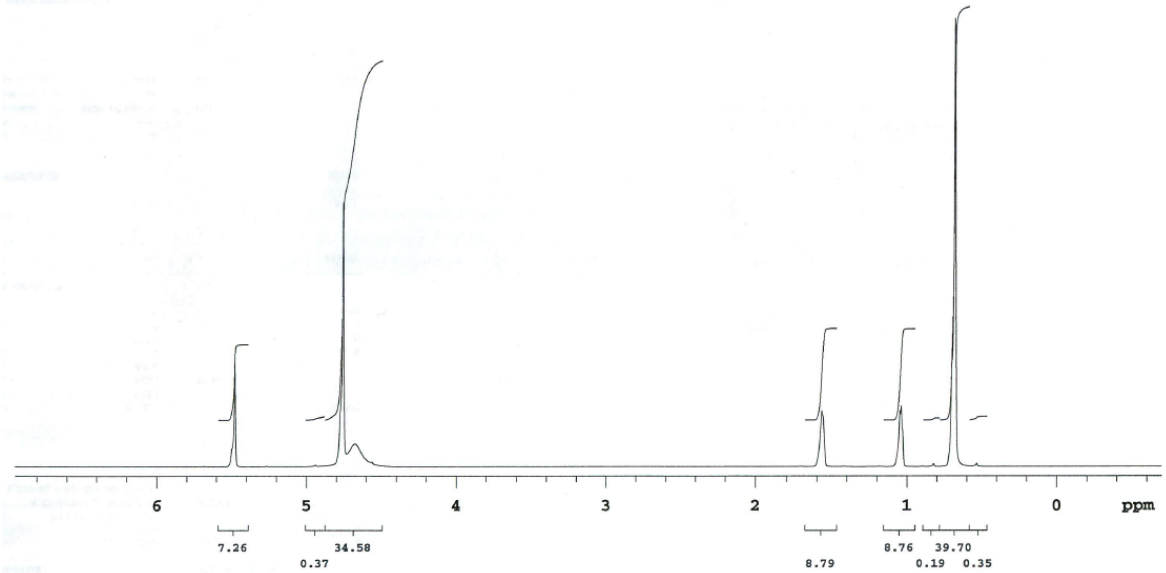

b)

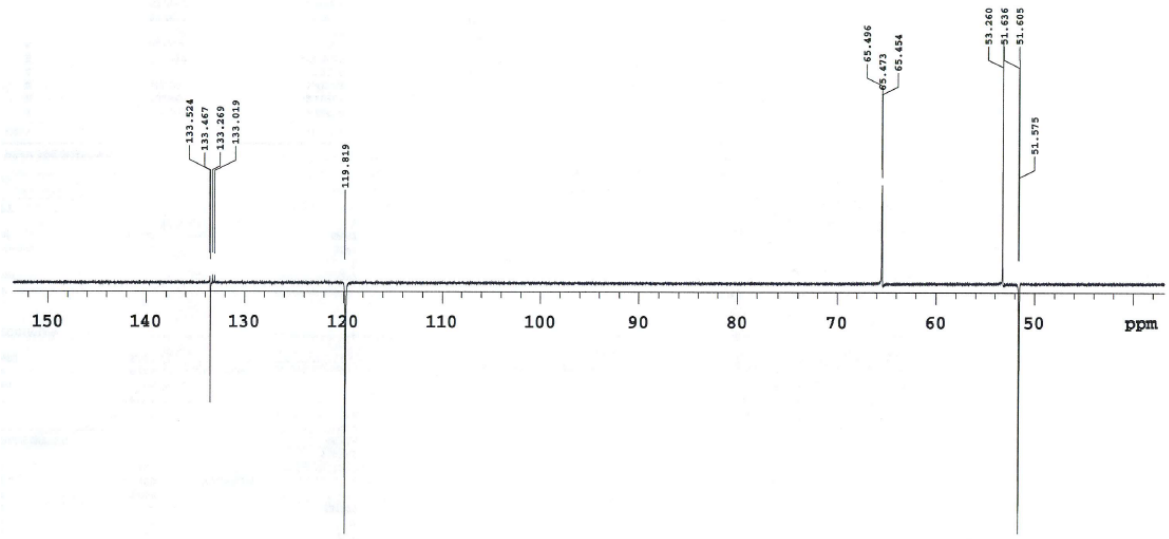

Figure A14: **(a)** ^{1}H NMR spectrum and **(b)** ^{13}C APT NMR spectrum for the sample with 33.59 % water content.

Table .7: Peak assignment of the sample with 33.59 % water content.

	peak position	intensity	assignment
^{1}H spectrum	5.48 ppm	22.84	–NH–C**H**=N–CH=CH–
	4.75 ppm	57.27	–NH–CH=N–C**H**=C**H**–
	4.67 ppm	4.94	$(CH_3)_3N^+$–CH_2–CH_2–O**H**; –N**H**–CH=N–CH=CH–
	1.57 ppm	12.07	$(CH_3)_3N^+$–CH_2–C$\mathbf{H_2}$–OH
	1.04 ppm	13.10	$(CH_3)_3N^+$–C$\mathbf{H_2}$–CH_2–OH
	0.68 ppm	96.93	(C$\mathbf{H_3}$)$_3$N$^+$–CH_2–CH_2–OH
^{13}C spectrum	133.48 ppm	−25.99	–NH–**C**H=N–CH=CH–
	119.83 ppm	−54.40	–NH–CH=N–**C**H=**C**H–
	65.48 ppm	21.38	$(CH_3)_3N^+$–**C**H_2–CH_2–OH
	53.27 ppm	53.10	$(CH_3)_3N^+$–CH_2–**C**H_2–OH
	51.61 ppm	−54.12	(**C**H_3)$_3$N$^+$–CH_2–CH_2–OH

Table .8: Peak assignment of the sample with 43.08 % water content.

	peak position	intensity	assignment
^{1}H spectrum	6.83 ppm	15.72	–NH–C**H**=N–CH=CH–
	6.15 ppm	71.47	–NH–CH=N–C**H**=C**H**–
	4.66 ppm	14.98	$(CH_3)_3N^+$–CH_2–CH_2–O**H**; –N**H**–CH=N–CH=CH–
	2.99 ppm	13.12	$(CH_3)_3N^+$–CH_2–C$\mathbf{H_2}$–OH
	2.41 ppm	15.38	$(CH_3)_3N^+$–C$\mathbf{H_2}$–CH_2–OH
	2.08 ppm	126.90	(C$\mathbf{H_3}$)$_3$N$^+$–CH_2–CH_2–OH
^{13}C spectrum	134.95 ppm	−12.00	–NH–**C**H=N–CH=CH–
	121.15 ppm	−31.35	–NH–CH=N–**C**H=**C**H–
	66.82 ppm	13.42	$(CH_3)_3N^+$–**C**H_2–CH_2–OH
	54.74 ppm	45.90	$(CH_3)_3N^+$–CH_2–**C**H_2–OH
	53.11 ppm	−33.59	(**C**H_3)$_3$N$^+$–CH_2–CH_2–OH

a)

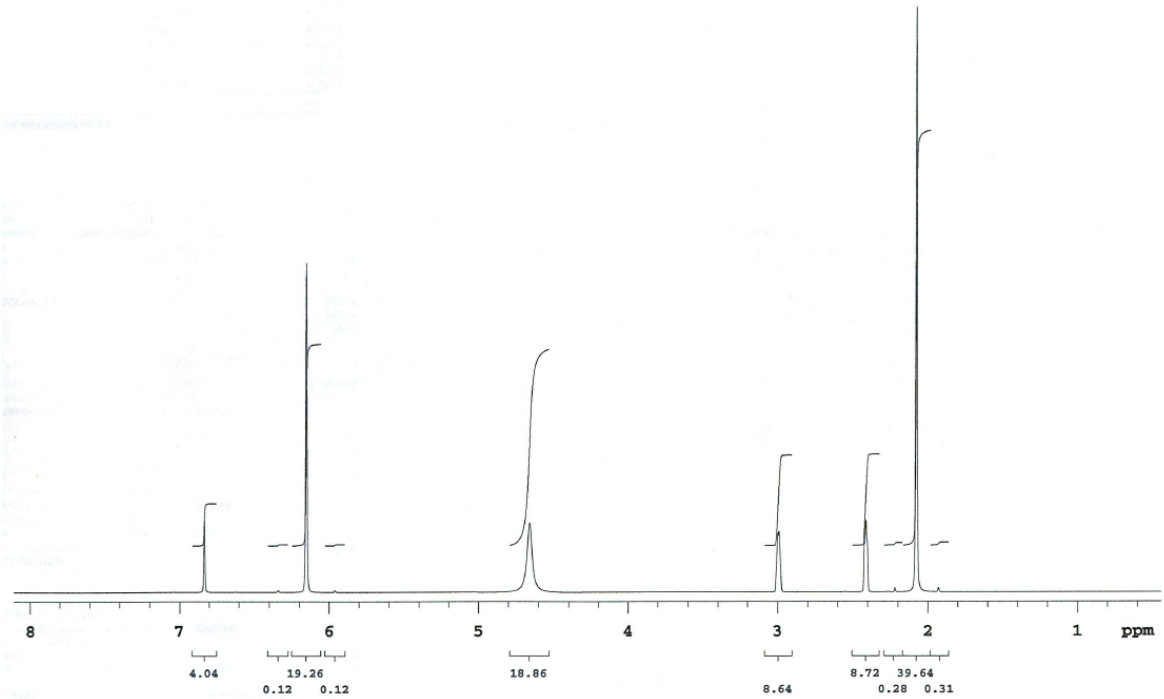

b)

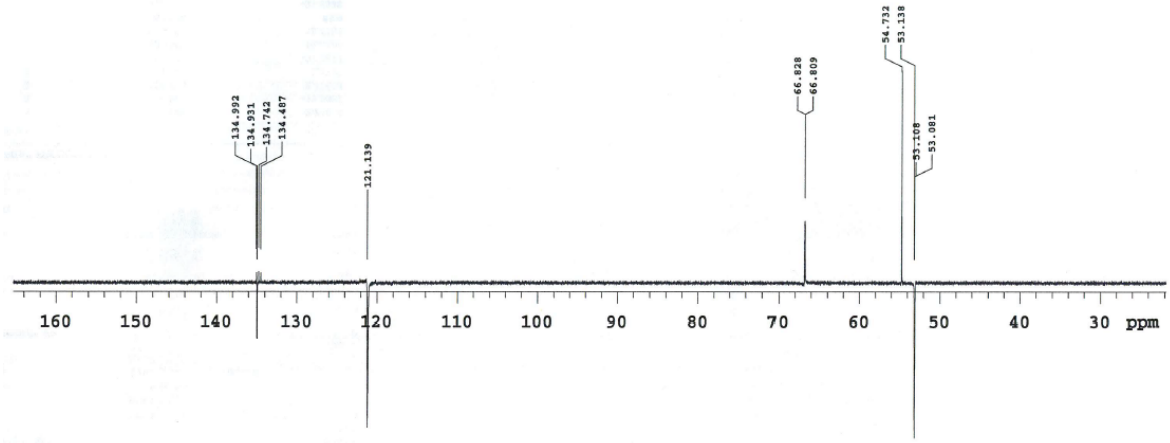

Figure A15: **(a)** ^{1}H NMR spectrum and **(b)** ^{13}C APT NMR spectrum for the sample with 43.08 % water content.

Chapter 3

A3.1 5 μM MBP in 100 % (EMIm)(BF_4)

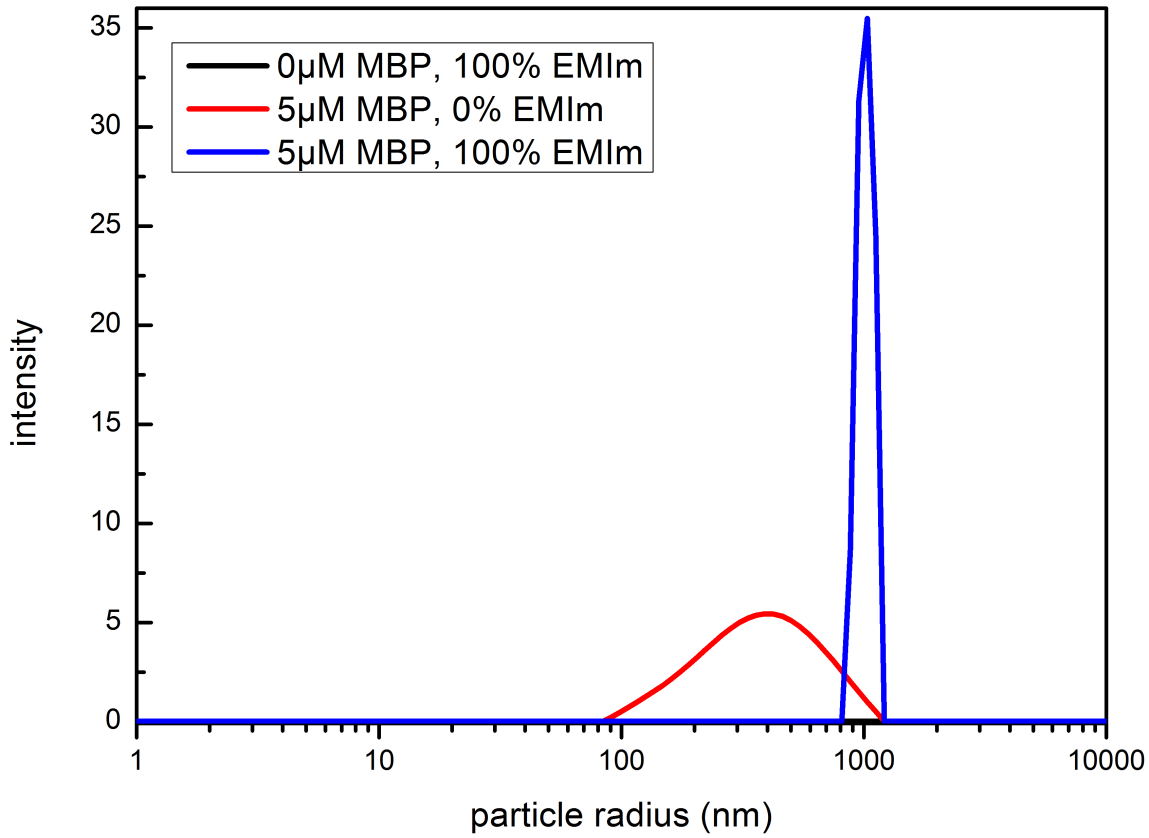

Figure A16: Particle size distributions of 5 μM MBP in pure [EMIm][BF_4]. For each image, the reference plots of the pure ionic liquid without MBP as well as the MBP in pure buffer solution are shown.

A3.2 10 μM MBP in 100 % (EMIm)(BF_4)

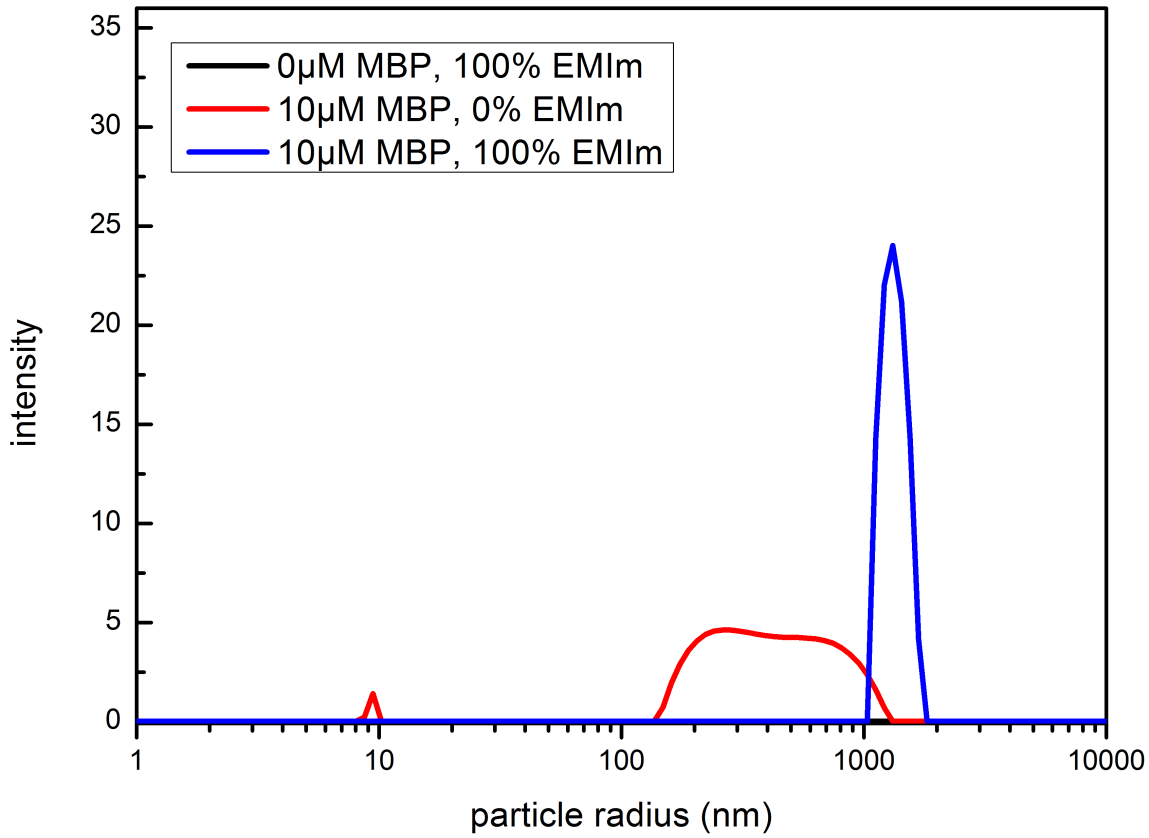

Figure A17: Particle size distributions of 10 μM MBP in pure [EMIm][BF_4]. For each image, the reference plots of the pure ionic liquid without MBP as well as the MBP in pure buffer solution are shown.

A3.3 5 μM MBP in 100 % (BMIm)(BF_4)

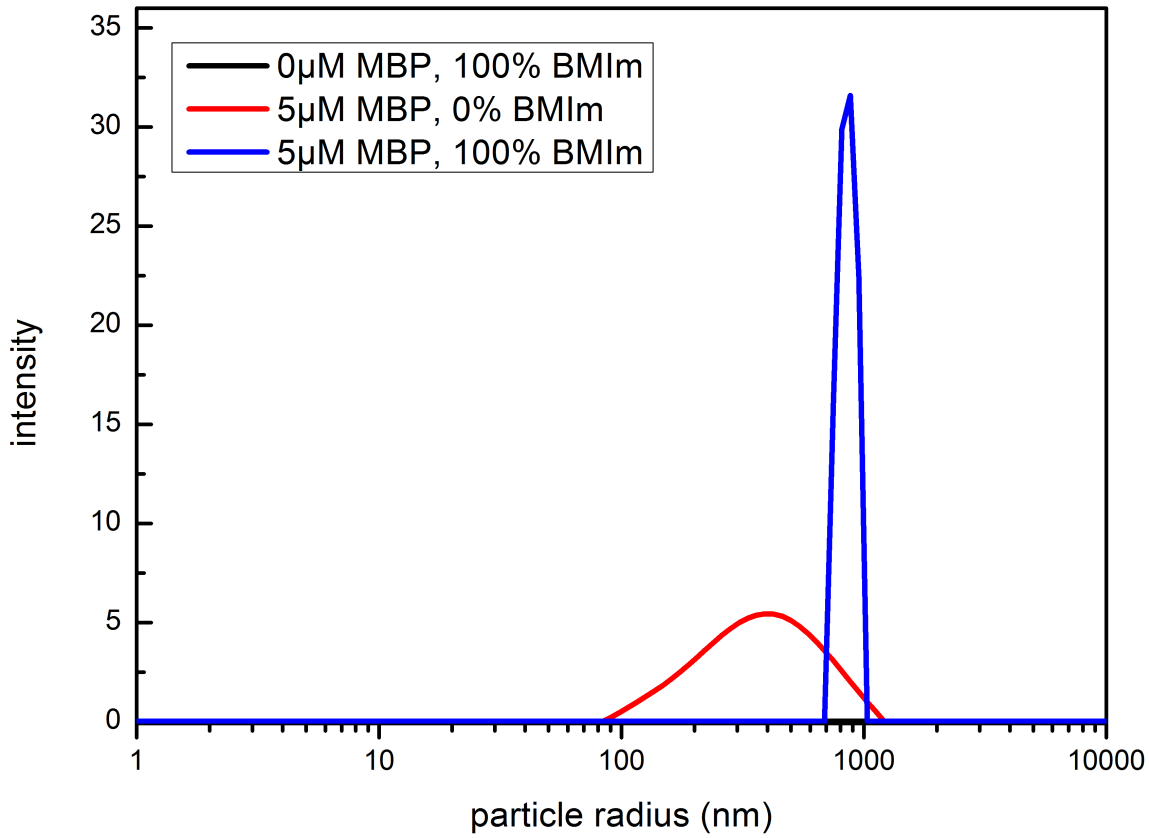

Figure A18: Particle size distributions of 5 μM MBP in pure [BMIm][BF_4]. For each image, the reference plots of the pure ionic liquid without MBP as well as the MBP in pure buffer solution are shown.

A3.4 10 μM MBP in 100 % (BMIm)(BF_4)

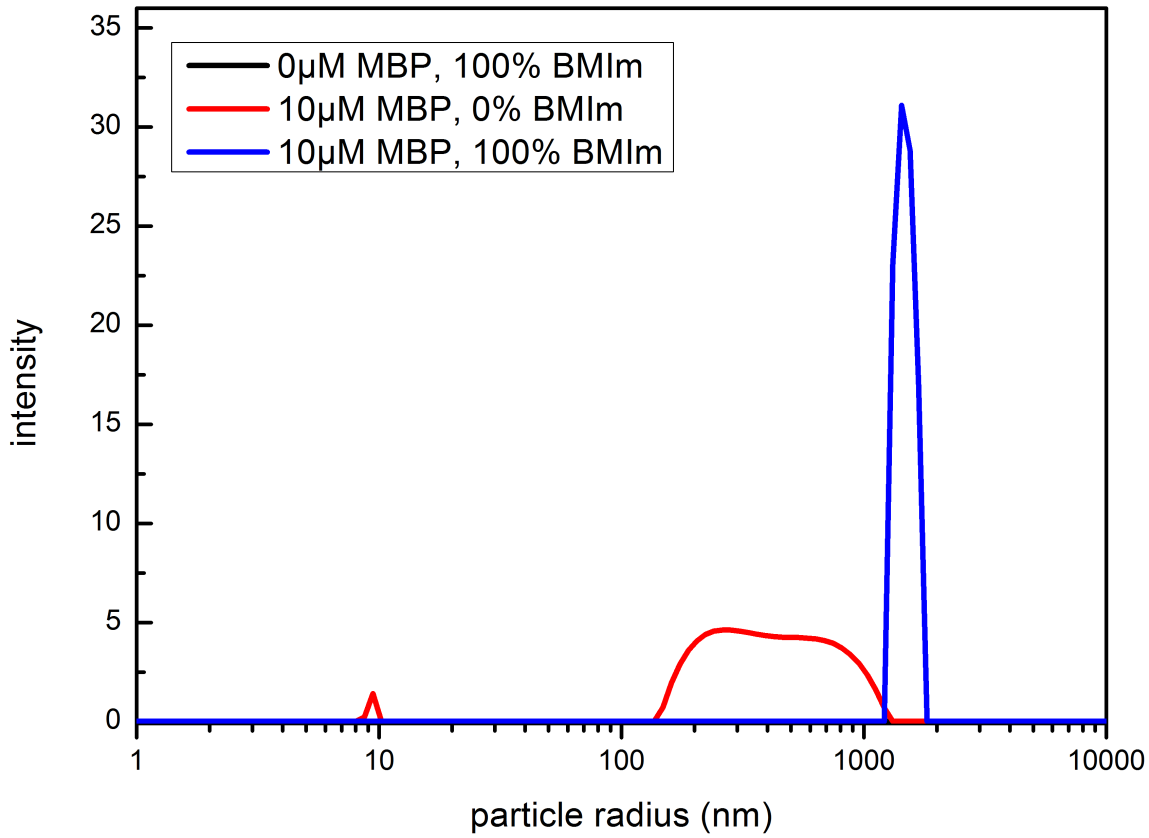

Figure A19: Particle size distributions of 10 μM MBP in pure [BMIm][BF_4]. For each image, the reference plots of the pure ionic liquid without MBP as well as the MBP in pure buffer solution are shown.

Scientific contributions

List of publications

- U. Cerajewski, J. Träger, S. Henkel, A. H. Roos, M. Brehm, and D. Hinderberger. Nanoscopic structures and molecular interactions leading to a dystectic and two eutectic points in [EMIm][Cl]/urea mixtures. *Phys. Chem. Chem. Phys.*, 20:29591–29600, 2018. doi: 10.1039/C8CP04912B.

Oral contributions

- U. Cerajewski, and D. Hinderberger. Using EPR spectroscopy as a method for probing the molecular structure and dynamics of ionic liquids. *3rd International Conference on Ionic Liquid-Based Materials (ILMAT).*, Berlin (Germany), 8. Dec. 2015–11. Dec. 2015.

Poster contributions

- U. Cerajewski, and D. Hinderberger. CW EPR spectroscopy – a simple method for assessing structure and dynamics of complex soft matter on the nanoscale. *Asia-Pacific EPR/ESR Society and The International EPR Society Symposium (APES IES).*, Brisbane (Australia), 23. Sep. 2018–27. Sep. 2018.

- U. Cerajewski, and D. Hinderberger. CW EPR temperature series – a simple method for assessing structure and dynamics of deep-eutectic solvents on the nanoscale. *40th FGMR Annual Discussion Meeting.*, Leipzig (Germany), 10. Sep. 2018–13. Sep. 2018.

Acknowledgements

Großen Dank möchte ich Prof. Dr. Dariush Hinderberger aussprechen für die Ermöglichung der Arbeit an meinem Wunschthema und für das zahlreiche Feedback und die vielen Stunden der Ideensammlung und des Gedankenaustauschs. Ich schätze das familiäre Verhältnis in der Abeitsgruppe sehr und wurde immer entsprechend meiner persönlichen Talente gefördert und gefordert.

Vielen Dank außerdem an die Unterstützung der wissenschaftlichen Mitarbeiter und Angestellten, insbesondere an Dr. Andreas Kerth und Heike Schimm, die stets für jedes Problem eine Antwort hatten. Weiterhin gilt mein Dank allen Zuarbeiten für die Dissertation von meinen betreuten Schülern/Studenten: Jennica Träger, Selgar Henkel, Gerhard Reglich, Andreas Roos, und Josefin Abert sowie den Hilfestellungen und der Zeit für mich von Dr. Krushelnitsky, Dr. Hempel und Dr. Ströhl für indivuelle NMR Messreihen und deren Auswertungen und Dr. Ott für SAXS-Messungen.

Ich danke meinen Freunden und meiner Familie für den steten Rückhalt und die Motivationsschübe. Was die Promotionszeit besonders schön gemacht hat, waren alle Gruppenmitglieder der AG Hinderberger, die vielen Gespräche, die gemeinsamen Kuchenrunden und Freizeitaktivitäten. Ich danke euch allen für diese schöne Zeit!

Ulrike Cerajewski

Curriculum vitae

Persönliche Angaben

Geschlecht	**weiblich**.
Geburtsdatum	**10. Mai 1990**.
Geburtsort	**Potsdam**.
Nationalität	**Deutsch**.
Akademischer Grad	**M. Sc**.

Akademische Ausbildung

10/2008–03/2012	**Bachelorstudium der Chemie**, *Universität Leipzig*, Augustusplatz 10, 04109 Leipzig.
03/2012	**erreichter Abschluss**, *Bachelor of Science*.
04/2012–03/2015	**Masterstudium der Chemie**, *Universität Leipzig*, Augustusplatz 10, 04109 Leipzig.
03/2015	**erreichter Abschluss**, *Master of Science*.
06/2015–09/2020	**Promotionsstudium der Chemie**, *Martin-Luther-Universität Halle-Wittenberg*, Von-Danckelmann-Platz 4, 06120 Halle.
12/2020	**voraussichtl. Abschluss**, *Dr. rer. nat.*

Declaration of original authorship

Hiermit bestätige ich, dass ich die vorliegende Arbeit selbständig verfasst und keine anderen als die angegebenen Hilfsmittel benutzt habe. Die Stellen der Arbeit, die dem Wortlaut oder dem Sinn nach anderen Werken (dazu zählen auch Internetquellen) entnommen sind, wurden unter Angabe der Quelle kenntlich gemacht.

Es wurden keine bereits vergeblichen Promotionsversuche unternommen und die Dissertation ist zu keinem Zeitpunkt in ihrer jetzigen oder in einer anderen Fassung einer anderen Fakultät vorgelegt worden.

Es liegen keine Vorstrafen oder Ermittlungsverfahren vor.